MODELING OF THIN FILM EVAPORATION HEAT TRANSFER AND EXPERIMENTAL INVESTIGATION OF MINIATURE HEAT PIPES

A Dissertation
Presented to
the Faculty of the Graduate School
University of Missouri-Columbia

In Partial Fulfillment
Of the Requirements for the Degree

Doctor of Philosophy

By

ANJUN JIAO

Dr. Hongbin Ma, Dissertation Supervisor
Dr. John K. Critser, Dissertation Co-supervisor

MAY 2008

The undersigned, appointed by Dean of the Graduate School, have examined the dissertation entitled

MODELING OF THIN FILM EVAPORATION HEAT TRANSFER AND EXPERIMENTAL INVESTIGATION OF MINIATURE HEAT PIPES

Presented by Anjun Jiao

A candidate for the degree of Doctor of Philosophy

And hereby certify that in their opinion it is worthy of acceptance.

_____

_____

_____

_____

_____

ACKNOWLEDGEMENTS

I would like to express my deepest gratitude to my major advisor, Dr. Hongbin Ma and Dr. John K. Critser, for their supervision, encouragement and mentoring. They have always been supporting, patient and inspiring. I have been very lucky to have them as my major advisor, and I deeply appreciate their Research Assistantship support during my stay at University of Missouri-Columbia.

I am grateful to Prof. Yuwen Zhang, Prof. Gary L. Solbrekken, and Prof. Qingsong Yu (Department of Chemical Engineering) for serving as my committee members and for their discussions and suggestions in my research. My colleagues of Dr. Ma's group, Corey Wilson (Ph.D Candidate), Brian Borgmeyer (Ph.D Candidate), and Peng Cheng (Ph.D Candidate) deserve my sincere appreciation for their help and encouragement.

I would also like to thank Pat Free and Melanie Gerlach for all your help with staying on top of all the graduate paperwork.

Finally, my wife Qiqi Guo always encourages and comforts me. My sisters and brothers have given me warm support, and I am very grateful to them.

TABLE OF CONTENTS

LIST OF FIGURES

LIST OF SYMBLES

A	Hamaker constant 10^{-19} J; cross section area, m^2 ,
a	constant defined by Eq. (2-4)
b	constant defined by Eq. (2-4)
C	constant
D	diameter, m
d	half width of wick's top wall in Fig. 2-2
f	friction factor
g	gravity acceleration, m/s^2
h	heat transfer coefficient, J/Km^2; height, m
h_{fg}	latent heat of vaporization, kJ/kg
h_t	defined by figure1
K	defined by equation (2-23)
k	conductivity, W/m.K, curvature, 1/m
L	length, m

N	number of grooves
P	wetting perimeter, m
p	pressure, N/m^2
p_d	disjoining pressure, N/m^2
Q	heat load, W
$q^{'}$	heat flux, W/m^2
R	gas constant, J/kg K
Re	Reynolds number
$R_{30,60}$	radius at α =30 or 60, m
r	radius, m
$\bar{r}$	average meniscus radius, m
S	coordinate, m
T	temperature, K
u	velocity, m/s
W	width of heat pipe, m
w	with of groove, m
x	coordinate, m
y	coordinate, m
z	coordinate, m

Greek

α	contact angle, rad

β	angle defined by Fig.2-2, rad
δ	film thickness, m
δ_0	nonevaporating film thickness, m
ε	defined by eq. (3-41)
ϕ	slant angle of heat pipe, rad
γ	angle defined by Fig.3-2(a), rad
η	coordinate, m
θ	angle defined by Fig.2-1, deg
λ	angle defined by Fig.3-2, rad
μ	viscosity, N.s/m^2
θ	coordinates, deg
ρ	density, kg/m^3
σ	surface tension, N/m
Δ	difference

Subscripts

a	adiabatic, region (a) in Fig. 3-2
B	bottom
b	region (b) in Figs.1, 2
B-B	B-B thin film region in Fig. ,2-2 and 3-2
c	condenser, capillary
C-C	C-C thin film region in Fig. 2-2

D-D	D-D thin film region in Fig.2-2
e	evaporator
eff	effective
g	gravity
h	hydraulically
i	defined by Eq. (3-24)
l	liquid
loc	location
l,l	liquid-line
lv	vapor-line; interface of liquid-vapor
macro	macro region
max	maximum
men	meniscus
micro	micro region
min	minimum
p	particle
sat	saturated
T	top
th	thickness
tot	total
v	vapor
w	wire, wall
(z)	z coordinate

δa	thickness of region (a)
δb	thickness of region (b)
δv	liquid-vapor interface

ABSTRACT

The heat pipe, as one of the most efficient heat transport devices, is a peerless choice in the electronic cooling field. In order to better understand the heat transfer mechanisms of the heat pipe, a heat transfer model, which considers the effects of the surface condition, disjoining pressure, gravity force, and contact angle on the thin film profile, heat flux distribution, has been developed. The theoretical analyses showed that the heat transfer in the evaporator could be divided into three templates: CASE I, II, and III with increasing the heat load input. In order to verify the theoretical analysis, experimental investigations of a grooved heat pipe with micro trapezoid wicks, a miniature loop heat pipe with a copper sintered-layer flat evaporator, and a flat heat pipe with the wire core wicks were conducted, respectively. Comparison of the experimental data with theoretical results showed that the model can be used to predict the temperature response in evaporator at low heat load but is invalid at high heat load. The thin film evaporation heat transfer model is successful to address the heat transfer in a cell during the freezing process. In order to obtain ultra-high cooling rate and uniform temperature profiles at cryogenic temperature, one cryogenic oscillating heat pipe with the liquid nitrogen as its working fluid has been developed and experimentally studied. Experimental results showed that its heat transport capability reached 380W with $\Delta T_{Ave,e-c} = 49^0\mathrm{C}$ at charged ratio of 48 percent. At steady state, the amplitude of temperature response in evaporator was smaller than that of condenser while the temperature response kept the same frequency in both evaporator and condenser. The ΔT amplitude between evaporator and condenser decreased with increasing the heat load.

CHAPTER 1. INTRODUCTION

1.1 Overview

With the technology development of very large scale integrated (VLSI) circuits, high performance and more compact design of microelectronic elements and equipment accompany high power consumption resulting in higher heat fluxes in these components or systems [1-4]. Compact design of microelectronic equipment makes the heat transmission more difficult due to the increasing integration and power density of chips. Effective thermal management in those systems has been, and will continue to be one of the most critical issues to be resolved in order to maintain and keep their peak performance [5-6]. However, conventional cooling methods such as the conventional heat sinks without phase-change heat transfer are of impractical function at such high heat fluxes due to the constraints in the low thermal conductivity, volume and weight associated with metal fin-array heat sinks. While an impingement cooling jet, in which the CHF using a water spray was approximately 790W/cm^2 with a water flowrate of 516ml/min by single phase liquid convection in microchannels [7], can be operated at ultra-high heat flux condition, however, it needs an additional pump with a power supply. Although a variety of cooling techniques have been applied to thermal management of electronic units, urgent demand for cooling high power density with low cost and compact design gives impetus to searching for more efficient heat transport devices. The heat pipe, as the most efficient system known today among the many different types of heat transport systems [12], makes it become into the peerless choice in the electronics cooling field. Heat pipes have been designed and fabricated with various cross-

sectional shapes as small as 0.6mm×0.6mm and 25mm in length (micro heat pipes), and as large as 100m in length [12]. Heat pipes can be classified in several ways [13]: by operating temperature ranges (cryogenic, ambient, or liquid metal), by wicking structure (arterial or composite), or by function (rotating/revolving heat pipes, micro-heat pipes, variable conductance heat pipes, or thermal diodes). But all of them normally consist of two or three sections: evaporator, adiabatic section (this section does not exist sometimes) and condenser, as shown in Fig.1-1. When heat load is supplied to the wall of evaporator, the working fluid in the liquid phase in the evaporator vaporizes into vapor, the vapor travels through adiabatic section and arrives at the condenser section where it releases its latent heat of vapor and the heat is removed by heat sinks. At the same time, the vapor is condensed into liquid.

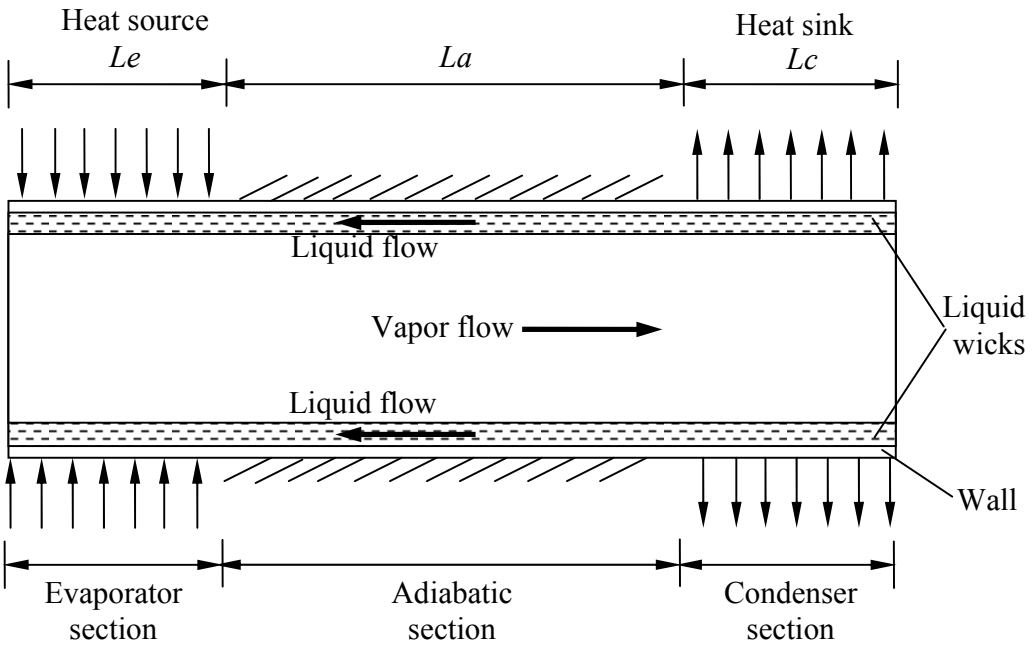

Figure 1-1 Schematic of conventional heat pipe

Capillary pumping pressure pulls the condensate back to the evaporator, and the cycle is complete.

Heat pipes offer a low weight, long-life solution to many types of thermal problems. The advantage of using a heat pipe over other conventional methods is that large quantities of heat can be transported through a small cross-sectional area over a considerable distance with no any additional power input to the system. Furthermore, uniform temperature distribution, design and manufacturing simplicity, small end-to-end temperature drops, and the ability to control and transport high heat flux at various temperature levels are unique features of heat pipes.

1.2 Limits and Maximum Heat Transport Capacity of Heat Pipes

Although heat pipes are very efficient heat transfer devices, they are subject to a number of heat transfer limitations. Its heat transport capacity is often restricted by the capillary, sonic, boiling, entrainment, and viscous limit at steady-state conditions [8-13]. Theoretical analyses and experimental investigations on the capillary limits for different wicks have been conducted [14-19]. The capillary limit was defined that the sum of pressure drop occurring in the flow path shall not surpass the maximum capillary pressure head so that the fluid flow can be pumped back from the condenser to evaporator. The basic relationship can be expressed as:

$$P_c \geq \Delta P_l + \Delta P_v + P_{others} \tag{1.1}$$

where, P_c is capillary pressure and can be predicted by Young-Laplace equation, which depend on the meniscus radii formed in the evaporator and condenser. ΔP_l and ΔP_v are the

pressure drops of liquid flow and vapor flow created between the evaporator and condenser. ΔP_{others} include the gravity and other factors to create the pressure drop. Each of these pressure terms is determined independently and combined to obtain an expression for the maximum heat transport capability.

Previous investigations, such as: Peterson [13], Faghri [12], Dunn and Reay [20], indicated that the sonic, entrainment, boiling, and viscous limits can be respectively expressed as,

$$q_s = A_v \rho_v h_{fg} \left[\frac{\gamma_v R_v T_v}{2(\gamma_v + 1)} \right]^{1/2} \tag{1.2}$$

$$q_e = A_v h_{fg} \left[\frac{\sigma \rho_v}{2(r_{h,w})} \right]^{1/2} \tag{1.3}$$

$$q_b = \left[\frac{2\pi L_{eff} k_{eff} T_v}{h_{fg} \rho_v \ln\left(\frac{r_l}{r_v}\right)} \right] \left(\frac{2\sigma}{r_n} - \Delta P_{c,m} \right) \tag{1.4}$$

$$q_v = \frac{D_{hl}^2 h_{fg} \rho_v P_v}{64} A_v \tag{1.5}$$

respectively. Those limitations based on steady state model have been widely investigated and Fig. 1-2 illustrates the results predicted by Cotter [16] and Babin et al [8] for a trapezoidal micro-heat pipe with water at a horizontal orientation. As shown in Fig. 1-2, the capillary limit is the most important among those limitations for most heat pipes.

As presented above, the capillary limitation is the critical limit for the heat pipes cooling the electronic components/systems, therefore, the heat load added on the heat pipe cannot infinitely increase, and when it is higher than one value, it will result in the sum of the

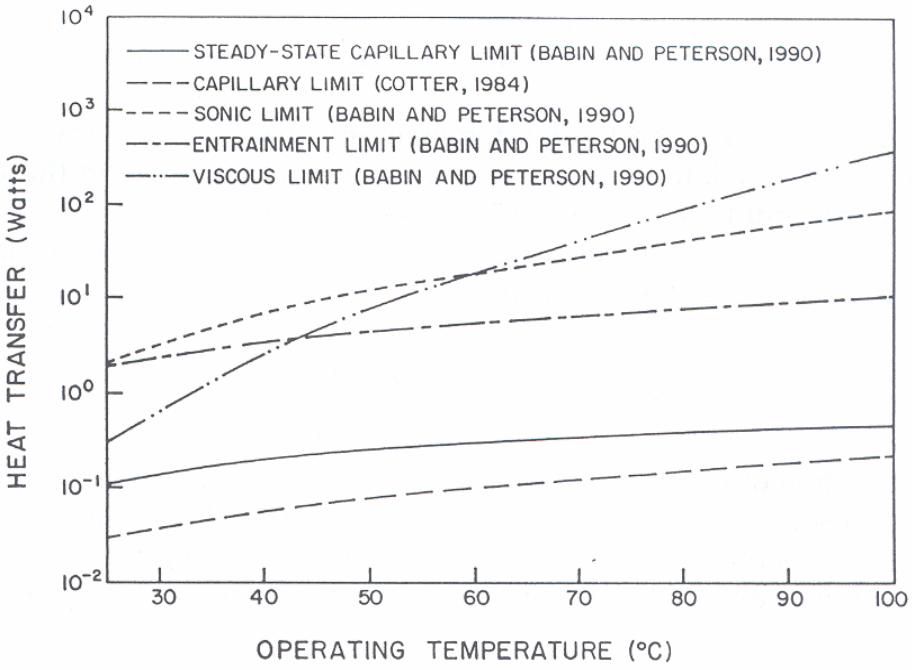

Figure 1-2 maximum heat transport capacity under different limits

pressure drops occurring in the flow path is higher than the capillary pump pressure. Thus, the investigation herein will only focus on the capillary limit of heat pipes.

1.3 Modeling Thin Film Evaporating Heat Transfer in Heat Pipes

Many electronic components or systems often generate very high heat fluxes and heat generated must be dissipated in order to keep uniform temperature distribution and maintain its operating temperature limit and peak performance. When the heat pipe technology is used as a cooling strategy for those modern systems, the further increase of the effective thermal conductivity of the heat pipe is the key for the high-heat flux applications. As a high heat flux is added on the evaporating section of the heat pipe, the thin film evaporation heat transfer

plays an important role in keeping its operation. A better understanding of the heat transport mechanisms in the thin film region will directly help the designs of highly efficient heat pipes and advanced thermal management systems.

A number of previous investigations [14, 15, 17-18] have been conducted on the thin film evaporation heat transfer mechanisms and heat transport occurring in micro grooves, and indicate that most of the heat is transferred through the region where the thickness of the liquid layer is extremely small. One proposed mechanisms is by means of thin film evaporation heat transfer, where the heat transfer is believed to form a thin liquid layer on the heated surface through which heat is conducted. Because the top of the film is assumed to be at the saturation temperature, thinner films result in higher heat transfer as a result of the increased thermal gradient across the film. In this case, accurately predicting the thin film distribution and determining the heat flux in the evaporator are very important. Once the thin film profile and heat flux distribution are obtained, the temperature response in the evaporator as well as the temperature difference between the evaporator and condenser at a given heat load can be calculated. Due to the disjoining pressure effect, the thin film is often divided into three regions, namely, the equilibrium non-evaporating film region, evaporating film region, and meniscus region. In the evaporating film region, the disjoining pressure plays a key role and affects the interface temperature and heat transfer rate through the thin film. Ma and Peterson [9] found that the evaporating heat transfer coefficient through the thin film region depends on the meniscus radius and the superheat. Wayner [22] and Ma et al.[4] show that when the heat flux level added on the thin film region increases, the contact angle increases resulting in a decrease of the evaporating heat transfer coefficient, which presents a

limitation of heat transport capability in a high heat flux heat pipe. Recently, Demsky and Ma [17], Jiao, Ma, and Critser [5] theoretically analyzed the curved surface effects on the thin film profiles and heat flux distributions in the evaporator with wire core or sintered surface. Experimental investigations of groove heat pipe with trapezoids wicks, flat heat pipe, loop heat pipes with sintered copper particles layer evaporator have been conducted [5, 6, 15]. The thin film evaporating heat transfer in those heat pipes occurred both on the flat surface and curved surface.

In order to better understand the heat transfer mechanisms in evaporator and condenser, and furthermore determine the temperature response in heat pipe, the heat transfer model of heat pipe has been developed. The prototype heat pipes of groove heat pipe with trapezoid wicks, miniature loop heat pipe without compensation chamber and flat heat pipe with wire core wicks, as well as the cryogenic oscillating heat pipe for the cell freezing have been manufactured and experimentally conducted.

1.4 Thesis Outline

This work performs the theoretical conduct the mechanisms of thin film evaporating heat transfer both on the flat surface and curved surface in evaporator and film condensation heat transfer in condenser. Experimental investigations of the groove heat pipes with trapezoid liquid wicks, loop heat pipes with flat sintered copper particle layer evaporator, and cryogenic oscillating heat pipe have been manufactured and measured. The comparisons of the theoretical prediction and experimental data have been conducted and the results show that the model predictions can agree with the experimental data very well herein.

Chapter 2 describes a detailed mathematical model for predicting the thin film heat transfer characteristics in the evaporator and its effect on the temperature drop in a grooved heat pipe with trapezoid wicks has been developed. The model includes the effects of the contact angle and the groove configuration on the temperature drop in the evaporator. An extensive experimental investigation has been conducted and the results compared with the theoretical results. For the grooved heat pipe investigated here, the temperature drop in the evaporator is much higher than that occurred in the condenser at an equivalent heat load. Chapter 3 provides detailed information about the thin film evaporating heat transfer on curved surface. The effects of gravitational force and contact angle on the thin film profiles and heat flux distribution on the curved surface are investigated. Based on the capillary limit and thermal resistance, the maximum heat transport capacity of the heat pipes is predicted. Prototypes of miniature flat heat pipe with wire core groove and loop heat pipe with flat sintered evaporator have been manufactured and experimentally investigated. While the mechanisms of the thin film evaporating heat transfer on different surface and application in maximum heat transport capacity prediction in heat pipe are the concentration in the chapters 2 and 3, Chapter 4, describes the thin film evaporating heat transfer to apply in the heat transfer process of cell freezing in details and a theoretical model to predict the transient temperature distribution with thin film evaporation heat transfer in a cell during the cyropreservation process has been developed. The analytical results show that the heat transfer coefficient significantly affects the volume fraction of crystallization, x, and as the heat transfer coefficient, h, increases, the volume fraction of crystallization and the freezing time decrease sharply. In order to obtain an ultra-high cooling rate with uniform temperature

distribution, one novel device called cryogenic oscillating heat pipe, which combined the oscillation flow to enhance the convection heat transfer with unique heat transport performance of heat pipe, also has been developed and experimentally conducted in this chapter. Finally, the conclusions and prospect works are presented in Chapter 5.

CHAPTER 2 MODELING AND EXPERIMENTAL INVESTIGATION OF HEAT TRANSFER IN GROOVE HEAT PIPES WITH TRAPEZOIDAL MICRO WICKS

2.1 Physical Model

The physical model of tube heat pipe with trapezoidal microgooves is shown in Fig.2-1. When heat is added on the evaporating section of a grooved heat pipe, the heat will transfer through solid regions of tube wall and reach the working fluid. The working fluid is vaporized and become into vapor; vapor flow passes through the adiabatic section and reaches condenser section where the condensation heat transfer occurs. The vapor flow releases the latent heat and condenses into liquid in the condenser. The condensate in the condenser will be pumped back to the evaporator by the capillary pressure along the trapezoidal microgrooves. Therefore, heat transfer in the tube heat pipe includes evaporation heat transfer in the evaporator and condensation heat transfer in condenser.

As demonstrated in the previous investigations [15, 18, 21], heat mainly passes through the thin film regions where the thin film evaporation heat transfer occurs. Therefore, the determination of the thin film profiles is very important in the thermal analysis of heat pipes. As shown in Fig.2-1, comparing the thickness δ of the liquid thin film with R (radius of the groove heat pipe), the thin film distribution can be considered as the one formed on a flatted surface since $\delta \square R$. The thin film thickness δ_y decrease with the heat load increase till it

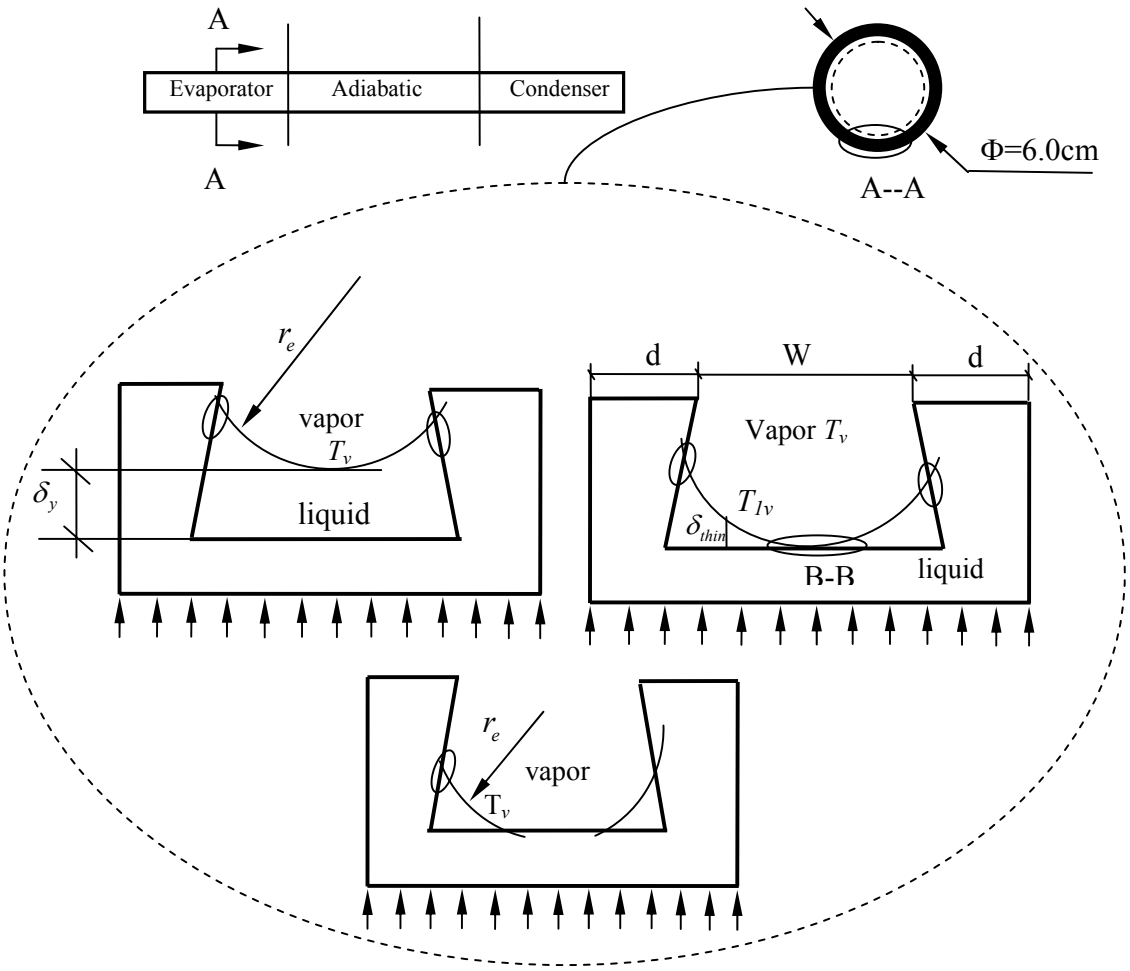

Figure 2-1 Physical model of the evaporation heat transfer on a flatted surface

reaches $\delta_y = \delta_0$ (the no-evaporation point) where no evaporation heat transfer occur because the liquid-vapor interface temperature in evaporator is equal to the wall temperature due to disjoining pressure effects.

In order to better understand the operation mechanism and predict the maximum heat transport capacity of tube heat pipes, a detailed mathematical model for predicting the thin film heat transfer characteristics in the condenser and evaporator and its effect on the

temperature drop in a grooved heat pipe has been developed in this chapter. The model includes the effects of the contact angle, disjoining pressure, surface tension and wick configuration on the interface temperature and heat flux distribution in the evaporating thin film region. The heat transfer rate effect on the temperature drop of the heat pipe is also conducted.

2.2 Heat Transfer in Evaporator

Figure 2.2 illustrates the heat transfer rate effect on the thin film profile in the evaporator. For low heat load (CASE I, $\delta_y > \delta_0$), the evaporation heat transfer mainly occurs in the two thin film regions, i.e., C-C and D-D regions. The C-C thin film region is the same as the D-D thin film region due to the groove symmetry. When the heat load increases, the new thin film region B-B forms, which ($\delta_y = \delta_0$) is defined as CASE II. Because there is no vapor-solid interface in the B-B region, the contact angle in this region should be equal to zero. Obviously, the thin film region shown in the CASE II is much longer. When the heat load continuously increases, the thin film region B-B will rupture into two triangle shaped thin film areas as shown in CASE III ($\delta_y < \delta_0$). When the heat pipe works at the CASE III, the thermal resistance and the temperature drop of the heat pipe will increase dramatically because the thin film region in the triangle-shaped area is significantly affected by by the contact angle. Therefore, when heat pipes operate in CASE II，we consider the heat load as the maximum heat transport capacity of the heat pipe.

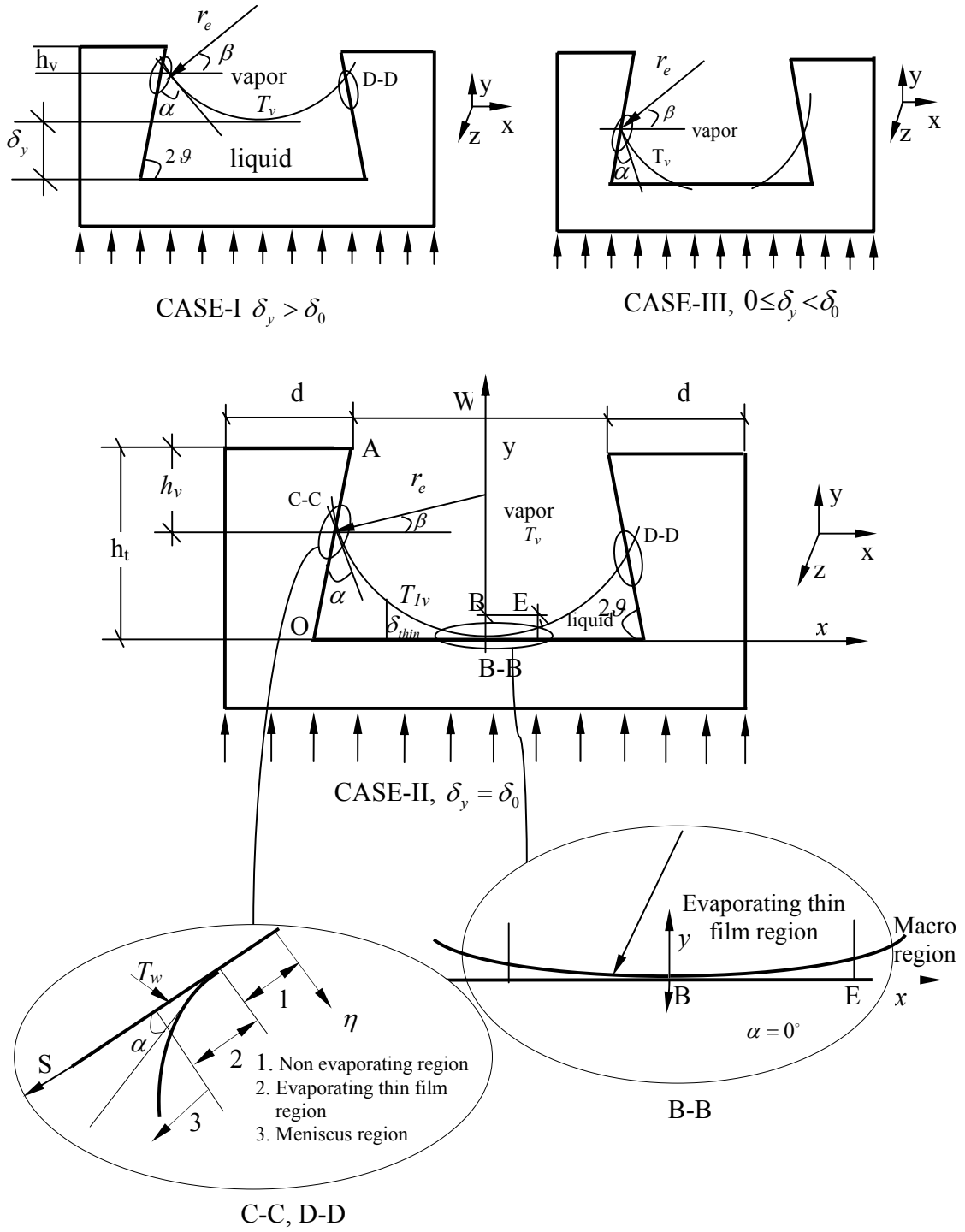

Figure 2-2 Schematic of thin film profile at different heat load

2.2.1 Meniscus Radius and Thin Film Region

As shown in Fig. 2-2, the liquid-vapor interface temperatures on those thin film regions can be depicted by the Clausius-Clapeyron equation, i.e.,

$$\left(\frac{dp}{dT}\right)_{sat} = \frac{h_{fg}}{T_{sat}\left[\left(1/\rho_v\right)-\left(1/\rho_l\right)\right]} \tag{2-1}$$

Since $\rho_l \gg \rho_v$, the effect of $1/\rho_l$ in the equation (2-1) can be neglected. Integrating from the saturated temperature T_{sat} to the interface temperature $T_{\delta,v}$ results in a relationship between the interface temperature and the saturated vapor temperature

$$T_{lv} = T_v\left[1+\left(\Delta p/\rho_v h_{fg}\right)\right] \tag{2-2}$$

where Δp can be found from

$$\Delta p = \sigma/r_{(z)} + p_d \tag{2-3}$$

For the second term, p_d can be estimated by $p_d = -A/\delta^3$ for nonpolar liquids and $p_d = -A/\delta^3 \ln\left(\delta/\bar{\delta}_0\right)$ for poplar liquids. Because the Hamaker constant A and the reference length $\bar{\delta}_0$ both depend on the solid-liquid properties, it is difficult to accurately determine these values for polar liquids such as water. To overcome this difficulty, the relationship developed by Holm and Goplen (1979) was utilized

$$p_d = \rho_l R_g T_{\delta,v} \ln\left(a\delta^b\right) \tag{2-4}$$

where, *a=1.5787, b=0.0243.* In the non-evaporating film region, as shown in Fig. 2-1, the curvature effect can be neglected due to the absence of vaporization. The interface temperature at this region will be equal to the wall temperature due to the interface thermal

resistance. Substituting Eqs. (2-3) and (2-4) into Eq. (2-2), the film thickness in this region can be obtained as

$$\delta_0 = \exp\left\{\frac{\left(T_w/T_v - 1\right)\left(h_{fg}/RT_w\right) - \ln a}{b}\right\} \tag{2-5}$$

Based on the definition of contact angle α and configuration of liquid wicks, as shown in Fig. 2-2, the meniscus radius, $r_{(z)}$ can be calculated by

$$r_{(z)} = \frac{\frac{W\sin 2\vartheta}{2} + \left(h_t - \delta_y\right)\cos 2\vartheta}{\cos\beta\sin 2\vartheta + \left(1-\sin\beta\right)\cos 2\vartheta} \tag{2-6}$$

where,

$$\beta = \alpha - \left(\frac{\pi}{2} - 2\vartheta\right) \tag{2-7}$$

$$h_v = h_t - \left[\delta_y + r_{(z)}\left(1-\sin\beta\right)\right] \tag{2-8}$$

When the Bond number is very small, the meniscus radius shown in Eq. (2-6) only depends on the contact angle, the thickness of non-evaporating δ_0, and the groove configuration. The film thickness for both the C-C and D-D regions can be written as

$$\delta_{C-C} = \delta_{D-D} = \frac{W}{2} + ctg2\vartheta\left(h_t - y\right) - \sqrt{r^2 - \left[y - \left(r_{(z)} - \delta_0\right)\right]^2} \tag{2-9}$$

where

$$\begin{aligned} &y = r_{(z)}\left(1-\sin\beta\right) + \delta_0 \\ &\delta_0 \le y \le r_{(z)}\left[1-\sin\beta\right] + \delta_0 \\ &\delta = \delta_0,\ r_0 \to \infty,\ T_{\delta,v} = T_w;\ \text{at } s = 0 \end{aligned} \tag{2-10}$$

The film thickness variation for the B-B region can be found as

$$\delta_{B-B} = \left(r_{(z)} + \delta_0\right) - \sqrt{r_{(z)}^2 - x^2} \tag{2-11}$$

where

$$\begin{aligned} &-r_{(z)}\cos\beta \le x \le r_{(z)}\cos\beta \\ &\delta_{B-B} = \delta_0, \quad r_{(z)} \to \infty,\ T_{\delta,v} = T_{w,} \quad at \quad x = 0 \end{aligned} \tag{2-12}$$

Heat transfer through the thin film region can be considered as one-dimensional heat conduction. Based on above assumption and the coordinates shown in Fig. 2-2, the heat flux and total heat transfer through three thin film regions can be calculated by

$$q = k\frac{\Delta T}{\delta} = k\frac{T_w - T_{\delta,v}}{\delta} \tag{2-13}$$

$$Q_{Micro} = 2N\left[\int_0^x k\frac{T_w - T_{\delta,v}}{\delta_{B-B}} L_{\text{evaporator}}\,dx + \int_0^s k\frac{T_w - T_{\delta,v}}{\delta_\eta} L_{\text{evaporator}}\,ds\right] \tag{2-14}$$

The second term on the right side of Eq. (2-14) can be expressed by

$$-\int_{r_{(z)}\left[1+\cos(2\vartheta+\alpha)\right]+\delta_0}^{y} k\frac{T_w - T_{\delta,v}}{\delta_{C-C}\sin 2\vartheta} L_{\text{evaporator}}\,dy \tag{2-15}$$

2.2.2 Heat Transfer through Macro Region

Because the groove as shown in Fig. 2-2 is very small and the Bond number ($B_o = \sqrt{\dfrac{g\left(\rho_l - \rho_v\right)D^2}{\sigma}}$) is much less than 1, the temperature distribution in the macro liquid film region can be described by the two-dimensional, steady-state heat conduction equation,

$$\frac{\partial^2 T}{\partial x^2} + \frac{\partial^2 T}{\partial y^2} = 0 \tag{2-16}$$

Although the geometry is not regular, the solution for Eq. (2-16) can be readily obtained by the FLUENT software, and the total heat transfer through the macro region can be easily obtained. In this region, the effect of disjoining pressure on the interface temperature can be neglected. The interface temperature can be determined by

$$T_{\delta,v} = T_v \left(1 + \frac{\sigma}{r_{(z)} \rho_v h_{fg}} \right) \tag{2-17}$$

A number of grid numbers have been employed in order to obtain the grid-independent solutions. And finer grids near the evaporating thin film region were used. Using Eq. (2-17) for the liquid-vapor interface temperature, the heat transport Q_{mac} through the macro region of liquid for a given superheat can be calculated. The total heat transport from the solid wall to the liquid can be determined by

$$Q_{tot} = Q_{macro} + Q_{micro} \tag{2-18}$$

where, Q_{micro} can be calculated by Eq. (2-14) for a given superheat.

2.3 Capillary Limitation

In order to determine the temperature drops in the evaporator and condenser, the meniscus radius variation from the evaporator to the condenser must first be determined. For a heat pipe operating in steady state, a given heat transport will determine the meniscus radius variation from the cap end of the evaporator section to the radius in the condenser section. To simplify the calculation, the average radii at the evaporator and condenser are considered. In order to pump the condensate back to the evaporating section for a given heat input, the capillary pressure must be equal to the summation of the total pressure drops, i.e.,

$$\sigma\left(\frac{1}{r_e}-\frac{1}{r_c}\right)=\left[\frac{4f_l Re\mu_l}{2D_{h,l}^2}\cdot\frac{Q_{tot}}{N\rho_l A_{ac}h_{fg}}+\left(\frac{f_v Re_{h,v}\mu_v}{2r_{h,v}^2 A_v\rho_v h_{fg}}\right)Q_{tot}-\rho_l g\sin\phi\right]L_{eff} \qquad (2\text{-}19)$$

Where

$$\begin{aligned}
&L_{eff}=\frac{L_e}{2}+L_a+\frac{L_c}{2}\\
&\beta=\alpha+2\vartheta-\frac{\pi}{2}\\
&r_{h,v}={}^{4A_v}\!\Big/\!_{P_v}\\
&A_v=\pi R_{in}^2+A_{ac}-A_{ae}\\
&P_v=\pi R_{in}+N\left[2r_e\left(\frac{\pi}{2}-\beta\right)+\frac{h_v}{\sin 2\vartheta}\right]\\
&h_v=h_t-\left[\delta_y+r_e\left(1-\sin\beta\right)\right]
\end{aligned} \qquad (2\text{-}20)$$

Since the cross-sectional area of the liquid flow in the condenser is different from that occurring in the evaporator, A_{ac} and $D_{h,l}$ for single groove channel in the condenser can be written as

$$\begin{aligned}
&A_{ac}=h_t\left(W+h_t ctg2\vartheta\right)\\
&D_{h,l}={}^{A_{ac}}\!\Big/\!_{\left(\frac{h_t}{\sin 2\vartheta}+W+h_t ctg2\vartheta\right)}
\end{aligned} \qquad (2\text{-}21)$$

For the evaporator, the cross-sectional area of the liquid fluid flow for single groove channel can be expressed as

$$A_{ae}=\left(h_t-h_v\right)\left[W+2r_e\cos\beta+2\left(h_t-h_v\right)ctg2\vartheta\right]-r_e^2\left(\frac{\pi}{2}-\beta-\cos\beta\sin\beta\right) \qquad (2\text{-}22)$$

and it should be noted that the meniscus radius in the evaporator is assumed to be equal to a constant for a given heat transport load, which can be determined by equation (2-6).

As shown in Eq. (2-6), r_e is dependent on the configuration parameters of the micro groove, the contact angle, and δ_y for a given grooved heat pipe. For the condensate flow in an open trapezoidal groove, the results by Kim et al. (2003) can be used as follows:

$$f_l Re = 14.11\alpha^{0.06009} \times \exp\left\{-0.5 \times \left[\left(\log\frac{K}{22.22\alpha^{-0.3366}}\right) \Big/ \left(2.083\alpha^{0.0372}\right)\right]^2\right\} \quad (2\text{-}23)$$

where, $K = h_t \Big/ \left(W + 2h_t ctg2\vartheta\right)$.

On the other hand, the flow mass can be determined using additional conditions. It should equal to the charged working fluid flow mass and keep constant. In this model, the flow mass can be calculated as follows

$$m_{tot} = N\rho_l \left[L_c A_{ac} + L_e A_{ae} + 0.5L_a \left(A_{ac} + A_{ae}\right)\right] + \rho_v A_v \left(L_c + L_a + L_e\right) \quad (2\text{-}24)$$

2.4 Heat Transfer in the Condenser

As shown in Fig. 2-3, the pressure gradient in the condensate film can be found as

$$\frac{dP_{l\delta}}{dx} = \frac{4f \cdot \frac{1}{2}\rho \bar{u}_\delta^2}{\delta} = \frac{4fRe_\delta \mu \bar{u}_\delta}{2\delta^2} \quad (2\text{-}25)$$

where

$$Re_\delta = \frac{\delta\rho\bar{u}_\delta}{\mu}, \text{ and } \bar{u}_\delta L_c \delta\rho_l = m_s = \frac{q_s}{h_{fg}} = \frac{Q_{mic}}{Nh_{fg}} \quad (2\text{-}26)$$

Substituting Eq. (2-26) into Eq. (2-25) and integrating Eq. (2-25), the pressure drop can be determined, and this value is equal to the capillary pumping pressure i.e.,

$$\Delta P_{l\delta} = \int_0^{\frac{W}{2}} \frac{2 f Re_\delta \mu}{\delta^3} \frac{q_s}{L_c \rho h_{fg}} dx = \frac{f Re_\delta \mu W Q_{mic}}{N \delta^3 L_c \rho h_{fg}} = \frac{\sigma}{r_c} \tag{2-27}$$

where, $f Re_\delta = 6$, and r_c can be determined from Eq. (2-19) with Eq. (2-6) for a given heat transport. The thickness of thin film in the condenser can be calculated by Eq. (2-27). Therefore, the condensation heat transfer Q_{mic} through the thin film region can be calculated by

$$Q_{mic} = 2N \int_0^{L_C} \int_0^{W/2} k \frac{T_w - T_{\delta,v}}{\delta} dx dz \tag{2-28}$$

It is assumed that the δ is constant in the condenser wall shown in Fig. 2-3. Thus, the temperature drop in the condenser can be obtained

$$\Delta T = Q_{mic} \delta \Big/ \left(N k L_c W \right) \tag{2-29}$$

where, $\Delta T = T_{sat} - T_W$

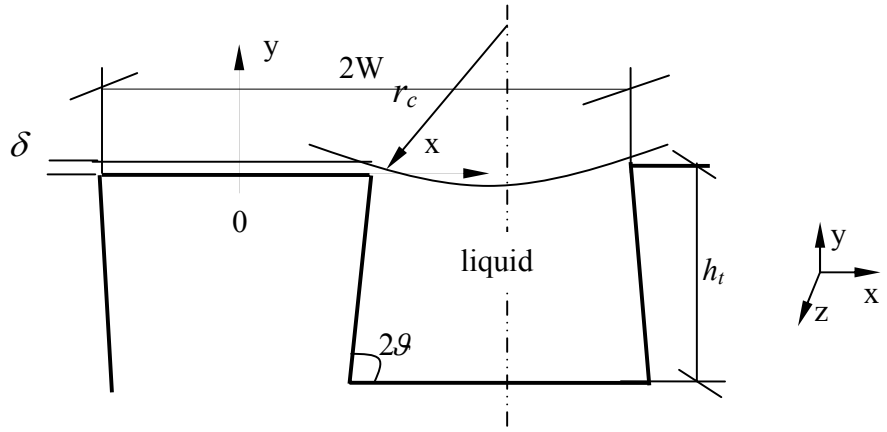

Figure 2-3 Film condensation heat transfer in the condenser

2.5 Theoretical Results and Discussion

The disjoining pressure and interface curvature significantly affect the film thickness variation, interface temperature, and heat flux distribution. In order to better illustrate effects on the meniscus radius, heat flux distribution and heat transfer, a trapezoidal groove similar to the one shown in Fig.2-2 is considered in the current model with the thermophysical properties of copper and pure saturated water at 60^0C. The detailed dimensions of the grooves include $2W$=0.262 mm, h_f=0.195 mm, L_e=60 mm, L_a=45 mm, L_c=30 mm, $2\vartheta = 75.8$ deg, R_{in}=2.5 mm, and the groove number = 60. The heat pipe was charged with 0.508 g of pure water.

2.5.1 Contact Angle Effects

Figure 2-4 illustrates the contact angle effect on the meniscus radius including the superheat

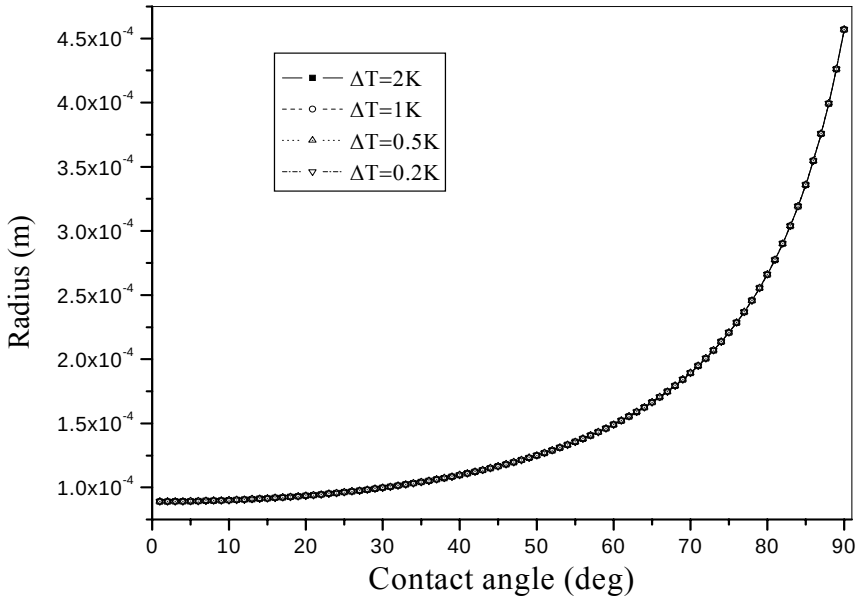

Fig. 2-4 Meniscus radiuses versus contact angle

effect on the nonevaporating film thickness. As shown, the meniscus radius increases nonlinearly as the contact angle increases. For example, when the contact angle changes from α=0° to α=30°, the radius changes slowly and the ratio of the meniscus radius at α=30° to the one at α=0° is equal to 1.12, while the ratio of the meniscus radius at α=90° to the one α=60° is 3.07. It shows that when the contact angle is less than 30°, the further decrease of the contact angle will not significantly further reduce the meniscus radius. As shown in Fig. 2-4, the model cannot predict the effect of superheat ($T_w - T_e$) on the meniscus radius.

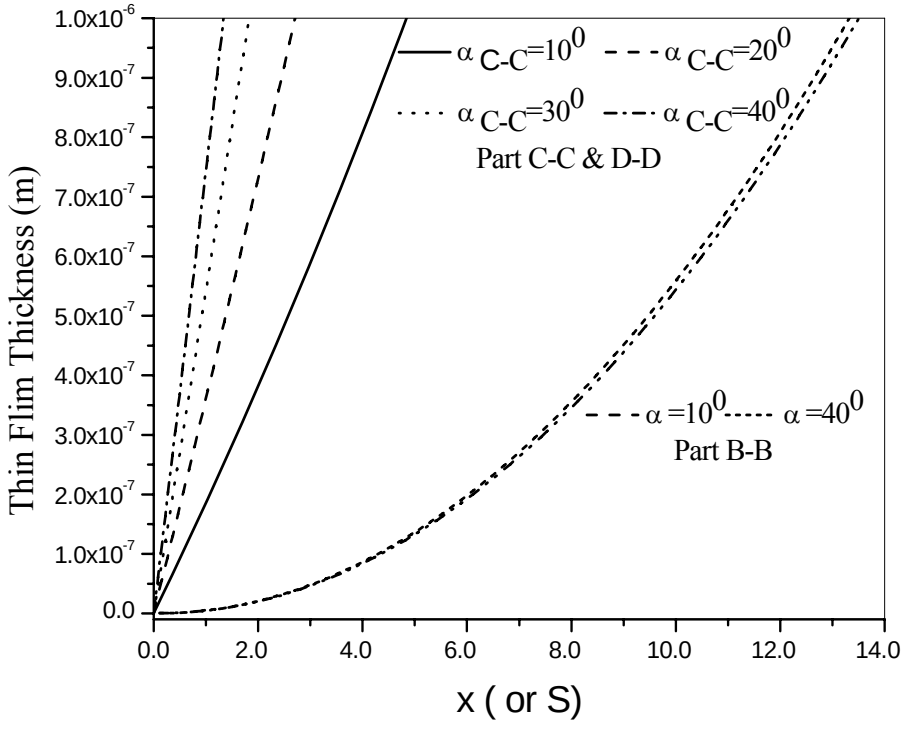

Fig. 2-5 Contact angle effect on liquid film profiles

Figure 2-5 shows the contact angle effect on the thin film profiles in both the C-C (or D-D) and B-B regions. As shown, the thin film thickness profile in the C-C (or D-D) region largely

depends on the contact angle, while the thin film profile in the B-B region is almost unchanged when the contact angle varies from 10° to 40°. If the cut-off film thickness for the thin film region is δ=1 μ, for example, the thin film region length decreases from 13.5 μ and 13.4 μ for the B-B region when the contact angle increases from α=10° and 40°. As the contact angle increases, however, the thin film profile for the C-C (or D-D) region varies very sharply. With the same cut-off film thickness of δ=1 μ for the thin film region, the thin film length decreases from 4.8 μ to 1.33 μ as the contact angle increases from $\alpha = 10°$ to 40°. As shown in Fig. 5, the thin film region length of the B-B region is about 2.8-10 times of the one in the C-C region.

Once the thin film profile is given, the heat flux distribution through the thin film regions shown in Fig. 2-6 can be obtained. As the interface temperature at the liquid-vapor interface varies from $T_{lv} = T_w$ at the non-evaporating film region to $T_{\delta,v} = T_v\left[1+\sigma\Big/\left(r_{(z)}\rho_v h_{fg}\right)\right]$ in the evaporating thin film region, the effect of the disjoining pressure diminishes to zero. In the C-C or D-D thin film region, the contact angle variation directly affects the thin film profile and the heat flux distribution through the thin film region. Although the highest heat flux is nearly the same, the total heat transfer through the thin film region increases as the contact angle decrease. As shown in Fig. 2-6(b), the effect of contact angle on the heat flux profile and maximum heat flux can be negligible for the B-B thin film region. Comparison of the results shown in Fig. 2-6(a) with those in Fig. 2-6(b) indicates some of common characteristics of heat flux distribution for the B-B and C-C regions. The heat fluxes for both regions are initially zero at the origin point where the film thickness is

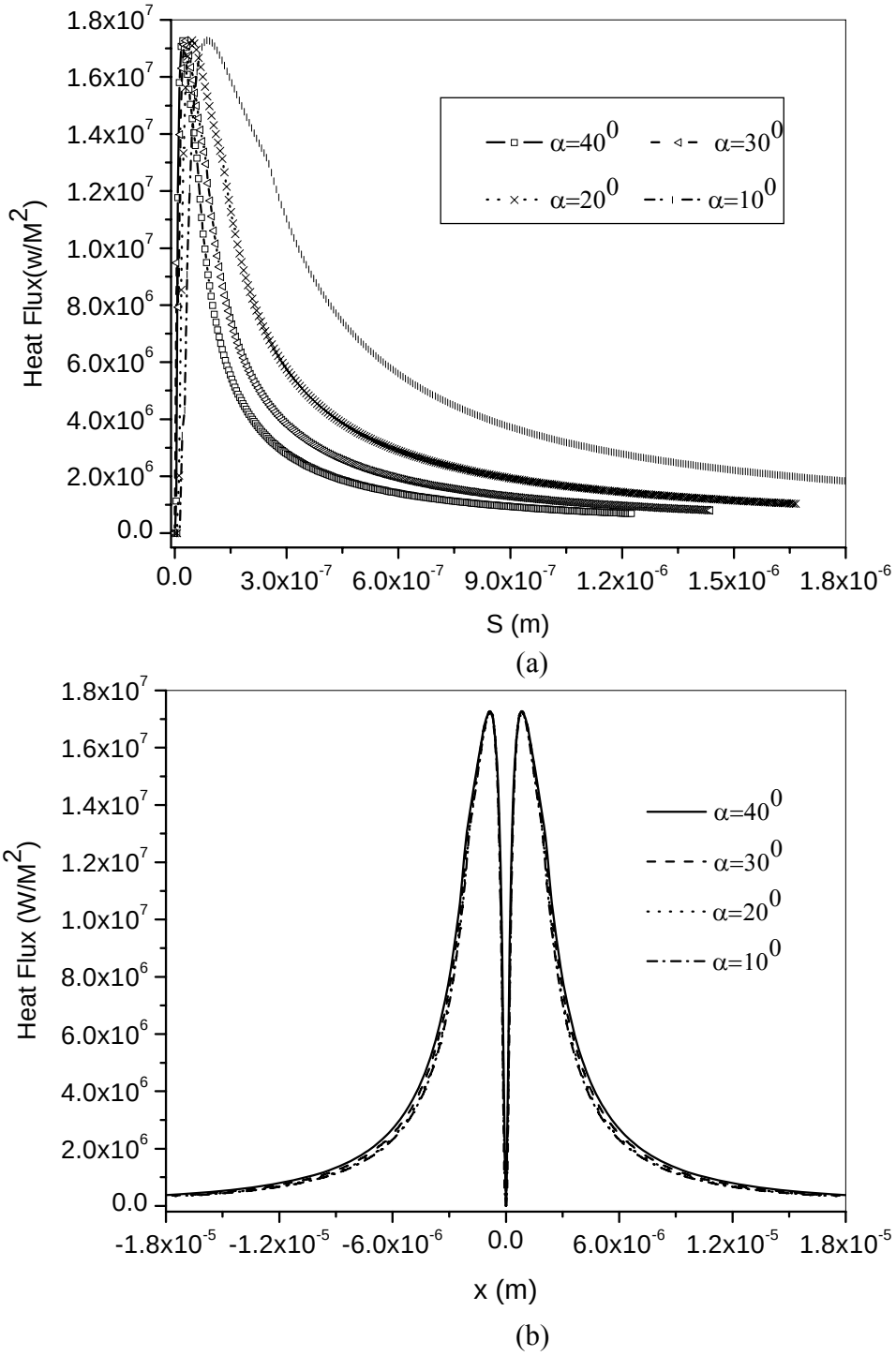

Fig. 2-6 Contact angle effect on heat flux distributions (T_w-T_e =1K). (a)C-C or D-D thin film region, (b) B-B thin film region

equal to δ_0, and then increase dramatically as the film thickness increases. After getting the maximum heat flux, the heat flux through the thin film decreases quickly along the x (or s) direction until it reaches the meniscus region.

2.5.2 Disjoining Pressure Effects

As shown in Figure 2-7 (a) and (b), the superheat and disjoining pressure drop signifcnatly affect heat transfer through the thin film region at the same contact angle. When the temperature difference between the groove wall and saturate vapor increases, the heat flux increases and the heat transfer rate through either B-B or C-C(D-D) region enhances. On the other hand, as shown in Eqs. (2-2) and (2-3), the temperature difference between the wall temperature (T_w) and interface temperature T_{lv} at the liquid vapor interface decreases due to the disjoining pressure in the thin film region. The heat flux profiles in the region from the nonevaporation region to the highest heat flux location directly illustrate that the disjoining pressure plays more important role in the thinner film region.

2.5.3 Temperature Distribution in Macro Region

The temperature distribution and heat transport through the macro region from the wall to the vapor phase can be readily obtained by the FLUENT software. Figure 2-8 illustrates the liquid film profile and the temperature distribution in the macro region of the liquid film at different cases. As shown in Fig. 2-8(a), the larger temperature gradient mainly creates in the C-C (D-D) region, and clearly the evaporation heat transfer occurs in those regions. The temperature difference between two isotherms shown in Fig. 2-8(b) is equal to 0.05K at

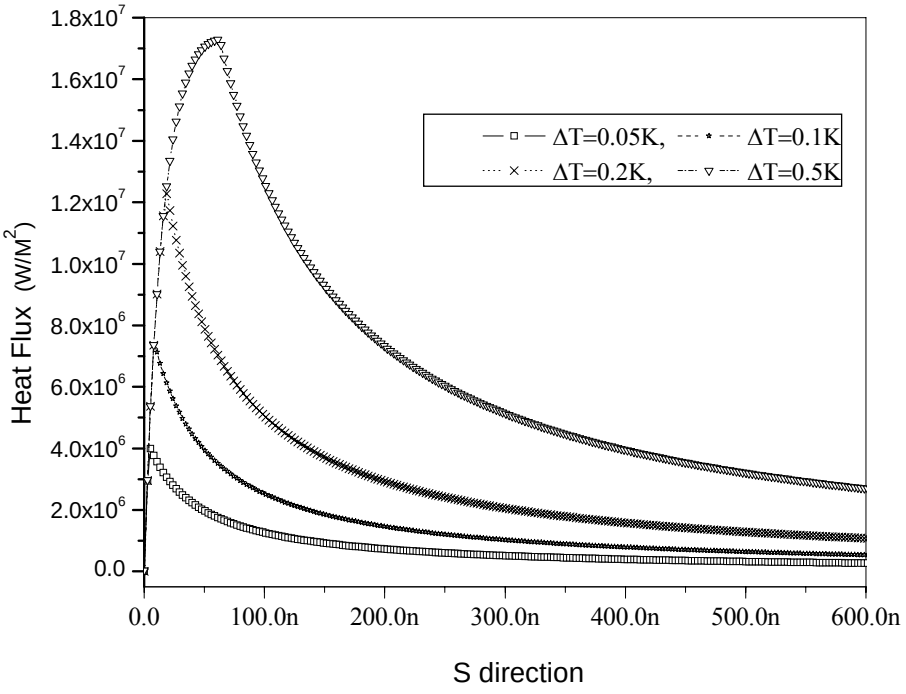

(a)

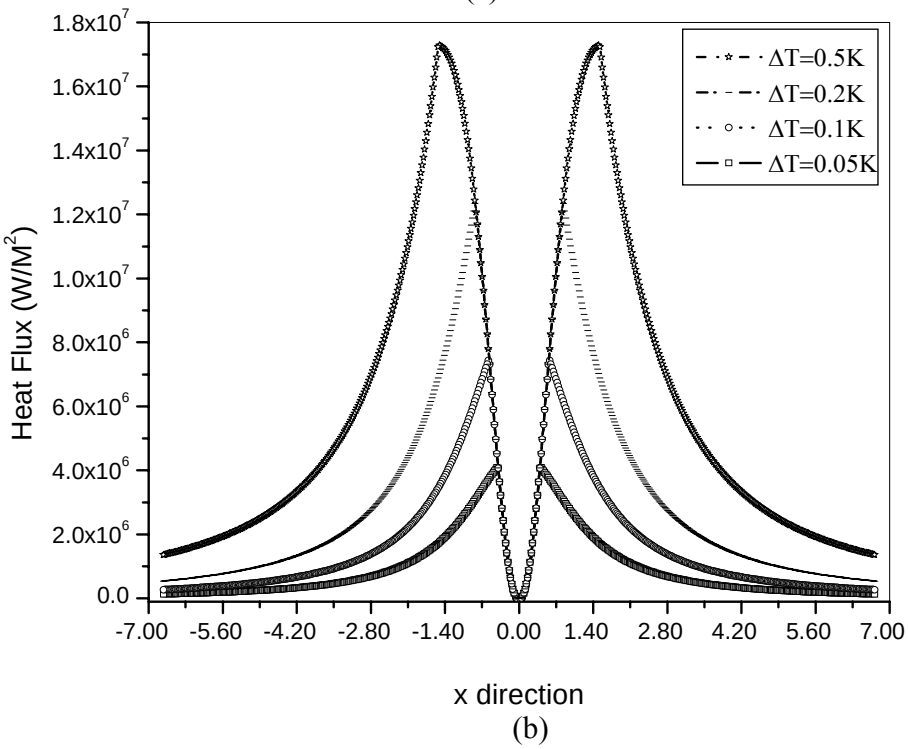

(b)

Fig. 2-7 Superheat and disjoining pressure effects on the heat flux distribution at the same contact angle (a) B-B part (b) C-C(D-D) parts

CASE II. For CASE II, the largest temperature gradient existing in the thin film evaporation region creates ultra-high heat flux, and the thin film region in the B-B part is much larger than that in C-C(D-D) parts. Comparing Figure 2-8 (a) and (b), the evaporation heat transfer occur in the B-B region is stronger than that in the region C-C.

As presented above, the B-B thin film region plays an important role and the total heat transfer through this region is much larger than that through the C-C or D-D region. Therefore, the B-B thin film region is a key determining the maximum evaporating heat

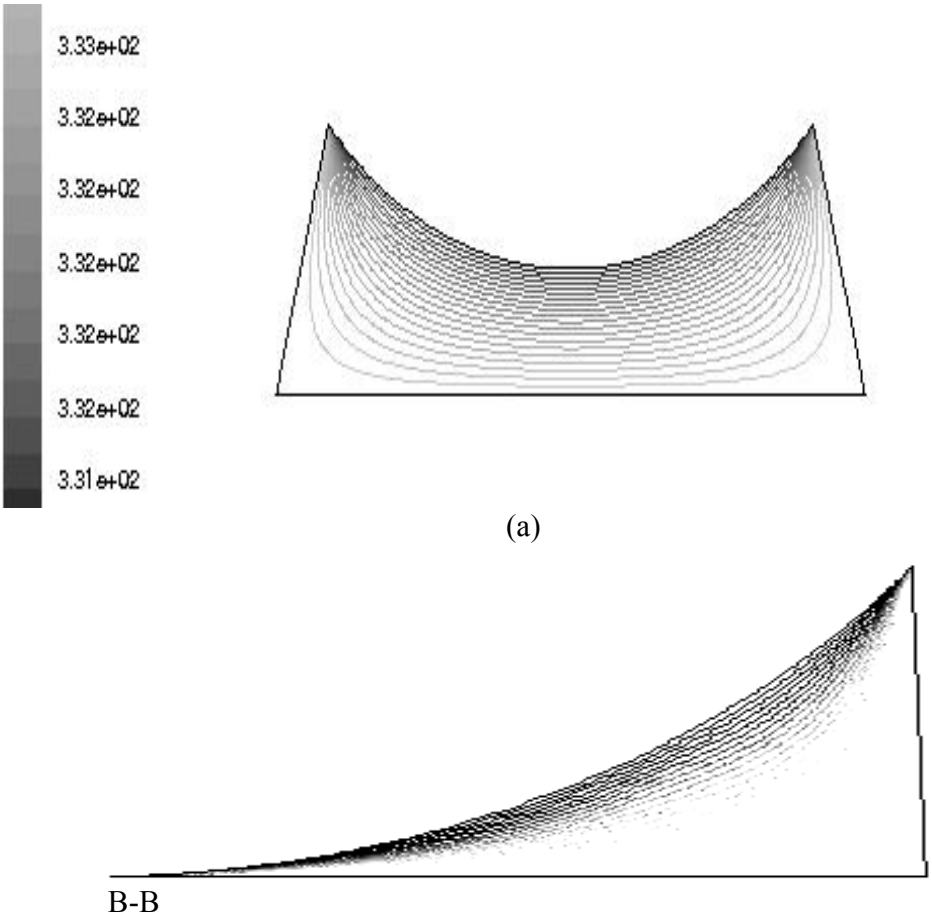

Fig. 2-8 Isotherms in the liquid films (a) CASE I (b) CASE II (temperature difference between two isotherms is 0.05K, $\Delta T = 1K$)

transfer in the evaporator, and the total effective thermal conductivity of the whole heat pipe. In addition, the contact angle has a little effect on the B-B thin film region and can be neglected. The effects of contact angle on the thin film profile and heat flux distribution for the C-C or D-D region, however, is significant.

2.5.4 Superheat Effect on Q_{micro}/Q_{tot}

Due to the high heat flux occurring at the evaporating thin film, the micro regions are of significant interest. The superheat between the wall and the vapor, $T_w - T_{lv}$, drastically affects the thin film profile and heat flux profiles. Therefore, the superheat will significantly affect the heat transfer rate through both regions. Figure 2-9 illustrates the superheat effect on the ratio of the heat transfer through the thin film region, Q_{micro} to the total heat transfer, Q_{tot}, i.e., Q_{micro}/Q_{tot} at CASE II. As shown in Figure 2-9, when the superheat increases, the ratio, Q_{micro}/Q_{tot}, decreases. And it depends on the contact angle. When the contact angle increases from 10° to 30°, as illustrated in Fig. 2-9, the ratio decreases, for example, from 87.0% to 75.9% for a superheat of 2.0 K, and shows that the ratio, Q_{micro}/Q_{tot}, at $\alpha = 10°$ is larger than that at $\alpha = 30°$. There are mainly two reasons resulting in the ratio decrease when the superheat increases. One of them is that the thin film region in the C-C or D-D region has been extended and heat transfer through those regions enhanced when the contact angle decrease. Another of them is that: the mass flow rate of liquid flow in thin film region directly depends on the heat flux distribution, which is function of the superheat. There exists a higher heat flux at higher superheat; the evaporation rate must increase over the micro

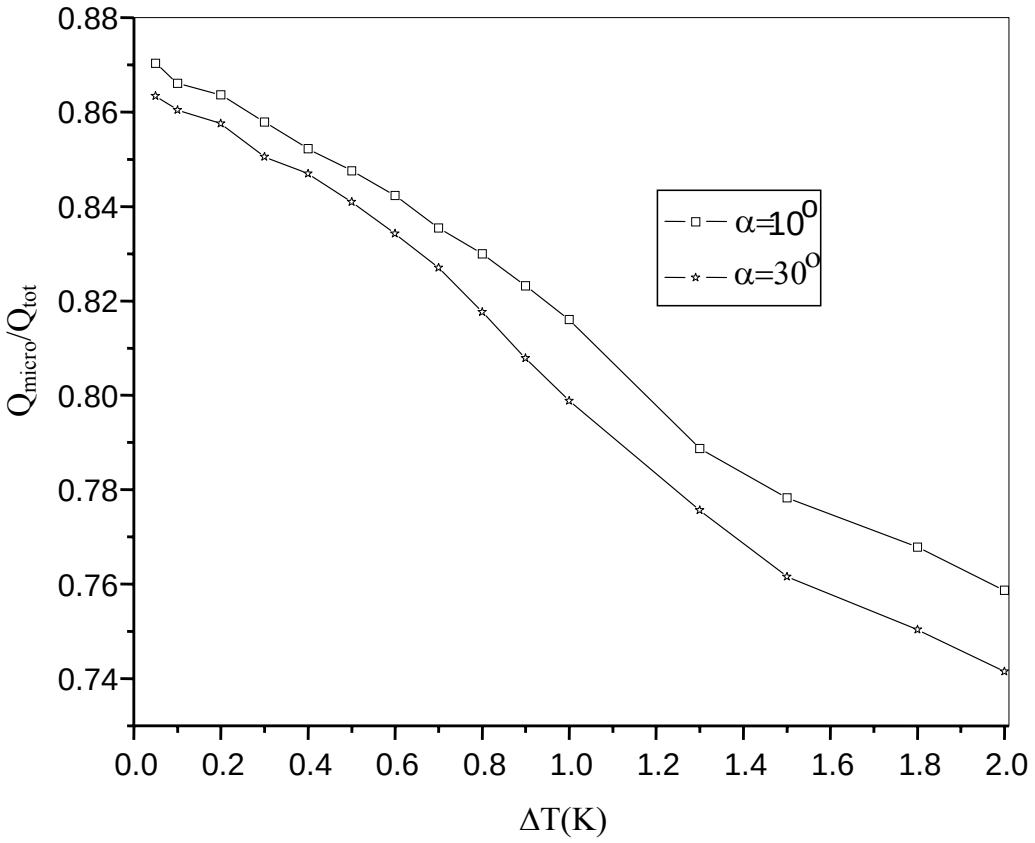

Fig. 2-9 Contact angle effect on Q_{micro}/Q_{tot}

region. This causes the mass flow rate through the thin film region to increase, resulting in the pressure loss to increase over a given length due to viscous forces. In order to maintain a steady-state evaporating heat transfer over this length, the pumping pressure due to the disjoining pressure effect must compensate for the viscous pressure drop and the pressure variations due to the curvature effect as the curvature aids in pulling liquid to the bulk liquid region. Therefore, the ratio, Q_{micro}/Q_{tot} , will decrease since the length of the evaporating thin film region decreases when the temperature difference increases.

2.5.5 Temperature Response in the Evaporator and Condenser

The heat transfer rate effect on the temperature response in the evaporator can be predicted by the present model. It should be noted that the following assumptions are made in the calculation: 1) The vapor flow is saturated and considered as ideal gas. 2) The meniscus radius of liquid-vapor interface in the wicks is constant at a given heat load. 3) When the film thickness increases, the disjoining pressure effect decreases until it is so small that it can be neglected. The length of the thin film region is determined by the cut-off value of 0.015 Pa of disjoining pressure. 4) As shown in Fig.2-2, the contribution of the heat transfer through region (B-B) at Case I is negligible since the thermal resistance is very large due to the thick

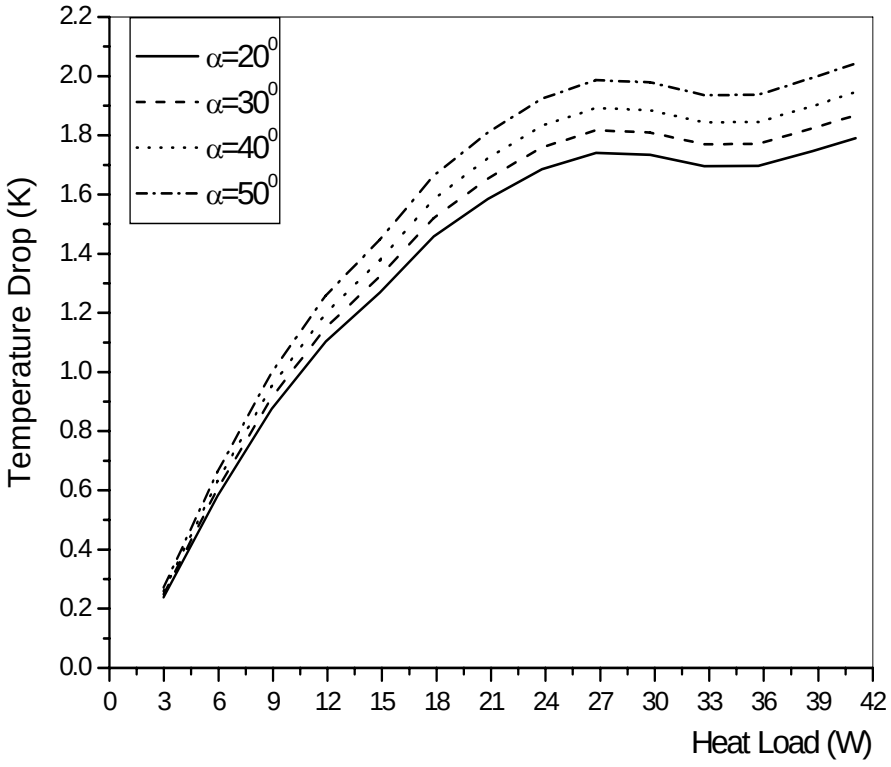

Figure 2-10 Temperature drop versus heat load in the evaporator

liquid film. But when the heat load increases, the liquid film thickness becomes thinner and thinner, the contribution of the heat transfer through the region (B-B) should be considered. In the calculation of evaporation heat transfer, the heat passing through the region (B-B) has been added when the film thickness $\delta_f = 0.05mm$ until δ_f reaches δ_0 . If the heat load continues to increase after δ_f reaches δ_0 , the Case III situation is used to predict the temperature response in the evaporator since the heat transfer performance of heat pipe is becoming worse. As shown in Fig. 2-10, the temperature drop is different at the same heat load depending on the contact angle. It can be concluded that the contact angle plays an important role in determining the radius. The meniscus radius decreases with the contact angle decreasing and directly increases the capillary pumping ability and heat transport capability. More importantly, as the contact angle decreases, the thin film region is enlarged and effectively enhances the heat transport capability, resulting in a smaller temperature drop in the evaporator for a same heat load. On the other hand, when the heat load is large enough and $\delta_y = \delta_0$, the heat transfer has been dramatically enhanced. As a result, the temperature drop does not increase, but rather decreases as the heat load increases.

As shown in Fig. 2-11, the temperature drop in the condenser varies nonlinearly at a low heat load but nearly linearly as the heat load increases. The temperature drop in the evaporator, as shown in Figs. 2-11 and 2-11, is much higher than that in the condenser at a given heat load. For example, as $Q_{tot} = 18\,W$, $\Delta T_e = 1.52$K at $\alpha = 30^o$ in the evaporator and $\Delta T_c = 0.14K$ in the condenser, respectively. The prediction shown above also indicates that the optimum design of the evaporator is more important than that of condenser since the

evaporator plays a more important role in a heat pipe system. One explanation is that the condenser length is twice the evaporator length and the thin film region in the condenser is much larger than that in the evaporator.

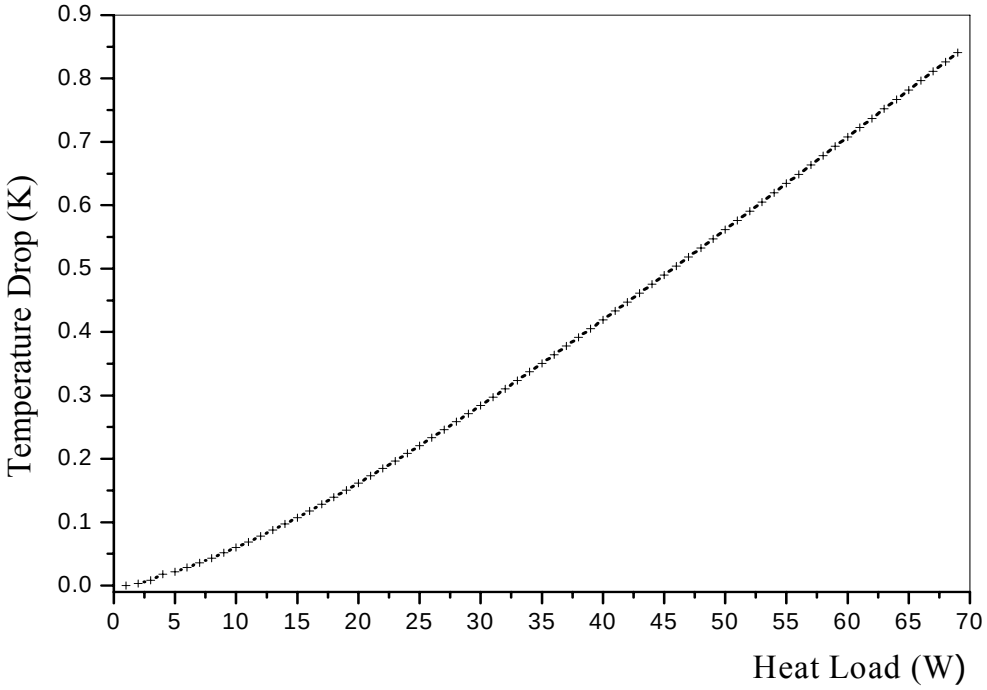

Figure 2-11 Temperature drop versus heat load in the condenser

2.6 Experimental Investigation of Groove Heat Pipes

In order to verify the model prediction, a prototype of copper-tube heat pipe shown in Fig. 2-12 has been developed and manufactured. As shown in Fig. 2-12, the dimensions of groove heat pipe was the same as the theoretical analysis. The fin number was 60 to form 60 wicks, which dimensions are the same as used in the theoretical analysis. Height of the fin (height of wicks) was 0.0195cm and the wall thickness was 0.0305cm, the charge liquid amount was

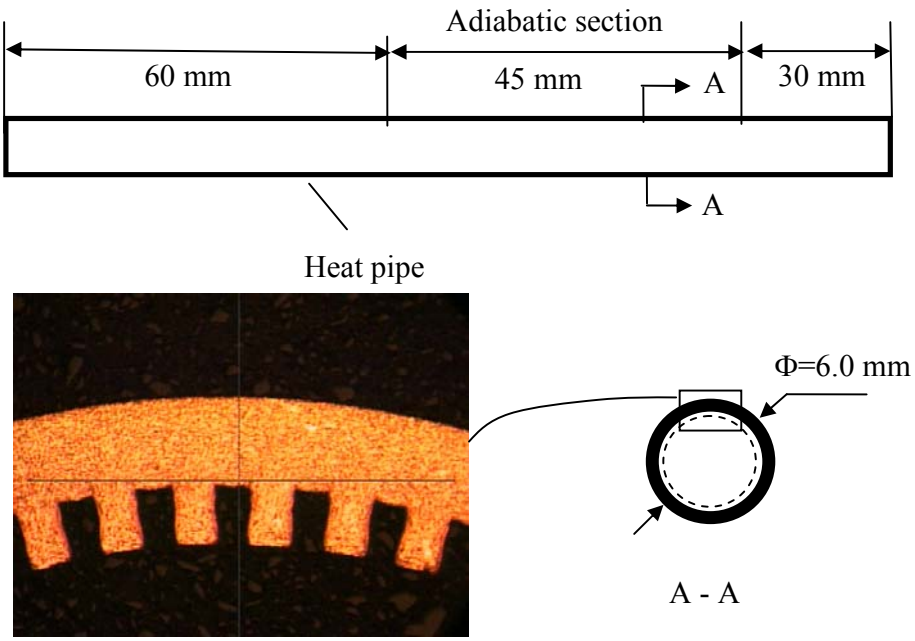

Figure 2-12 Prototype of groove heat pipe with trapezoidal micro wicks

0.508g. The schematic of experimental system was illustrated in figure 2-13. The system consisted of a test section, constant temperature circulator, power supply and measurement unit, and data acquisition system, which could be used to measure the heat transfer performance of a heat pipe. As shown in Fig. 2-13, the heat load was added on the evaporator through a copper block, wrapped by a heating coil (FAST HEAT BB010002, 200 W, 120 V) with a diameter of 1″. The input power was supplied by a power supply and recorded by a multimeter. A Julabo water chiller – constant temperature circulator was used to keep the operating temperature equal to 60.0 ± 0.2 °C. Water circulates through ¼ inch diameter polyethylene tube to and from a cooling chamber where a condensing section was placed. Six T-type thermocouples (three on the evaporating section, two on the condenser, and one on the adiabatic section) were used to measure the temperature distribution on the heat pipe.

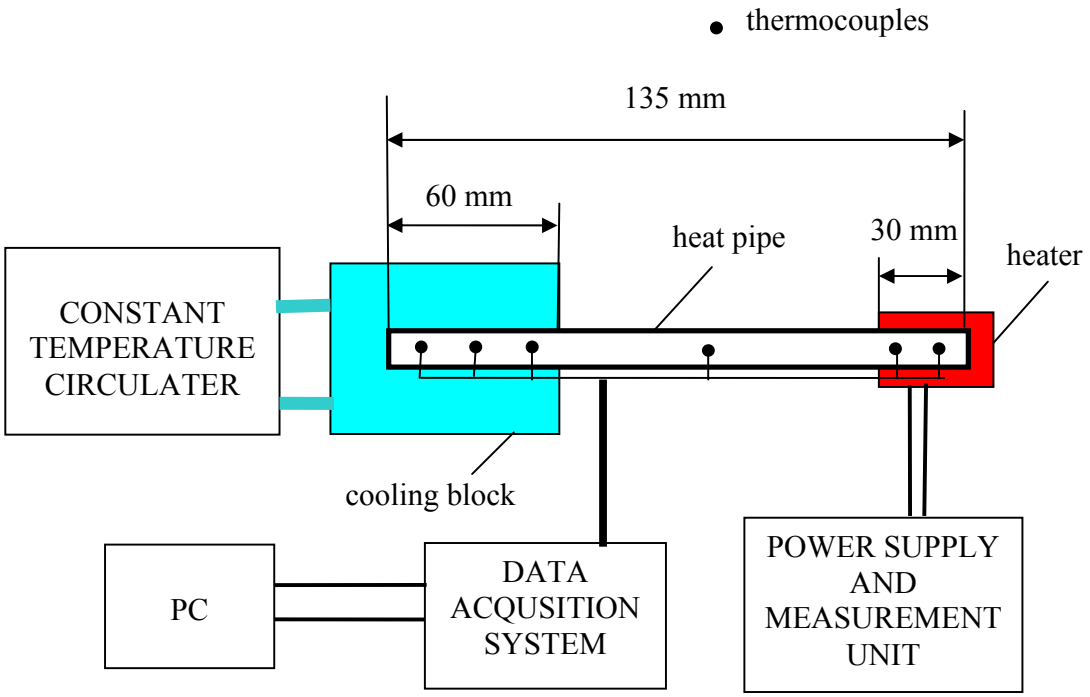

Figure 2-13 Schematic of the experimental system

A series of thermocouples were attached to the heat pipe, which led to an IO/Tech Personal DAQ56 data acquisition system controlled by a personal computer. The most important results of the experiment were the resulting temperature differences between the evaporator and the condenser

$$\Delta T = \left(\frac{T_{e,1} + T_{e,2} + T_{e,3}}{3} \right) - \left(\frac{T_{c,1} + T_{c,2}}{2} \right) \qquad (2\text{-}30)$$

Where, $T_{e,1}$, $T_{e,2}$, and $T_{e,3}$ represent the thermocouple measurements in the evaporator and $T_{c,1}$ and $T_{c,2}$ in the condenser.

The experimental results of temperature difference between evaporator and condenser have been compared with the theoretical prediction, which the contact angle selected 30

degree, as shown in Fig. 2-14(a). In the low heat load region, the numerical results are in good agreement with the experimental results. However, as the heat load increases, the theoretical results deviate from the experimental results. The experimental results show a step function increase as the heat load approaches 26 W, while the respective jump in the theoretical results occurs as the heat load reaches 33W. The main reason for this is that the liquid film δ_y becomes thinner as the heat load increases and part heat load pass through the B-B thin film region. When the heat load is large enough till δ_y reached δ_0, the heat load pass through the B-B thin film region reached maximum value and the heat transfer in this case has been dramatically enhanced. As a result, the temperature does not increase while the heat load increases. But the heat load continue increasing, the thin film region of B-B will break into two parts to form two triangular grooves, which the thin film evaporation heat transfer in triangular groove has been widely theoretically conducted by Ma and Peterson [9]. Figure 2-14(b) displays a comparison of the thermal resistances between the theoretical prediction and experimental results. As shown, the theoretical prediction accurately predicts the thermal resistance jump as observed in the experimental investigation. The minimum thermal resistance exists and should occur when $\delta_y = \delta_0$, as shown in CASE II of Fig. 2-21, if the heat load continues to increase, the thin film becomes so thin that it will rupture and separate into two triangle liquid regions as shown in CASE III in Fig. 2-2, where the thermal resistance increases sharply. This minimum thermal resistance can be called the minimum thermal resistance limitation in the design of heat pipes. Alternatively, the heat pipe can continue to function for this case, but the temperature drop increases sharply, namely, its performance decrease dramatically.

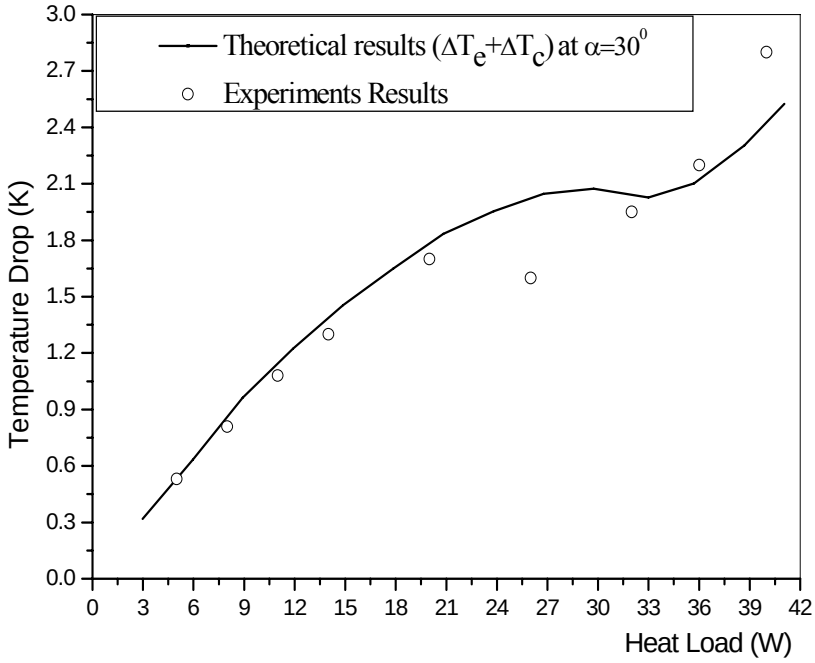

(a) Temperature difference

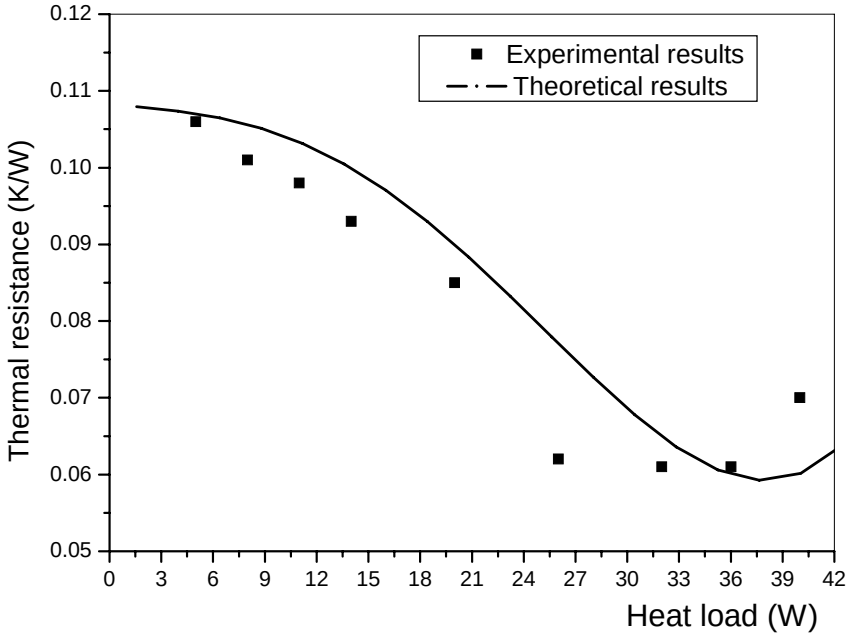

(b) Thermal resistance

Figure 2-14 Comparison of the theoretical analysis and the experimental results

2.7 Summary

A detailed mathematical model for predicting the thin film heat transfer characteristics in the condenser and evaporator and its effect on the temperature drop in a grooved heat pipe has been developed. The model includes the effects of the contact angle and the groove configuration on the temperature drop in the evaporator. An extensive experimental investigation has been conducted and the results compared with the theoretical results. The results indicate that the theoretical results predicted by the current model are in good agreement with experimental results. For the grooved heat pipe investigated here, the temperature drop in the evaporator is much larger than in the condenser at an equivalent heat load. In order to further enhance the heat transport capability in a grooved heat pipe it is more important to further decrease the temperature drop in the evaporator.

The results also show that while the decrease in the contact angle decreases the meniscus radius and directly increases the capillary pumping capability and heat transport capacity, it can enlarge the thin film region and effectively enhance the heat transport capability, resulting in a smaller temperature drop in the evaporator for the same heat load. The concept of the minimum thermal resistance limitation in the design of heat pipes has been put forward for the first time. With an increase in the heat load, the liquid flow thickness, δ_y, becomes smaller and the liquid film thinner and leads to a decrease in the thermal resistance of the macro liquid region. The thermal resistance will reach its minimum as δ_y equals δ_0. As the heat load continues to increase, $\delta_y < \delta_0$ or $\delta_y = 0$, the liquid region will separate into two triangular liquid regions and the thermal resistance will increase sharply.

CHAPTER 3 THERMAL ANALYSIS EXPERIMENTAL INVESTIGATION OF MINIATURE FLAT AND LOOP HEAT PIPES WITH THIN FILM EVAPORATING HEAT TRANSFER ON A CURVED SURFACE

3.1 Physical Model of a Flat Heat Pipe (FHP)

The physical model of the thin film evaporation on curved surfaces in a miniature flat heat pipe is illustrated in Figs. 3-1 and 3-2. The heat pipe consists of several sub-parallel heat pipes and each pipe includes three parts: a condenser, adiabatic section and evaporator. As the heat transfer rate increases, the total pressure drop occurring in the heat pipe will increase, which directly results in the decrease of the meniscus radius in the evaporator to increase the capillary pressure and overcome the pressure drop. When the meniscus radius of liquid vapor interface in the evaporator decreases, the liquid level in the evaporator (shown in Figs. 3-1 and 3-2) will change with the heat transfer rate added on the evaporator. The liquid film thickness characterized by δ_f, shown in Fig. 3-1, will decrease as the heat transfer rate increases until it reaches the non-evaporation film thickness, shown in Fig. 3-2, where it creates the longest thin-film-evaporation region (Case II). If the heat transfer rate continuously increases, the thin film region will break into two regions (Case III), shown in Fig. 3-2, and the total length of the thin film region will become shorter. As a result, the temperature difference across the evaporating film region will increase at the same heat transfer rate. Although the heat pipe has not reached the capillary limit, the temperature drop

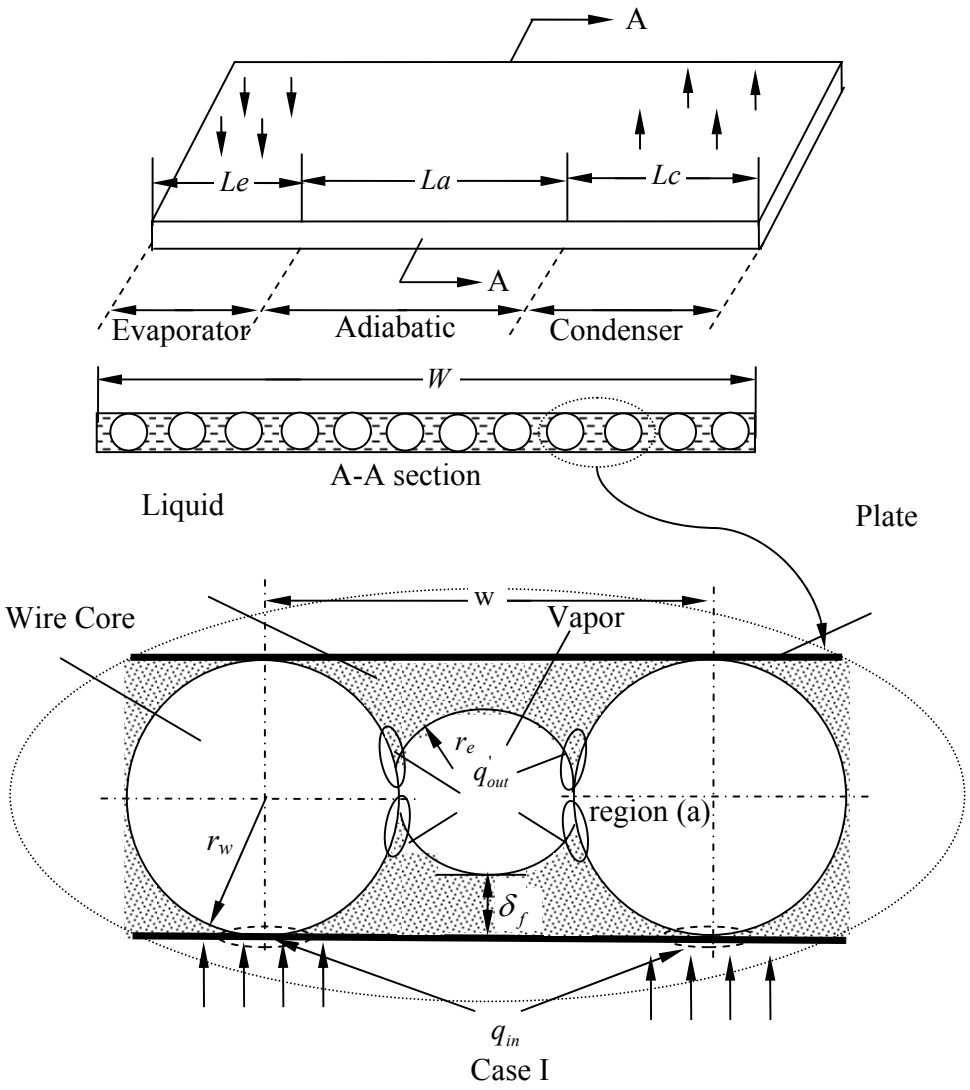

Fig.3-1 Schematic of evaporation heat transfer on curved surfaces in a flat heat pipe

occurring in the evaporator will increase, which directly reduces the effective thermal conductivity of the whole heat pipe. Because the highest effective thermal conductivity is of the greatest concern for a highly efficient heat pipe cooling device, the current investigation will focus on the temperature drop from the evaporator to the condenser, *i.e*., the effectively thermal conductivity of the whole heat pipe. Because the liquid distribution in the heat pipe

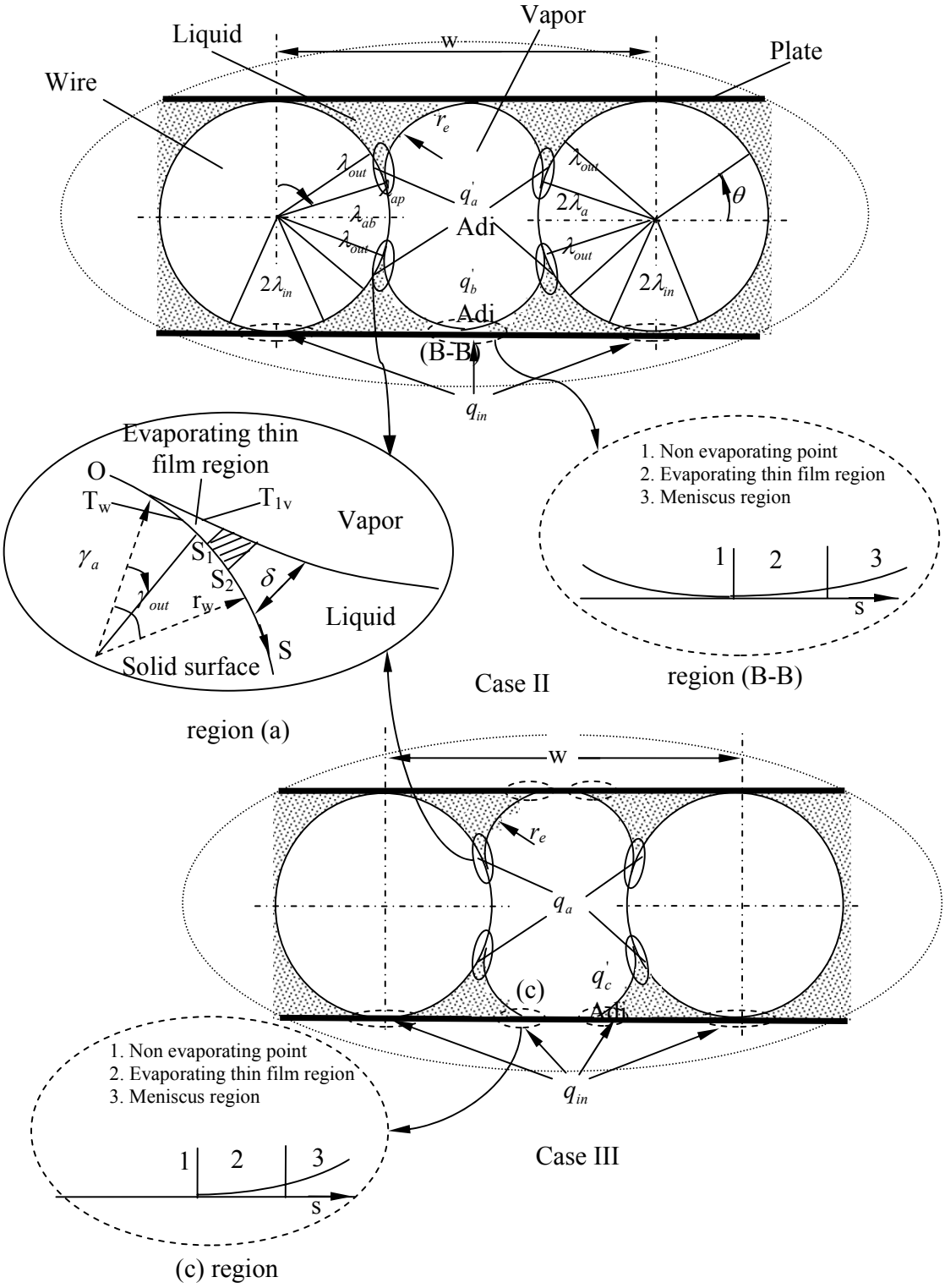

Fig.3-2 Thin film regions in the evaporator of FHP with wired wicks

including the liquid level in the evaporator is governed by the capillary limitation, the following analysis will start with the capillary flow. Once the meniscus radius distribution in the heat pipe is determined for a given heat transfer rate, the detailed liquid distributions in the evaporator and condenser can be calculated, and the temperature drop found. In order to simplify the problem and study evaporation and fluid flow in the thin film region formed on a curved surface, the following assumptions for the physical model shown in Figs. 3-1 and 3-2 are made:

1) When the wires and plates are sintered together, a finite area is formed and this area is defined as the sintered region, where the uniform heat flux input is assumed.
2) Only three cases: CASE I, CASE II and CASE III occur in the evaporator and they depend on the heat transfer load added.
3) The evaporation heat transfer only occurs in the thin film region in the evaporator and heat load passing through the bulk region is negligible. There is only the thin film condensation occurred in the condenser.
4) For CASE I, the heat load added on the external evaporator wall only can passes through the sintered region into the wire core, then reaches the thin film zones formed on the curved surface because the heat load through the bulk region on the internal plate wall into vapor phase can be neglected. In order to investigate the characteristics of evaporation heat transfer on the curved surface, we should answer the following two questions at first: a) what is the temperature distribution along the curve surface? b) what is the thin film profile on the curve surface? For CASE II, when heat is added on the external evaporator wall, it will pass through both the sintered region and the

region (B-B). The heat transfer process in the sintered region is similar to the CASE I and the heat transfer characteristics occurring in region (B-B) have been conducted in Chapter 2. For CASE III as shown in Fig. 3-2, the heat transfer process is similar to the CASE II except the thin film region (c) instead of the region (B-B).

3.2 Thermal Analysis and Experimental Investigation of FHP

3.2.1 Capillary Limitation

As shown in Fig. 3-1, the flat heat pipe consists of several sub-parallel heat pipes and each pipe includes three parts: a condenser, adiabatic section and evaporator. The micro/miniature heat pipe is governed by the capillary limit for virtually all conceivable situations. Therefore, the following analyses will focus on the capillary limit which depicts that the sum of pressure drop occurring in the flow path shall not surpass the maximum capillary pressure head so that the fluid flow can be pumped back from the condenser to evaporator. The basic relationship can be expressed as:

$$P_c \geq \Delta P_l + \Delta P_v + P_g \tag{3-1}$$

To simplify the calculation, the average radii at the evaporator and condenser are used, and thus, the capillary pumping pressure can be predicted by the Laplace-Young equation. The pressure drop occurring in the liquid and vapor phases can be calculated by momentum equations at a steady state. As shown in Figs.3-1 and 3-2, for the flat heat pipe with wired wick structure, Eq. (3-1) can be rewritten as:

$$\sigma\left(\frac{1}{\bar{r}_e}-\frac{1}{\bar{r}_c}\right)=\left[\frac{4f_l Re_l \mu_l}{2D_{h,l}^2}\cdot\frac{1}{N}\frac{Q_{tot}}{\rho_l A A_{ac} h_{fg}}+\left(\frac{f_v Re_{h,v}\mu_v}{2r_{h,v}^2}\right)\cdot\frac{1}{N}\frac{Q_{tot}}{AA_v\rho_v h_{fg}}-\rho_l g\sin\phi\right]L_{eff} \tag{3-2}$$

where,

$$
\begin{aligned}
&2\beta = \frac{\pi}{2} - \lambda_{ai}, \quad 0 < \lambda_{ai} \le \pi/2, i = B \text{ or } T \\
&N = W/w \\
&\bar{r}_e = \frac{\sin^2\beta}{\cos\beta\cos(0.5\beta+\alpha)} r_w \\
&\delta_f = \begin{cases} r_w - \left[\left(r_w + \bar{r}_e\right)\sin\lambda_{ai} + \bar{r}_e\right] & \text{for Case I} \\ \delta_0 \quad \text{for Case II} \end{cases} \\
&L_{eff} = \frac{L_e}{2} + L_a + \frac{L_c}{2} \\
&AA_{ac} = 2\left[\frac{wr_w}{2}\left(1-\sin\lambda_{ai}\right) - r_w^2\left(\beta - \frac{1}{2}\sin\lambda_{ai}\sin 2\beta\right) - r_e^2\left(\frac{\pi}{2} - \beta + \frac{1}{2}\sin\lambda_{ai}\cos\lambda_{ai}\right)\right] \\
&D_{h,l} = 4AA_{ac}/\left[2r_w tg\beta + 2r_w\beta + r_e\left(2\alpha+\beta\right)\right] \\
&r_{h,v} = 2AA_v/P_e \\
&AA_v = 2r_w w - \pi r_w^2 - AA_{ac} \\
&P_e = 2w + 2\pi r_w + 4r_e\left(2\alpha+\beta\right) - 8r_w tg\beta - 8r_w\sin\beta
\end{aligned}
\tag{3-3}
$$

Considering Eqs. (3-2) and (3-3) and Figs. 3-1 and 3-2, it can be found that β depends on λ_{ai}, and λ_{ai} is determined by the heat input. For the liquid flow, the Poiseuille number in an open groove $f_l \mathrm{Re}_l$ can be calculated by [26]:

$$
f_l Re = 14.11\alpha^{0.06009} \times \exp\left\{-0.5 \times \left[\left(\log\frac{CC}{22.22\alpha^{-0.3366}}\right)\Big/\left(2.083\alpha^{0.0372}\right)\right]^2\right\} \tag{3-4}
$$

where, $CC = r_w \cos\lambda_{ai} \big/ 4r_c \cos\alpha$. Vapor can be considered as ideal gas. As shown in Fig. 3-1, the vapor flow channel in the condenser and adiabatic section can be approximated as a round tube, and its Poiseuille number is equal to 16 for a laminar flow. For the evaporator section, the vapor flow path can be approximated as rectangular channel, which $\frac{b}{a} = \frac{\pi r}{w} = 0.785$ and its Poiseuille number is equal to 14.5. Once Eqs. (3-2) and (3-3) are solved for a given heat transfer rate, the liquid distribution along the heat pipe can be calculated and the meniscus radius and liquid level in the evaporator and condenser can be determined.

3.2.2 Heat Transfer in the Evaporator

In order to find the temperature drop occurring in the evaporator, the heat transfer process must be determined. When heat is added to the evaporator, some of the heat will transfer through the solid wire to the working fluid, and the rest of the heat directly through the heat pipe shell to the working fluid. While the temperature of the heat pipe shell can be assumed to be constant, the temperature distribution on the solid wire must be determined at first.

3.2.2.1 Temperature distribution in the wire core

Thin film evaporation heat transfer plays an important role in the phase change heat transfer on a flat surface [9, 11, 27]. Stephan and Busse [28] found that the effects of interface temperature variation on the heat transfer in the thin film evaporation region cannot be neglected. In order to investigate the heat transfer characteristics including the interface

temperature effect on the thin film profiles, evaporation heat transfer on the curved surface, as shown in Fig. 3-1, the temperature distribution in the wire core should be determined at first. Since the length of the wire is much longer than its radius, the temperature distribution in the wire core can be predicted by a 2-D model. The governing equation can be expressed as:

$$\frac{\partial^2 T}{\partial r^2}+\frac{1}{r}\frac{\partial T}{\partial r}+\frac{1}{r^2}\frac{\partial^2 T}{\partial \theta^2}=0 \tag{3-5}$$

The required boundary conditions can be expressed as,

$$-k_w\frac{dT}{dr}\Big|_{r=r_w}=q_{in}^{'} \qquad at \quad \frac{3\pi}{2}-\gamma_{in}\le\theta\le\frac{3\pi}{2}+\gamma_{in} \tag{3-6}$$

$$-k_w\frac{dT}{dr}\Big|_{r=r_w}=\begin{cases}0 & at \quad -\lambda_{ab}\le\theta\le\lambda_{at}\\ q_{out}^{'} & at \quad \lambda_{aT}\le\theta\le\lambda_{aT}+\lambda_{out},-(\lambda_{aB}+\lambda_{out})\le\theta\le-\lambda_{aB}\\ q_{out,b}^{'} & at \quad \lambda_{aT}+\lambda_{out}\le\theta\le\pi/2,\ \frac{3\pi}{2}+\lambda_{in}\le\theta\le2\pi-(\lambda_{aB}+\lambda_{out})\end{cases} \tag{3-7}$$

Equation (3-5) can be solved using the separation of variables. And, the temperature distribution of the wire core can be expressed by

$$T_w(r,\theta)=a_0+\sum_{n=1}^{\infty}\left\{\left(\frac{r}{r_w}\right)^n\left[a_n\cos(n\theta)+b_n\sin(n\theta)\right]\right\} \tag{3-8}$$

where,

$$a_n=\frac{2r_w}{n\pi}\left(\begin{array}{l}\int_{\lambda_{aT}}^{\lambda_{aT}+\lambda_{out}}q_{out,a}^{'}\cos(n\theta)d\theta+\int_{\lambda_{aT}+\lambda_{out}}^{\pi/2}q_{out,b}^{'}\cos(n\theta)d\theta\\ +\int_{\frac{3\pi}{2}+\lambda_{in}}^{2\pi-\lambda_{aB}-\lambda_{out}}q_{out,b}^{'}\cos(n\theta)d\theta+\int_{2\pi-\lambda_{aB}-\lambda_{out}}^{2\pi-\lambda_{aB}}q_{out,a}^{'}\cos(n\theta)d\theta+\int_{\frac{3\pi}{2}}^{\frac{3\pi}{2}+\lambda_{in}}q_{in}^{'}\cos(n\theta)d\theta\end{array}\right) \tag{3-9}$$

$$b_n = \frac{2r_w}{n\pi}\left(\begin{array}{l}\int_{\lambda_{aT}}^{\lambda_{aT}+\lambda_{out}} q'_{out,a}\sin(n\theta)d\theta + \int_{\lambda_{aT}+\lambda_{out}}^{\pi/2} q'_{out,b}\sin(n\theta)d\theta \\ +\int_{\frac{3\pi}{2}}^{\frac{3\pi}{2}+\lambda_{in}} q'_{in}\sin(n\theta)d\theta + \int_{\frac{3\pi}{2}+\lambda_{in}}^{2\pi-\lambda_{aB}-\lambda_{out}} q'_{out,b}\sin(n\theta)d\theta + \int_{2\pi-\lambda_{aB}-\lambda_{out}}^{2\pi-\lambda_{aB}} q'_{out,a}\sin(n\theta)d\theta\end{array}\right) \quad (3\text{-}10)$$

and a_0 can be calculated by $a_0 = T_{sat} + \text{superheat}$.

3.2.2.2 Evaporating Thin Film Profiles on the Wire Core Surface

When the heat transfer rate in the heat pipe changes, the liquid distribution in the liquid channel will be different. The meniscus radius in the evaporator will be different depending on the heat transfer rate. Based on the configuration of thin film region, there exist three cases as shown in Figs. 3-1 and 3-2. For the Case I ($\delta_f > \delta_0$), the liquid thickness δ_f decreases when the heat load increases and the thin film region evaporation only occurs in the region (a). The fluid flow in the region (a) is driven by the curvature variation and disjoining pressure to overcome the viscous pressure loss and gravity effect, The governing equation can be written as:

$$\sigma\frac{dK}{dS} + K\frac{d\sigma}{dS} - \frac{dp_d}{dS} = \frac{dp_l}{dS} + \frac{dp_{hg}}{dS} \quad (3\text{-}11)$$

For the region (a), using the coordinate transformations,

$$S = r_w\theta'',\ \theta'' = 2\pi - \lambda_a - \theta \text{ at } 2\pi - \lambda_a - \lambda_{out} \le \theta \le 2\pi - \lambda_a \quad (3\text{-}12)$$

Equation (3-11) can be rewritten as

$$\sigma\frac{dK_a}{d\theta''} + K_a\frac{d\sigma}{d\theta''} - \frac{dp_d}{d\theta''} = \frac{dp_l}{d\theta''} + \frac{dp_{hg}}{d\theta''} \quad (3\text{-}13)$$

where,

$$p_{hg} = -\rho g r_w\left(1-\sin\lambda_{at}\right) \text{ or } p_{hg} = \rho g r_w\left(1-\sin\lambda_{ab}\right) \text{ at } 0 \le \theta'' \le \lambda_{out} \quad (3\text{-}14)$$

$$K_a = \frac{-\frac{d^2\delta}{d\theta''^2}(\delta + r_w) + 2\left(\frac{d\delta}{d\theta''}\right)^2 + (\delta + r_w)^2}{\left[\left(\frac{d\delta}{d\theta''}\right)^2 + (\delta + r_w)^2\right]^{3/2}} \tag{3-15}$$

$$\text{and } \frac{dp_l}{d\theta''} = -\frac{\mu_l \dot{m}_\delta}{\rho_l\left[\frac{3}{2}\delta^2 + r_w\delta + (r_w + \delta)^2 \ln\left(\frac{r_w}{r_w + \delta}\right)\right]} \tag{3-16}$$

Boundary conditions can be summarized as

$$\delta\Big|_{\theta''=0} = \delta_0,\ K\Big|_{\theta''=0} = K_0 = \frac{1}{r_w + \delta_0},\quad \frac{d\delta}{d\theta''}\Big|_{\theta''=0} = 0 \tag{3-17}$$

where, $p_d = -\frac{A}{\delta^3}$, $A = 10^{-19}$ J, and $\delta_0 = \left[AT_v \Big/ (T_w - T_v)\rho_v h_{fg}\right]^{1/3}$. Then, the film thickness distribution can be calculated by Eqs. (13-16) with the boundary condition of Eq. (3-17).

As the heat load increases, δ_f decreases. And when δ_f decreases and becomes equal to δ_0, a new thin film evaporation region forms along the flat surface. This case is called Case II and there exists hybrid thin film evaporation regions which consist of regions (a) and (b). The governing equation of the thin film thickness distribution in region (b) can be expressed as Eq. (3-11) without the $\frac{dp_{hg}}{dS}$ term, and the terms of curvature and $\frac{dp_l}{dS}$ can be rewritten as:

$$\frac{dp_l}{dS} = -\frac{f_l \mathrm{Re}_{l,\delta}\,\mu_l \int_0^s \frac{q(s)}{h_{fg}} ds}{2\delta^3(s)\rho_l} \tag{3-18}$$

$$K_b = \frac{\dfrac{d^2\delta}{ds^2}}{\left[1+\left(\dfrac{d\delta}{ds}\right)^2\right]^{3/2}} \tag{3-19}$$

respectively. The boundary conditions can be rewritten as

$$K = 0, \quad \delta = \delta_0, \quad \frac{d\delta}{dS} = 0 \qquad \text{at } S = 0 \tag{3-20}$$

As shown in Fig.3-2, the contact angle can be considered as zero in the thin film region (b) in Case II. With the further increase of the heat load, the thin film evaporation region (b) breaks into two zones where the contact angle is not equal to zero, which is called Case III. Once the liquid film distribution reaches Case III, the effective thermal conductivity of the heat pipe decreases although the heat pipe has not reached the capillary limit. Therefore, the heat transfer rate corresponding to Case II is considered as the design-point "maximum" heat transport of FHP. Because this "maximum" heat transport occurring in Case II can result in the highest effective thermal conductivity of the heat pipe, which is of the most concern, the heat transfer characteristics in Case III will not be discussed here.

3.2.2.3 Maximum Heat Transport Capacity in the Evaporator

Thin-film-evaporation heat transfer can be considered as one-dimensional heat conduction since the thickness of this region is very thin. Therefore, the local heat flux can be calculated by $q^{'} = k_l \dfrac{\Delta T}{\delta}$, which depends on the thin film profile and temperature difference between

the wall temperature and interface temperature. For the Case I, heat transfer through the evaporating thin film only exists in the region (a), and the local heat flux can be expressed as:

$$q_a^{'} = k_l \frac{T_w\left(r_w,\theta\right) - T_{\delta a,v}\left(\theta\right)}{\delta\left(\theta\right)} \tag{3-21}$$

where $T_w\left(r_w,\theta\right)$ can be predicted by Eq. (3-8) and $\delta\left(\theta\right)$ can be found by Eqs. (3-11) and (3-13).

For the Case II, the thin-film-evaporation heat transfer occurs in both the regions (a) and (B-B), and the heat flux in region (a) can be calculated with the same way as the CASE I and the heat flux in region (B-B) can be predicted by

$$q_b^{'} = k_l \frac{T_w - T_{\delta b,v}}{\delta\left(s\right)} \tag{3-22}$$

where T_w is the local wall temperature, and $\delta\left(s\right)$ can be calculated by Eq. (3-11) without $\frac{dp_g}{dS}$ term and with boundary conditions shown in Eqs. (3-18) and (3-19).

The local interfacial temperatures at the liquid-vapor interface on thin film regions, $T_{\delta a,v}\left(\theta\right)$ and $T_{\delta b,v}$ can be depicted by the Clausius-Clapeyron equation,

$$\left(\frac{dp}{dT}\right)_{sat} = \frac{h_{fg}}{T_{sat}\left[\left(1/\rho_v\right) - \left(1/\rho_l\right)\right]} \tag{3-23}$$

Integrating Eq. (3-23) from T_{sat} to the interface temperature $T_{\delta,v}$ yields

$$T_{\delta,v} = T_v\left[1+\left(\Delta p \Big/ \rho_v h_{fg}\right)\right] \tag{3-24}$$

where $\Delta p = k_t\sigma + p_d$, $p_d = -A/\delta^3$.

Although the heat transport capability for the Case II has not reached the capillary limit, the thermal resistance from the evaporator to the condenser for the Case II is the lowest. Therefore, it is defined that the heat transfer rate at the Case II is the maximum heat transport capacity. For the Case II as shown in Fig. 3-2, the maximum heat transport capacity consists of heat transfer through bulk liquid (macro liquid region) and evaporating heat transfer through thin film regions (a) and (B-B). In this case, the heat transfer rate that passes through bulk liquid can be neglected. For thin film region (a), heat transfer through this region can be calculated by:

$$q = \int_0^{\lambda_{out}} q_a^{'} dA^{"} = L_e r_w \int_0^{\lambda_{out}} k_l \frac{T_w\left(r_w,\theta^{"}\right) - T_{\delta,v}\left(\theta^{"}\right)}{\delta\left(\theta^{"}\right)} d\theta^{"} \tag{3-25}$$

where, $\theta_1^{"} = \theta - \lambda_a$ at $\lambda_a \le \theta \le \lambda_a + \lambda_{out}$, and $\theta_2^{"} = 2\pi - \lambda_a - \theta$ at $2\pi - \lambda_a - \lambda_{out} \le \theta \le 2\pi - \lambda_a$, respectively. The total heat transport through thin film region (a) on a given wire core can be calculated by:

$$q_a = 2L_e r_w \left(\int_{\lambda_a}^{\lambda_a+\lambda_{out}} k_l \frac{T_w\left(r_w,\theta\right) - T_{\delta a,v}\left(\theta\right)}{\delta\left(\theta\right)} d\theta + \int_{2\pi-\lambda_a}^{2\pi-\lambda_a-\lambda_{out}} k_l \frac{T_w\left(r_w,\theta\right) - T_{\delta a,v}\left(\theta\right)}{\delta\left(\theta\right)} d\theta \right) \tag{3-26}$$

In the same way, the heat transfer rate through thin film region (B-B) can be found by

$$q_b = 2L_e \int_0^s k_l \frac{T_w - T_{\delta b,e}}{\delta\left(s\right)} ds \tag{3-27}$$

Combining Eqs. (3-26) with (3-27) and considering the evaporator structure shown in Fig.3-1, the maximum heat transport capacity for the FHP can be expressed as:

$$Q_{total} = \frac{W}{w}\left(q_a + q_b\right) \tag{3-28}$$

3.2.3 Thin Film Condensation Heat Transfer in the Condenser

When the condensation heat transfer occurs in the condenser, the latent heat of vapor is released. As shown in Fig.3-3, the condensation process can be simply modeled as the film condensation on a surface. The velocity of vapor flow decreases along the condenser direction to zero at the cap end. Its inlet Reynolds number can be calculated by:

$$Re_{v,i} = \frac{\rho_v u_{v,i} D_h}{\mu_v} \tag{3-29}$$

where, $D_h = {4A_e}/{P_e}$, $A_e = 2r_w w - \pi r_w^2 - A_{ac}$, and $u_{v,i}$ is the inlet velocity of vapor flow in the condenser and can be expressed by

$$u_{v,i} = \frac{Q_{total}}{NA_e \rho h_{fg}} \tag{3-30}$$

Thus, the average heat transfer coefficient in the condenser can be calculated by

$$\overline{h_D} = C\left[\frac{g\rho_l\left(\rho_l - \rho_v\right)k_l^3 h_{fg}^{'}}{\mu_l\left(T_{sat} - T_{wc}\right)D_h}\right]^{1/4} \tag{3-31}$$

where, $h_{fg}^{'} = h_{fg} + \frac{3}{8}c_{p,l}\left(T_{sat} - T_{cw}\right)$. Since the inlet velocity of vapor flow is not very high ($\mathrm{Re}_{v,i} < 3500$),Chato [29] recommended the constant C is equal to 0.555. Based on the condenser geometry as shown in Fig. 3-1, using the heat transfer coefficient shown in Eq. (3-

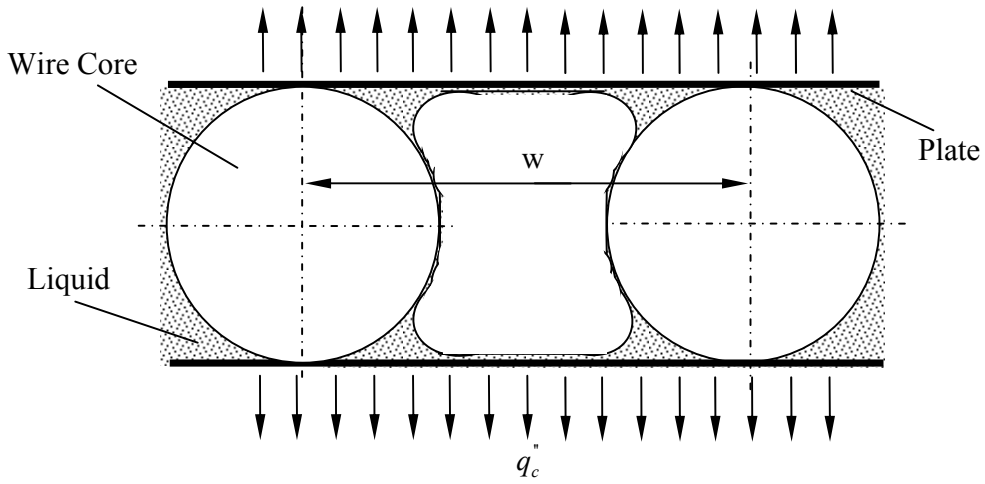

Figure 3-3 Schematic of thin film condensation heat transfer in condenser

31), the correlation between the heat load and condensation temperature difference can be expressed by:

$$Q_{total} = 0.9334 \frac{W}{w} \left[\frac{g\rho_l (\rho_l - \rho_v) k_l^3 h_{fg}^{'}}{\mu_l (2w - \pi r_w) r_w} \right]^{1/4} (w + \pi r_w)^{5/4} L_c \Delta T^{3/4} \qquad (3\text{-}32)$$

3.2.4 Experimental System and Investigations

Figure 3-4 illustrates the experimental system which consists of the test section (flat heat pipe), data acquisition system, heater power supply system, and cooling system. The data acquisition system includes a PC, thermocouples, and a data acquisition card to measure the temperature responses of evaporator and condenser, and power inputs. The cooling system contains two flat aluminum cooling blocks and one cooling bath where the temperature was maintained at $60 \pm 0.1^0 C$. The maximum heat load of the heater power supply is 250 W. In order to supply a uniform heat flux, the top surface size of the heater was fabricated as the

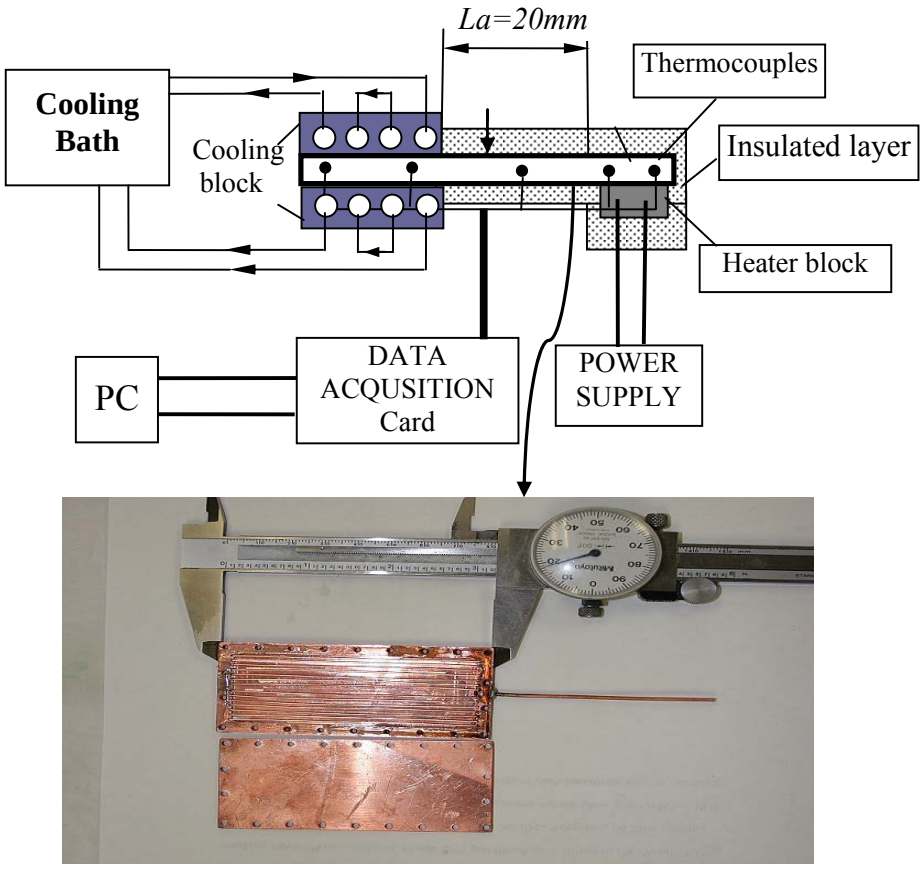

Fig. 3-4 Schematic of the experimental system

same as the evaporator bottom surface, which was 15 mm width and 30 mm length. The largest measurement uncertainties of the current investigations were less than 1%. The test section is a FHP which consists of 15 sub-parallel heat pipes and each of these heat pipes consists of the condenser ($L_e = 15mm$), adiabatic section ($L_a = 20mm$), and evaporator ($L_c = 40mm$). As shown in Fig. 1, the wire diameter is equal to 1 mm (r_w=0.5 mm) and the distance between two wires is 2.0 mm (w=2.0 mm). The width and length of the FHP are 30 mm and 75 mm, respectively. The total amount of water charged to the FHP is 0.6g. In order to reduce the contact thermal resistance, the Omega "201" thermal paste was used between the aluminum cooling block and the condensing surface in the condenser, and between the heater and the evaporating surface in the evaporator.

3.2.5 Results and Discussion

From the above analysis, heat transfer through thin films formed on the curved surface can be predicted by the third-order differential equations, which can be solved by the forth-order Runge-Kutta method to obtain the interface temperature and film thickness distribution. It should be noted that the following assumptions are made in the calculation:

1) Previous results [15, 17, 18, 22, 31] indicate that most of the heat added on the solid wire will transfer through the thin film region. So it is assumed that the heat added on the particle is equal to the total evaporating heat transfer through the thin film region.

2) The vapor flow is saturated and considered as ideal gas.

3) The meniscus radius of liquid-vapor interface in the wicks is constant at a given heat load.

4) When the film thickness increases, the disjoining pressure effect decreases until it is so small that it can be neglected. The length of the thin film region is determined by the cut-off value of 0.015 Pa of disjoining pressure.

5) Water is used as the working fluid and its thermophysical properties at 60^0C are used for the numerical calculations.

6) As shown in Fig.1, the contribution of the heat transfer through region (b) in Case I is negligible since the thermal resistance is very large due to the thick liquid film. But as the heat load increase, the liquid thickness becomes thinner and thinner, the contribution of the heat transfer through the region (b) should be considered. In the evaporation heat transfer calculation, the heat pass through the region (b) has been added when the film thickness $\delta_f = 0.05mm$ until δ_f reaches δ_0. If the heat load continues to increase after δ_f reaches δ_0, the Case III situation is used to predict the temperature response in the evaporator.

7) Only film condensation heat transfer occurs in the condenser. Heat flux through the thin film region depends on the input heat load and the temperature distribution on the solid wire, which in turn determines the evaporating heat transfer and the viscous fluid flow in the thin film region. Therefore, an iterative technique has been utilized to solve for the temperature distribution on the solid wire, liquid film profile, interface temperature, and heat flux in the thin film region. The calculation procedure for the evaporation heat transfer at a given heat load can be summarized as follows:

1) Select a contact angle of α.

2) Solve Eqs. (3-2) and (3-3) for $\overline{r_e}$, λ, and δ_f.

3) Select a superheat.

4) Calculate the temperature distribution of the solid wire by Eq. (3-8).

5) Calculate the thin film profile by Eqs.(3-13)-(3-20).

6) Calculate the vapor-liquid interfacial temperature and heat flux distribution by Eqs (3-21)-(3-24).

7) Calculate the total heat load and compare the prediction with the given heat load. If the error is greater than 0.5W, then go to step 3.

8) When the error between the prediction and the given heat load is less than 0.5W, output the superheat, thin film profiles and heat flux distributions.

Figure 3-5 (a) illustrates the heat load effect on the average radius in the evaporator at different contact angles in one sub-parallel heat pipe. The net capillary pressure difference pumping the condensate back to evaporator can be calculated by the Laplace-Young equation: $\Delta P_c = \sigma\left(\frac{1}{r_e} - \frac{1}{r_c}\right)$. Solving Eqs. (3-2) and (3-3) for a given heat load, the average curvature radius of evaporator $\bar{r}_e$ can be determined and it is found that it depends on the contact angle, heat load, and dimensions of wick structures. As the heat load increases, the flow rates in both the liquid and vapor phases result in the increase of the total pressure drop. In order to maintain a steady state operation of the heat pipe, higher capillary pressure difference between the evaporator and condenser results in. Therefore, the average meniscus radius in the evaporator decreases as the heat load increases, as shown in Fig. 3-5(a), and it depends on the contact angle. Figure 3-5(b) illustrates the heat transfer rate effect on the angle, λ, which stands for the liquid thickness in the evaporator in one sub-parallel heat pipe. The angle λ

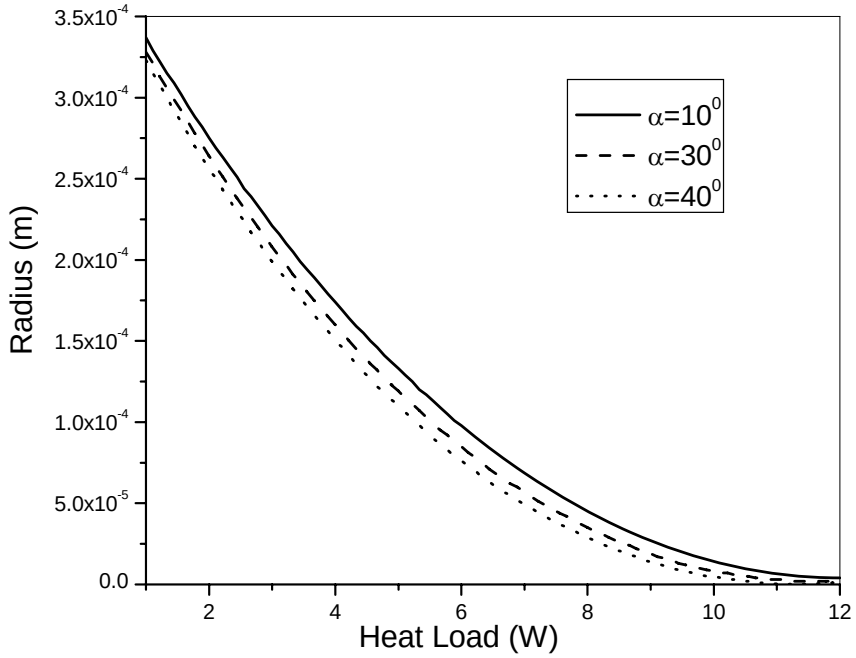

(a)

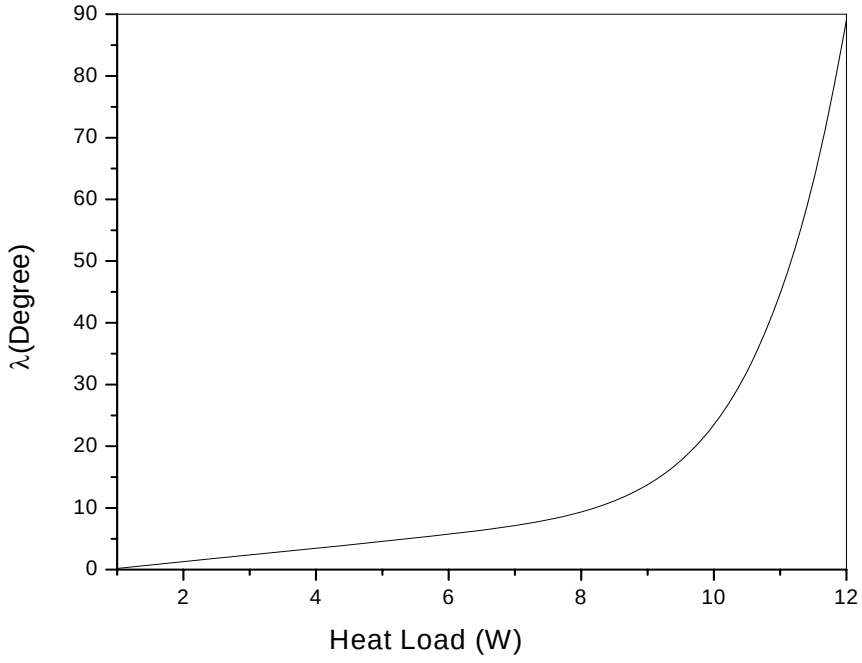

(b)

Figure 3-5 Heat load effects on (a) average radius of evaporator at different contact angles, (b) λ at $\alpha = 30^0$

changes slowly when the heat load is low. As the heat load becomes higher than 9W, however, the angle varies dramatically with the heat load.

Figures 3-6(a), (b), and (c) illustrate the thin film thickness profiles of the Case I ($\alpha = 30^{\circ}$, only for the curved surface), Case II ($\alpha = 30^{\circ}$, for the curved surface and $\alpha = 0^{\circ}$, for the flat surface), and Case III($\alpha = 30^{\circ}$, for both the curved and flat surface) at a superheat of 1.0 K, respectively. As shown in Fig. 3-6, the thin film region in Case I yields the lowest heat transport capability because it has the thin film evaporation region only on the curved surface. Case II yields the highest because of the curved surface and flat surface with a contact angle equal to zero. As shown in Fig. 3-6(c), the film thickness distributions of Region (a_B) and Region (a_T) illustrate the gravity effect on the thin film distribution on the curved surface. Results shown in Figures 3-6 (b) and (c) indicate that the gravity directly affects the length of the thin film region. In addition, the length of the thin film regions on the flat surface is much longer than that of thin film region on the curved surface.

When the interface temperature of vapor-liquid is equal to the wall temperature, no evaporation heat transfer occurs in this region. The non-evaporation thin film thickness can be determined by Eq. (3-24). If $T_{\delta,v} = T_w$ and $\frac{d\delta}{d\theta^{"}}\Big|_{\theta^{"}=0} = 0 \Rightarrow k \to 0$, the non-evaporating film thickness can be found by $\delta_0 = \left[AT_v \Big/ \left(T_w - T_v\right)\rho_v h_{fg} \right]^{1/3}$. The heat flux through the thin film region calculated by a 1-D heat conduction heat transfer model. When a superheat (T_w-T_{lv}) between the solid surface and the interface temperature exists, the high heat flux takes place in the thin film evaporation region. As shown in Fig. 3-7, this superheat drastically affects the evaporation thin film profiles both in length and shape. And a larger superheat results in a

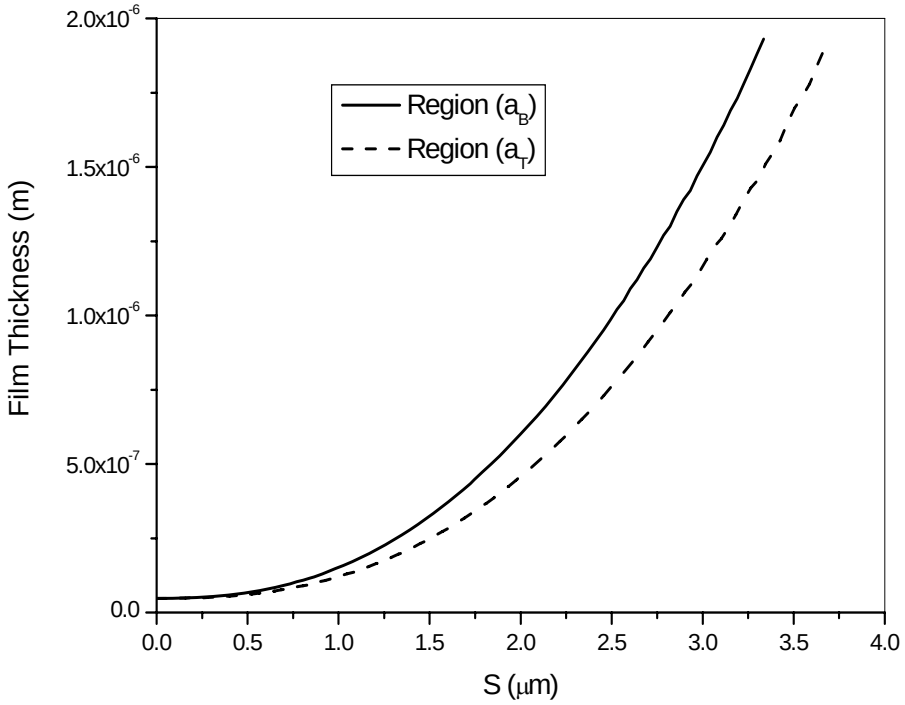
Region (a_B)
Region (a_T)
Film Thickness (m)
S (μm)
2.0x10^{-6}
1.5x10^{-6}
1.0x10^{-6}
5.0x10^{-7}
0.0
0.0
0.5
1.0
1.5
2.0
2.5
3.0
3.5
4.0

(a)

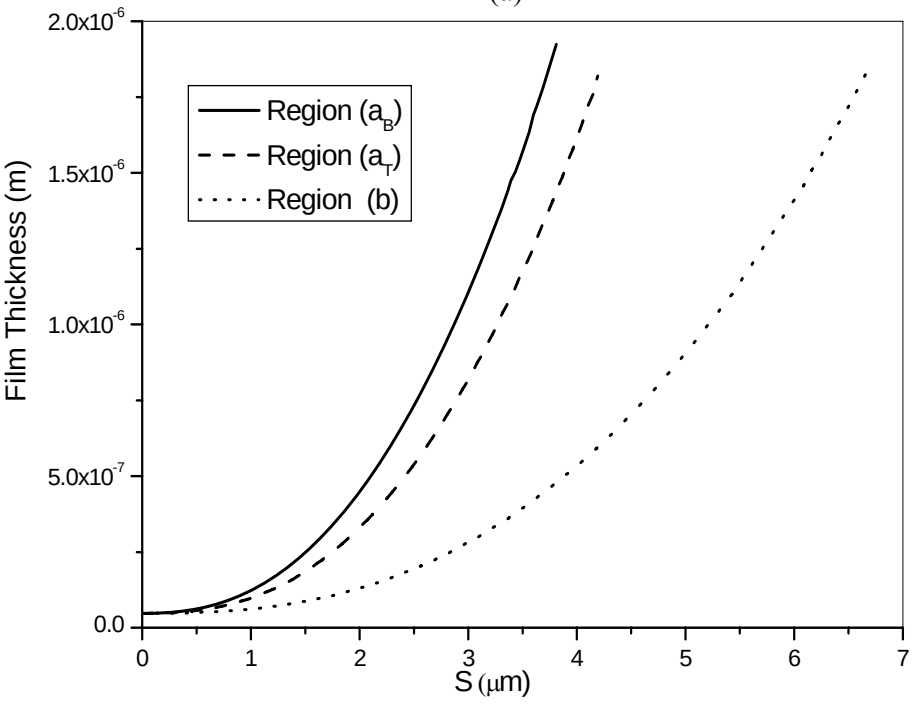
Region (a_B)
Region (a_T)
Region (b)
Film Thickness (m)
S (μm)
2.0x10^{-6}
1.5x10^{-6}
1.0x10^{-6}
5.0x10^{-7}
0.0
0
1
2
3
4
5
6
7

(b)

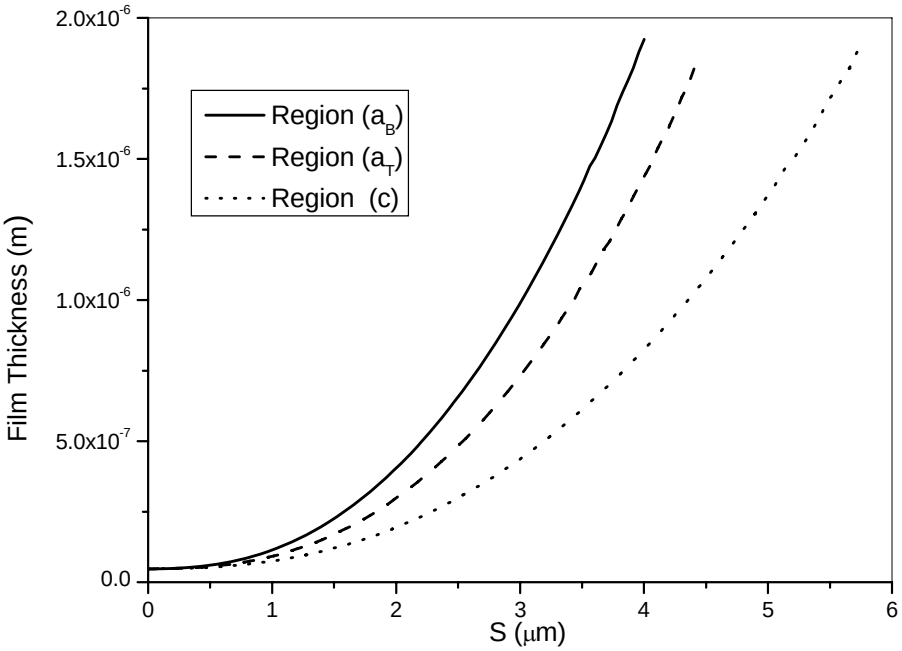

(c)

Fig.3-6 Thin film profiles at (a) case I, (b) case II, and (c) case III (T_w-T_v=1.0K)

higher heat flux and higher mass flow rate in the thin film region, which directly increases the viscous pressure drop over a given length. In order to maintain the steady-state evaporating heat transfer in the thin film region and pump enough liquid to the thin film region, the disjoining pressure must increase and overcome the viscous pressure drop and the pressure difference due to the curvature variation. As shown in Fig. 3-7(a), when the superheat increases, the thin film region decreases significantly. In other words, the curvature of thin film region is sensitive to superheat and the thickness of evaporating thin film increases dramatically with the superheat at a given location. With a higher superheat, the non-evaporating film thickness becomes thinner, and that produces an even higher heat flux in the evaporating thin film region than the case with a smaller superheat.

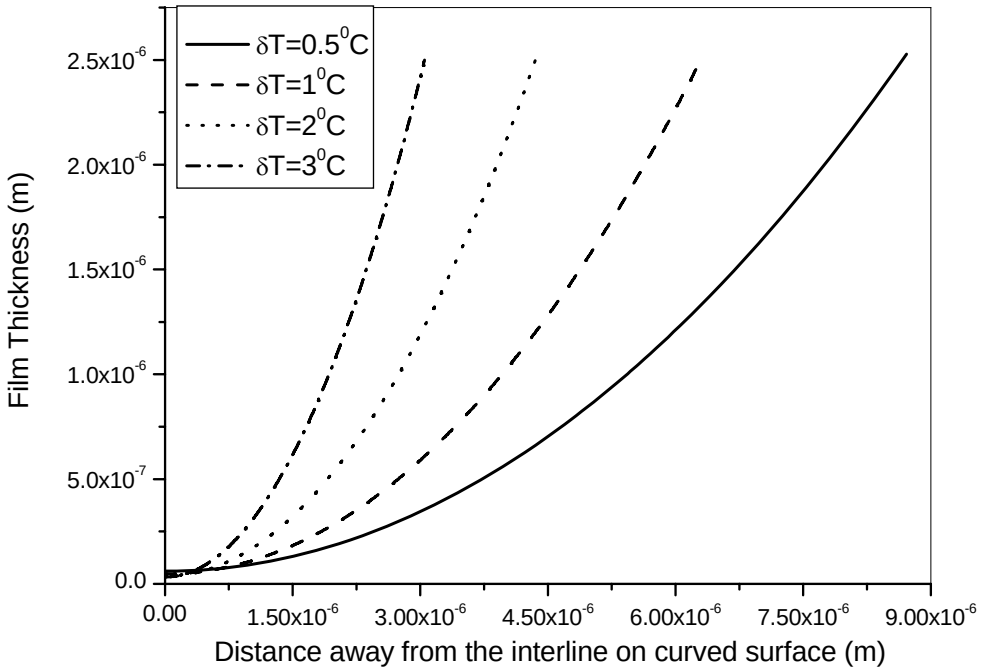

(a)

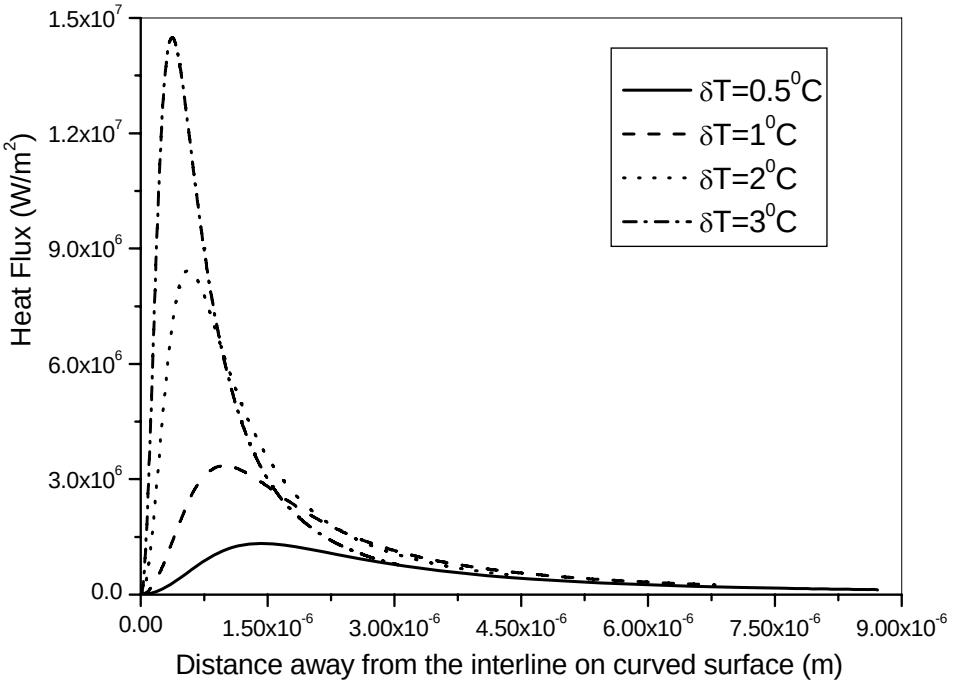

(b)

Fig.3-7 Superheat effect on the thin film profile and heat flux distribution on the upper curved surface (Case I, $\alpha = 30^0$)

At the same conditions, the effects of the gravity and contact angle on heat flux distributions along different surfaces were conducted with a superheat of 1.5 K. As shown in Fig.3-8, the heat flux profiles through the liquid films of the bottom and upper surfaces on a curved wire core in the FHP are different due to the effects of gravity on the fluid flow in the thin film region with the contact angle $\alpha = 30^0$. Obviously, the gravity force produces a longer length of thin film region and results in a better heat transfer performance on the upper

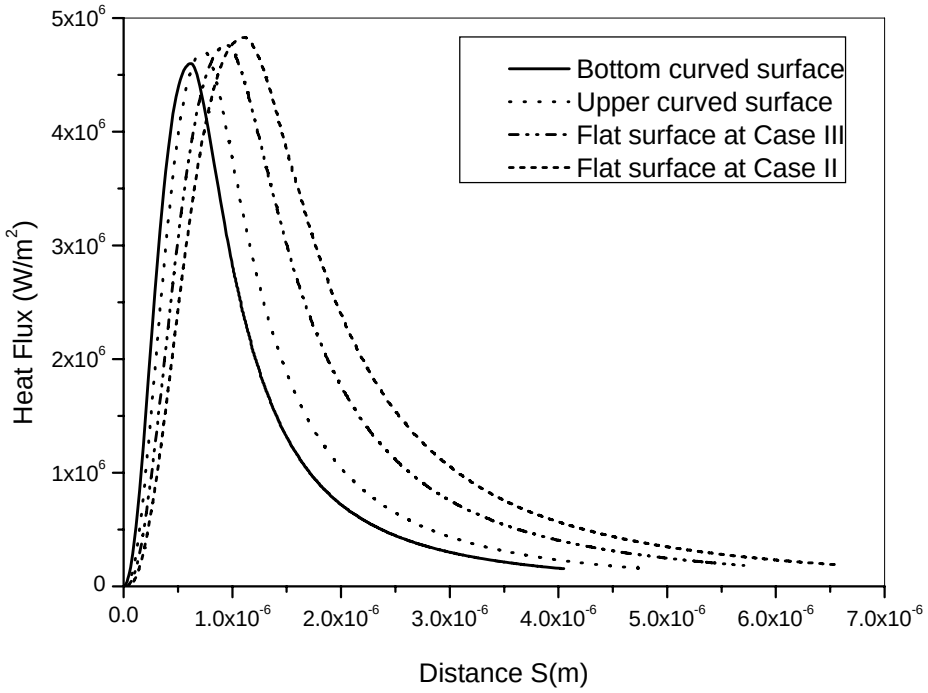

Fig.3-8 Curved surface effect on the heat flux distribution (T_w-T_v=1.5 K)

surface than that on the bottom surface. Integrating the heat flux profiles, the amount of heat through upper surface is 8.4% higher than that through the bottom surface. Clearly, the gravity directly affects the heat transfer rate through the evaporating thin film region. As shown in Fig.3-2, thin film evaporation on the flat surface will play an important role when

the heat pipe operates in Case II. When the heat load further increases after the heat pipe reaches Case II, the thin film evaporating region on the flat surface would break into two thin film zones and the heat pipe would operate in Case III. The heat flux distributions on the flat surface in Case II ($\alpha = 0^0$) and III ($\alpha = 30^0$) also have been conducted, herein, by integrating the heat flux, and the results show that the heat transport capacity of Case II is 1.11 times of that in Case III. Comparing these heat flux distributions, it can be concluded that the contact angle significantly affects the thin film profiles and heat transfer rate through the thin film regions.

Based on the model presented above, the temperature response to the heat load in the

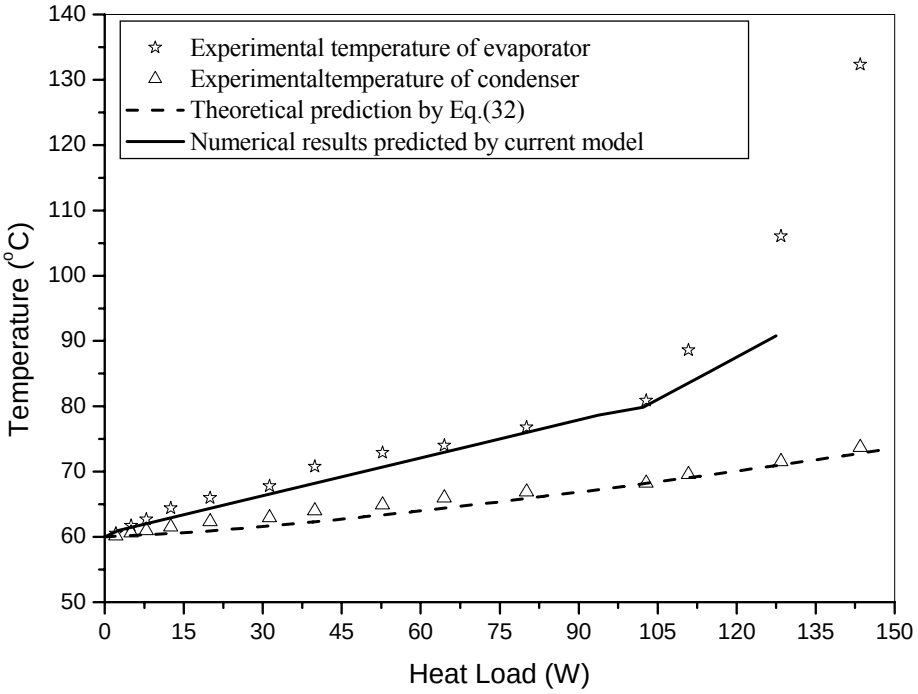

Fig.3-9 Comparison between the theoretical prediction and experimental data of the evaporator and condenser temperature response versus heat load input (working fluid: water, charged amount = 0.6g)

evaporator and condenser has been predicted. In order to verify the theoretical prediction, the experimental data of the temperature response with the heat load in the evaporator and condenser have been compared with the theoretical prediction. As shown in Fig.3-9, the theoretical results agree very well with experimental data for the condenser. The current model can be used to predict the temperature response in the evaporator with heat load if the heat load was less than 105W, which is corresponding to the situation of Case II. When the heat loads continue increasing, the thin film evaporating region on the flat surface would break into two thin film zones and the heat pipe would operate in Case III, where a contact angle of 30 degrees was selected. The increase of the contact angle would directly increase the temperature drop across the liquid film. Although the model considered this effect, the experimental results are still much higher than the theoretical prediction. The heat pipe also worked when the heat load was higher than 105W but its performance became worse as heat load increased, and it completely lost function when the heat load reached 138W.

3.3 Theoretical Analysis and Experimental Investigation of Miniature LHP

3.3.1 Physical Model of a Loop Heat Pipe

Figure 3-10 illustrates schematic of a loop heat pipe (LHP) with sintered particles in the evaporator where the thin-film-evaporation heat transfer on curved surfaces occurs. When heat is added on the evaporator wall, it will pass through the sintered particles, and reach the interface in the region II, where the thin-film-evaporation heat transfer occurs. The vapor from the liquid phase flows through the vapor line and to the condenser where the condensation heat transfer occurs and the vapor phase releases its latent heat, and condenses

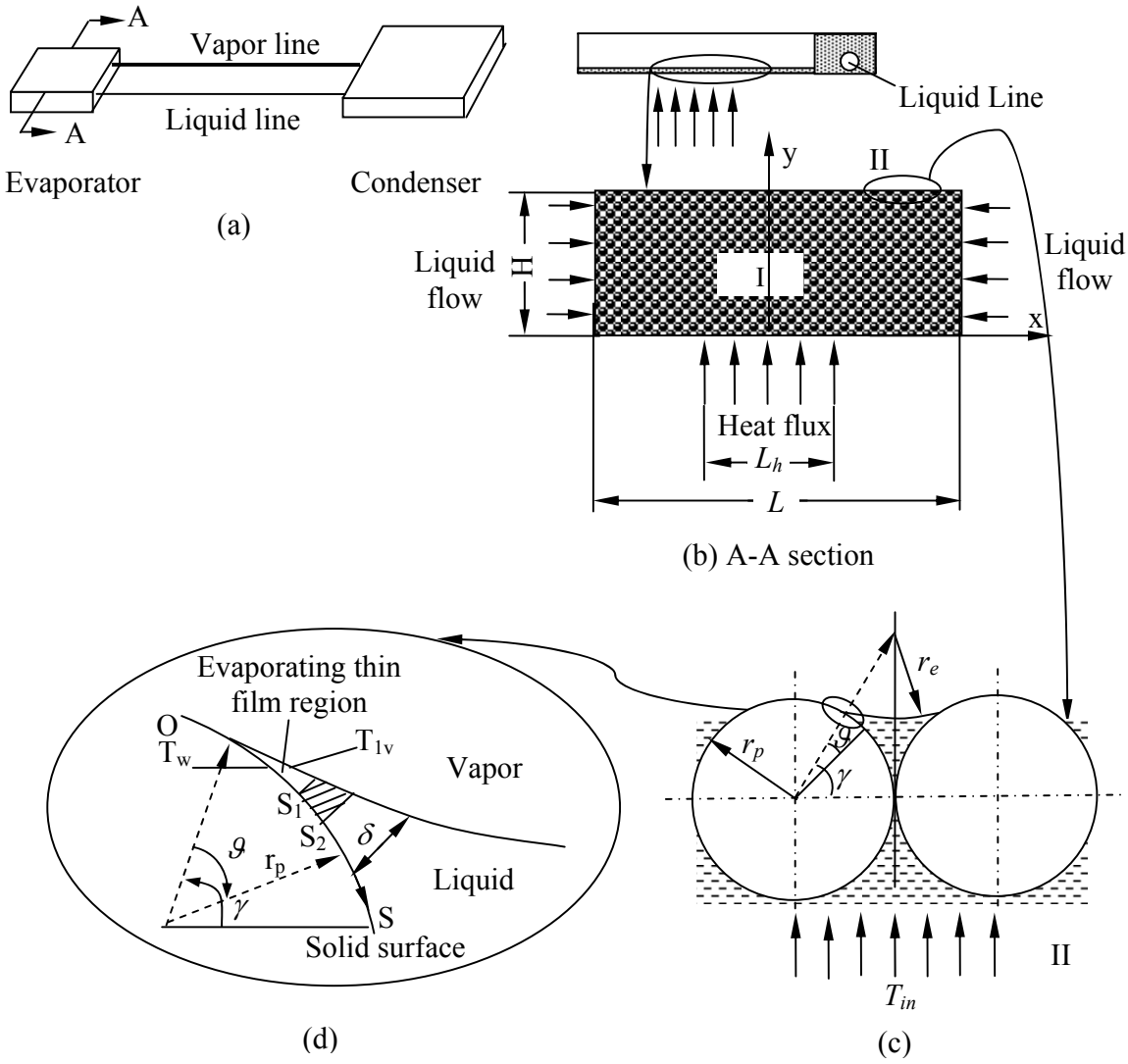

Figure 3-10 Schematic of the loop heat pipe with a sintered layer bottom evaporator

into the liquid phase. The condensate is pumped back to the evaporator via the liquid line by the capillary pressure. In this way, the heat is continuously transferred from the evaporator to the condenser. As shown in Fig.3-10(a), LHP is a heat pipe in which the vapor and liquid

flow passages are separated and no wick structures exist in both flow passages resulting in a low pressure drop. Thus, the heat transport capacity of a LHP is one or two orders of magnitude greater than that of conventional heat pipes [12, 32]. Some unique features of the LHP, such as long-distance heat transport capacity, no effect of vapor flow on liquid flow, low sensitivity to the change of orientation in 1-g conditions, and ramified evaporator & condenser design make the LHP become one of the potential candidates in the next generation of cooling devices/systems. Since the LHP normally consists of an evaporator, a compensation chamber, a condenser, a liquid line, and a vapor line, the configurations of LHP are more complex and the manufacturing process is more expensive than that of the conventional heat pipe. The novel design of LHP without compensation cavity is theoretically conducted herein and the prototype will be manufactured and experimental investigated later.

3.3.2 Capillary Limit

For a functional LHP, one of the important heat transport limitations is the capillary limit, namely, the total pressure drop occurring in the loop should not surpass the maximum capillary pressure head generated in the evaporator wicks. This limit mathematically can be expressed as

$$\Delta p_{cap,\max} \geq \Delta p_{loop} \tag{3-33}$$

where $\Delta p_{cap,\max} = 2\sigma \cos\alpha / r_{e,\min}$ .The total pressure drop, Δp_{loop} , along the loop can be found by

$$\Delta p_{loop} = \Delta p_{vl} + \Delta p_{ll} + \Delta p_{w,e} + \Delta p_{w,c} + \Delta p_c + \Delta p_e + \Delta p_g \tag{3-34}$$

where Δp_{vl} is the pressure drop occurring in the vapor line, Δp_{ll} the pressure drop in the liquid line. Assuming that the vapor is saturated in the evaporator and condenser, the pressure drop in the vapor line at a steady-state condition can be related to the saturation pressure difference between the condenser and evaporator, i.e.,

$$\begin{aligned} \Delta p_{vl} &= p_s(T_e) - p_s(T_c) = f_v \left(\frac{L_v}{D_v} \right) \left(\frac{1}{2} \rho_v \bar{u}_v^2 \right) \\ &= f_v Re_v \left(\frac{2\mu L_v Q}{\pi D_v^4 \rho_v h_{fg}} \right) \end{aligned} \tag{3-35}$$

where, $f_v = \dfrac{0.3164}{Re_v^{0.25}}$ for the turbulent flow, or $f_v = \dfrac{64}{Re_v}$ for the laminar flow in the vapor line.

If the heat load is given, the pressure drop between the evaporator and condenser can be calculated by Eq. (3-35). Liquid flow in the liquid line can be considered as an incompressible Newtonian fluid with fully developed laminar flow at steady state and its pressure drop can be predicted by

$$\Delta p_{l,l} = \frac{128 \mu_l \dot{m}_l L_l}{\pi \rho_l D_l^4} \tag{3-36}$$

Based on Darcy's law, the pressure drop of liquid flow occurring in the evaporator and condenser wicks can be calculated by

$$\Delta p_{w,e} = \frac{\mu_l \dot{m}_l L_{w,e}}{K_{w,e} A_{w,e} \rho_l}, \text{ and } \Delta p_{w,c} = \frac{\mu_l \dot{m}_l L_{w,c}}{K_{w,c} A_{w,c} \rho_l} \tag{3-37}$$

respectively, where, $K = \frac{r_p^2 \varepsilon^2}{37.5(1-\varepsilon)^2}$. The pressure losses during the phase change processes in the evaporator and condenser [36] are given by

$$\Delta p_c = \frac{\dot{m}_v}{A_c}\sqrt{2\pi R_v T_v}\ , \text{ and } \Delta p_{ev} = \frac{\dot{m}_v}{A_{ev}}\sqrt{2\pi R_v T_v} \tag{3-38}$$

respectively. The effective hydrostatic pressure drop can be calculated by the height difference between the evaporator and the condenser, i.e.,

$$\Delta p_g = \rho_l g L_{eff} \sin\phi \tag{3-39}$$

For the steady-state condition, the vapor mass flow rate in the vapor line is equal to the liquid mass flow rate in the liquid line and can be expressed by

$$\dot{m}_v = \dot{m}_l = Q_{tot} / h_{fg} \tag{3-40}$$

Using Eqs. (3-33) to (3-40), the maximum heat transport capacity of capillary limit can be predicted.

3.3.3 Theoretical Analysis of Heat Transfer in LHP

3.3.3.1 Evaporation Heat Transfer on Sintered Particles Surface

The total temperature drop occurring in the LHP primarily is due to the thermal resistances occurring in the evaporator and condenser. As shown in Fig. 3-10, when heat is added on the bottom shell of evaporator, it transfers through porous layer (region I) by conduction, and reaches the top surface (region II), where the evaporation heat transfer takes place at the vapor-liquid-solid interface. The thin film region illustrated in Fig.3-10 (d) can be divided

into non-evaporating zone, evaporating thin film zone, and bulk liquid zone. For the porous layer (region I), the temperature drop across the layer can be calculated by heat conduction, where the effective thermal conductivity can be found by text books, such as Faghri [12], and Peterson [13]

$$k_{eff} = \frac{k_s\left[2k_s + k_l - 2\varepsilon\left(k_s - k_l\right)\right]}{2k_s + k_l + \varepsilon\left(k_s - k_l\right)} \tag{3-41}$$

Heat transfer in the region II is directly related to the thin-film-evaporation heat transfer on the curved surface. If the particle radius is given and the thin film thickness determined, the local evaporating heat flux through the thin film can be approximately expressed as

$$q_p^{'} = k_l \frac{T_p - T_{lv}}{\delta_{loc}} \tag{3-42}$$

where, $T_{lv} = T_v\left[1 + \frac{\Delta p}{\rho_v h_{fg}}\right]$, and $\Delta p = k\sigma + p_d$.

The evaporating thin film profile on the particle is governed by

$$\sigma\frac{dk}{dS} + k\frac{d\sigma}{dS} - \frac{dp_d}{dS} = \frac{dp_l}{dS} \tag{3-43}$$

Using the coordinate transformations, $S = r_p\vartheta$, Eq. (43) can be rewritten as

$$\sigma\frac{dk}{d\theta} + k\frac{d\sigma}{d\theta} - \frac{dp_d}{d\theta} = \frac{dp_l}{d\theta} \tag{3-44}$$

where, $p_d = -\frac{A}{\delta^3}$, $A = 10^{-19}$ J. The non-evaporation thin film thickness can be obtained by

$\delta_0 = \left[AT_v \Big/ \left(T_p - T_v\right)\rho_v h_{fg} \right]^{1/3}$, and the curvature of meniscus of the evaporating thin film can be expressed as

$$k = \frac{-\frac{d^2\delta}{d\theta^2}\left(\delta + r_p\right) + 2\left(\frac{d\delta}{d\theta}\right)^2 + \left(\delta + r_p\right)^2}{\left[\left(\frac{d\delta}{d\theta}\right)^2 + \left(\delta + r_p\right)^2\right]^{3/2}} \tag{3-45}$$

The pressure drop occurring in the thin film region can be found by

$$\frac{dp_l}{d\theta} = -\frac{\mu_l \int_0^{r_p \vartheta} \frac{q(s)}{h_{fg}} r_p d\vartheta}{\rho_l \left[\frac{3}{2}\delta^2 + r_p\delta + \left(r_p + \delta\right)^2 \ln\left(\frac{r_p}{r_p + \delta}\right)\right]} \tag{3-46}$$

The required boundary conditions to solve Eq. (44) can be summarized as

$$\delta\big|_{\theta=0} = \delta_0, \quad k\Big|_{\theta=0} = k_0 = \frac{1}{r_p + \delta_0}, \quad \frac{d\delta}{d\theta}\Big|_{\theta=0} = 0 \tag{3-47}$$

Solving Eqs. (3-44)-(3-46) with boundary conditions shown in Eq. (47), the thin film thickness profile, δ, on the particle surface can be calculated. And the evaporating heat transfer through one particle may be found by

$$Q_p = \int_0^{\vartheta} 2\pi r_p^2 \cos\left(\gamma - \vartheta\right) \frac{k_l\left[T_p - T_{lv}\left(\vartheta\right)\right]}{\delta\left(\vartheta\right)} d\vartheta \tag{3-48}$$

where, $\gamma = \cos^{-1}\left(\frac{r_p}{r_e + r_p}\right)$, and the meniscus radius, r_e, is assumed to be constant at a given heat load. If the total number of particles at the top surface of wick is N, the total evaporating heat transfer can be obtained by

$$Q = NQ_p \tag{3-49}$$

The total number of particles, N, in Eq. (49) should be found in order to calculate the total evaporating heat transfer. For uniform particles, Peng and Ma [38] developed on e model and concluded that the sintered particles consist of only three structures is stable, as shown in figure 3-11, the percentages for the triangular, rectangular, and hexagonal structures are 45%, 28%, and 27%, respectively. Then, the number of particles can be approximately found by:

$$N = \frac{S_{top}}{r_p^2}\left[\frac{1}{4\sqrt{3}} \times 45\% + \frac{1}{4} \times 28\% + \frac{2}{3\sqrt{3}} \times 27\%\right] \tag{3-50}$$

where S_{top} is the flat bottom surface area of evaporator, and r_p is the radius of sintered particles. Once the evaporating thin film profile is obtained, the heat transfer through one

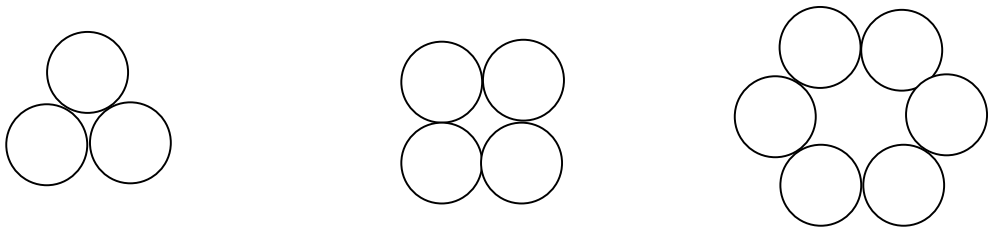

(a) (b) (c)

Fig. 3-11 Particles distribution on the surface of evaporator

particle is determined at a given temperature difference or the temperature difference can be calculated at a given heat load.

3.3.3.2 Condensation Heat Transfer in the Condenser

The condenser was made from a flat copper plate. The vapor passages in the condenser consist of rectangle channels. When condensation occurs in the condenser, the latent energy of the vapor is released. The condensation heat transfer can be considered as a film condensation in horizontal rectangle grooves. The velocity of vapor flow decreases along the condenser direction and equal to zero at the end of condenser. The inlet Reynolds number can be predicted by

$$Re_{v,i} = \frac{\rho_v u_{v,i} D_h}{\mu_v} \tag{3-51}$$

where, $D_h = 4A/P$, $A_{inlet} = ab$, $P_{inlet} = 2(a+b)$, and a and b are the width and height of inlet channel, respectively. $u_{v,i}$ in Eq. (3-51) is the inlet velocity in the condenser and can be expressed by

$$u_{v,i} = \frac{Q_{total}}{Nab\rho_v h_{fg}} \tag{3-52}$$

Since the inlet velocity of vapor flow is not very high and $\mathrm{Re}_{v,i} < 35000$, the average heat transfer coefficient in the condenser can be predicted by

$$\overline{h_D} = C\left[\frac{g\rho_l(\rho_l - \rho_v)k_l^3 h_{fg}'}{\mu_l(T_{sat} - T_{cw})D_h}\right]^{1/4} \tag{3-53}$$

where, $h_{fg}^{'} = h_{fg} + \frac{3}{8} c_{p,l} \left(T_{sat} - T_{cw} \right)$, and Chato [29] recommended the constant C is equal to 0.555. Therefore, the temperature difference across the condensation film at a given heat load can be predicted by

$$\Delta T = \left(\frac{Q_{total}}{CA_{total}} \right)^{4/5} \left[\frac{g \rho_l \left(\rho_l - \rho_v \right) k_l^3 h_{fg}}{\mu_l D_h} \right]^{1/5} \tag{3-54}$$

where, $A_{total} = \sum_{i=1}^{8} 2\left(a_i + b \right) L_i$ is the total interior condensing area.

3.3.4 Experimental System of LHP

In order to verify the theoretical prediction, an experimental system shown in Fig. 3-12 was established. The system consisted of the test section of LHP, data acquisition, power supply and measurement, and cooling system. The test section was a miniature LHP which included vapor and liquid lines, condenser, and evaporator. The liquid line was fabricated from a copper tube which has a length of 33 cm with inside and outside diameters of 2.29 mm and 2.36 mm, respectively. The length of the vapor line is the same as the liquid line, but its inside and outside diameters are 3.4 mm and 4.0 mm, respectively. The evaporator and condenser were directly made from a 12-mm-thick copper plate. The evaporator has dimensions of 10.8 mm in depth, 30 mm in width, and 30 mm in length. The 0.8-mm-thick wick was placed on the 3×3 -cm^2 bottom of the evaporator. The wick consisted of the sintered copper particles at a diameter of 50 μm. The outside dimensions of condenser were 15cm length, 7cm wide and 12mm high. The rectangle channel formed in the condenser has a uniform depth of 10.8mm and a variable width from 10 mm at the inlet connecting the vapor

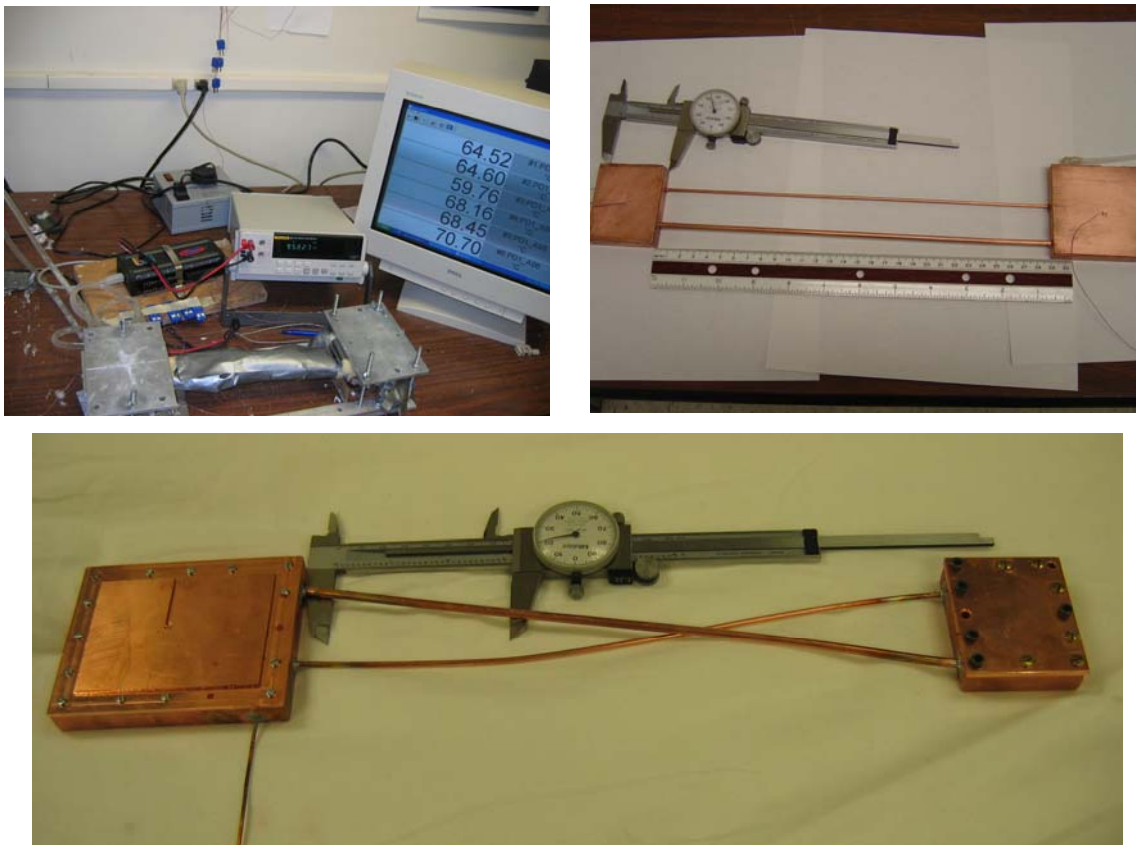

(a) Test sections

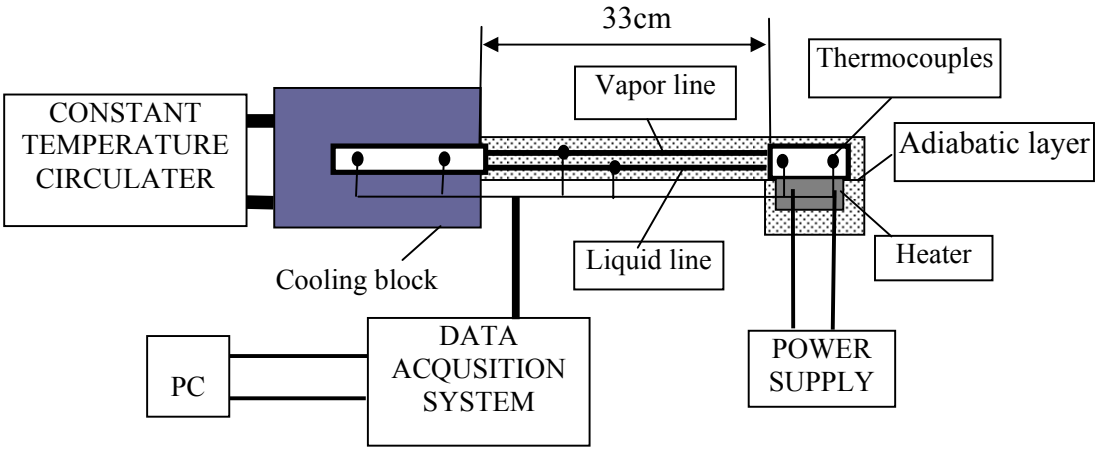

(b) Experimental system

Fig. 3-12 Photo of LHP prototype and schematic of experimental system

line to 5 mm at the outlet connecting the liquid line. The cooling unit consisted of two flat aluminum cooling blocks were directly attached to the condenser. The thermal paste of omegatherm "201" was used between the aluminum cooling block and the condenser to reduce the contact thermal resistance. One electronic heater coil with a maximum heat load of 260W was used to provide the heat added on the evaporator. Six thermocouples were used to measure the temperatures of the condenser, vapor and liquid lines, and evaporator. The data acquisition system consisted of a PC, thermocouples and data acquisition card. The maximum temperature measurement error of the current investigations were less than $\pm 0.1°C$ and the heat loss was less than 3%.

Prior to the start of the experiment, the system was allowed to equilibrate and reach steady-state such that the temperature of the cooling bath and the heat pipe were constant at 60 ± 0.1°C. When the desired steady-state condition had been obtained, the input power was increased in small increments. The test indicated that a time of approximately 30 minutes was necessary to reach steady-state. To obtain the data for the next successive power level, the power was incremented every 30 minutes. During the tests, the thermal power and the temperature data were simultaneously recorded using an iOtech Daq/56 data acquisition system controlled by a personal computer.

3.3.5 Results and Discussion

Using the mathematical model describe above, the heat transport capability in the LHP can be predicted. It should be noted that the following assumptions are utilized in the calculation: 1) Previous results [15, 17, 18, 22, 31] indicate that most of the heat added on the solid wire

will transfer through the thin film region. As a result, it is assumed that the heat added on the particle is equal to the total evaporating heat transfer through the thin film region. 2) The vapor is saturated and ideal gas. 3) The meniscus radius of liquid-vapor interface on the sintered particles in the evaporator is constant at any given heat load. 4) When the film thickness increases, the disjoining pressure effect decreases until it is so small that it can be neglected. The length of thin film region is determined by the cut-off value of 0.02 Pa of disjoining pressure. If the K reach $1/r_e$ before the disjoining pressure drop arrive 0.02Pa, the thin film profile will be approximately calculated by $\delta = \frac{r_p r_e \left[1-\cos\left(1+r_p/r_e\right)\theta\right]}{r_p + r_e \cos\left(1+r_p/r_e\right)\theta}$. 5) The water temperature of cooling system kept constant and was 60°C, thermophysical properties of working fluid were at $60^0 C +$ superheat are used in the calculation. The calculation process can be summarized as following for any given heat load:

1) Select contact angle α.
2) Select superheat ΔT
3) Meniscus radius r_e calculation by equations (1)-(8)
4) Solve equations (11)-(15) to get the thin film profile
5) Calculate heat flux profile by equation (10) and integrate equation (16).
6) Calculate the total heat load by eq. (17) with eq. (18) and compare the prediction with the given heat load. If the error is greater than 0.5W, then go to step 2.
7) When the error between the prediction and the given heat load is less than 0.5W,

output the superheat, thin film profiles, meniscus radius r_e and heat flux distributions.

Figure 3-13 depicts that average evaporator meniscus radius r_e versus heat load input at different contact angle. For any contact angle, as shown in Fig. 3-13, the radius r_e decrease with the heat load rise in order to create high enough capillary force and overcome the flow resistance caused by the vapor/liquid flow velocities increase. The contact angle play very important role for the radius of r_e at given heat load since the capillary force and length of thin film evaporating region depends on contact angle. For any given heat load, the

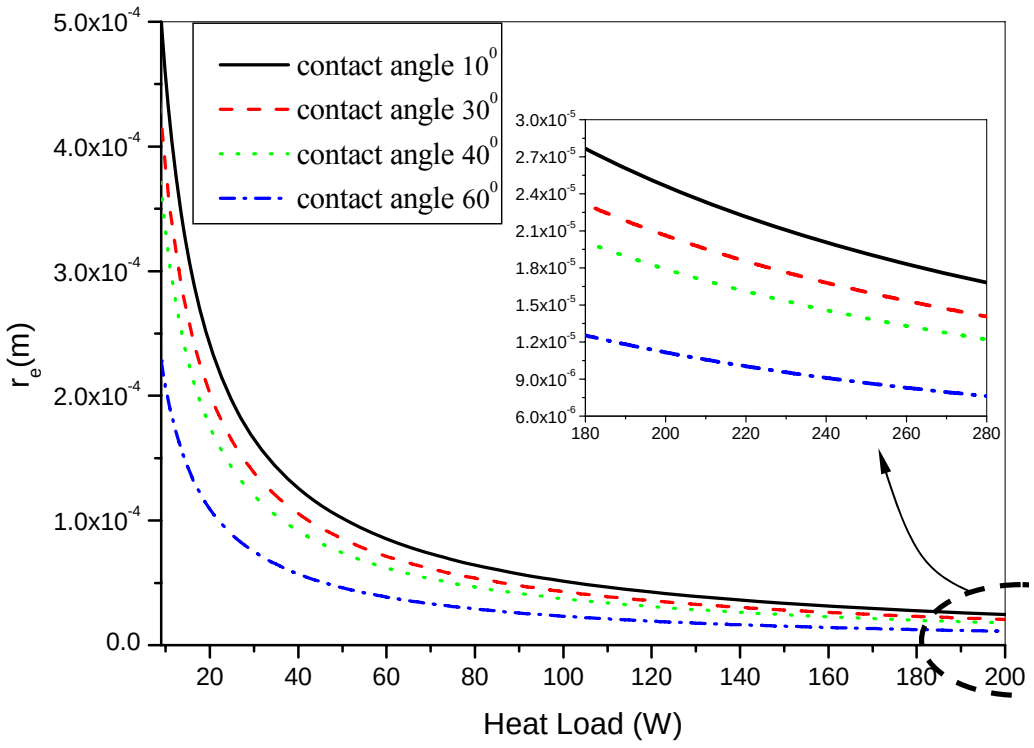

Fig.3-13 Average evaporator meniscus radius r_e versus heat load input at different contact angle

superheat at big contact angle will be higher than that at small contact angle because the heat load mainly pass through the thin film region [4, 5, 17, 18] and the contact angle increase resulting in the length of thin film evaporating region descend. The thermal properties of working flow depend on the superheat, especially, the term of $\frac{\mu_v}{\rho_v}$, which result in the total flow resistance of vapor/liquid lines increase and further make the r_e descend. For example, the radius of r_e is $0.050cm$, $0.042cm$, $0.037cm$, and $0.023cm$ while the heat load is 9W, and the contact angle is 10^0, 30^0, 40^0, and 60^0, respectively.

Figure 3-14 illustrates the effects of the curved surface and contact angle on the thin

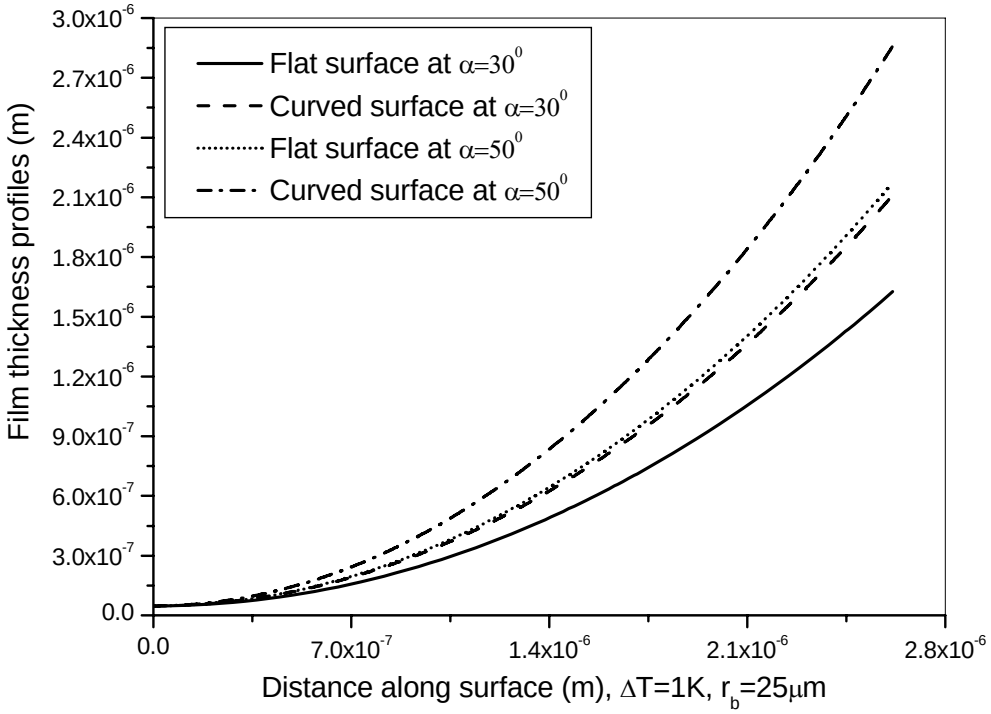

Fig.3-14 Comparison the thin film profile on curved and flat surface at different contact angle

film profiles. When the contact angle increases, the length of thin film region decreases on both the flat and curved surfaces. At a given contact angle, the length of evaporation thin film on the curved surface is much shorter than that on the flat surface. Clearly, the heat transfer rate through the thin film region on the curved surface is much lower than that on a flat surface. It should be noticed that this heat transfer rate is based on the actual solid surface area. For a surface consisting of a number of sintered particles, the actual solid surface area is much larger than the area projected on a horizontal plane. When the sintered particles become smaller, the number of thin film region increases resulting in a significant increase of the total thin film region. Although the heat transfer rate per unit of actual surface area on a curved surface is lower than that on a prefect flat surface, the heat transfer rate per unit of area projected on a horizontal plane is much higher. Clearly, when the surface consists of the sintered particles, the evaporating heat transfer per unit of area projected on a horizontal plane can increase. While the sintered particles on a surface can increase the thin film evaporation region and enhance the evaporating heat transfer rate per unit of area projected on a horizontal plane, the sintered particles play a key role in pumping the working fluid from the condenser to the evaporator.

The non-evaporation thin film thickness can be determined by $\delta_0 = \left[A T_v \Big/ \left(T_p - T_v\right) \rho_v h_{fg} \right]^{1/3}$ and the heat flux through the thin film region calculated by 1-D conduction heat transfer. When a superheat (T_p-T_{lv}) between the solid surface of particles and the interface temperature exists, the high heat flux takes place in the thin film evaporation region. As shown in Fig. 3-15, this superheat drastically affects the evaporation thin film

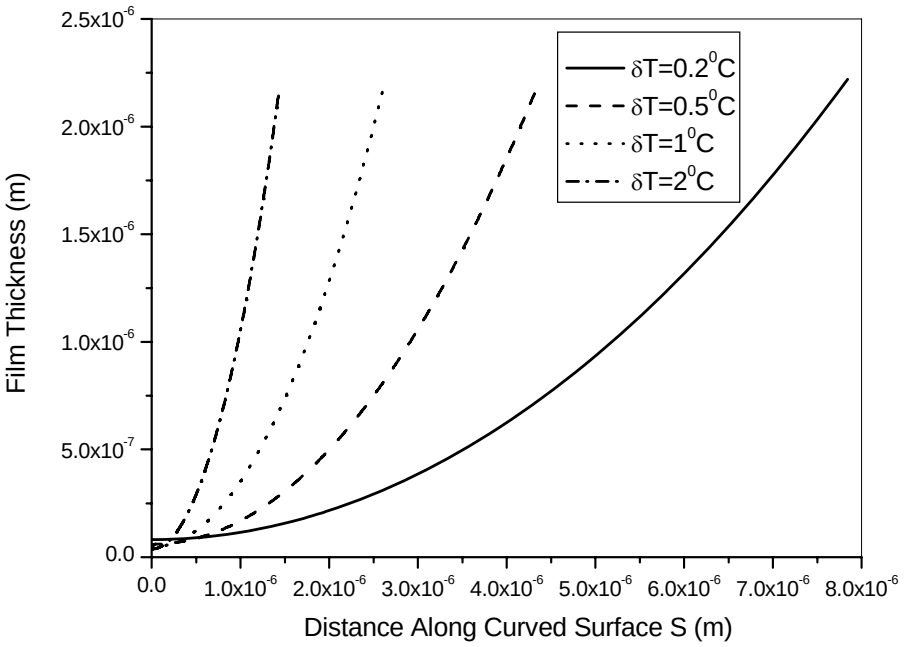

(a)

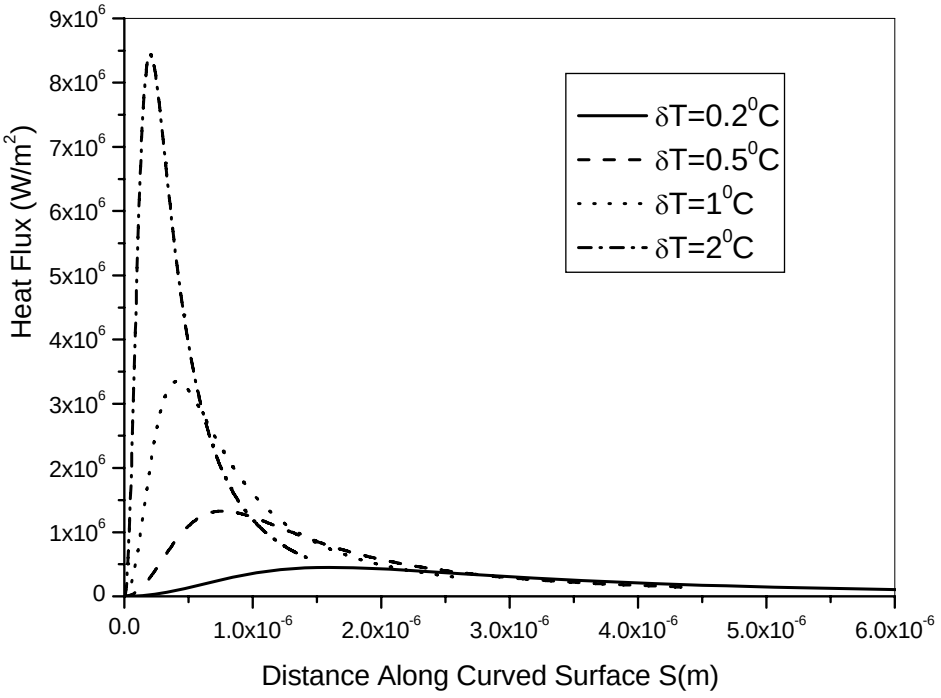

(b)

Fig.3-15 Effects of superheat temperature on the thin film profiles and heat flux distribution on curved surface (a) thin film (b) heat flux

profiles both in length and shape. And a larger superheat results in a higher heat flux and higher mass flow rate in the thin film region, which directly increases the viscous pressure drop over a given length. In order to maintain steady-state evaporating heat transfer in the thin film region and pump enough liquid to the thin film region, the disjoining pressure must increase and overcome the viscous pressure drop and the pressure difference due to the curvature variation. As shown in Fig. 3-15(a), when the superheat increases, the thin film region decreases significantly. In other words, when the superheat increases, the thickness of evaporating thin film at a given location, S, increases significantly. At a higher superheat, the non-evaporating film thickness becomes thinner producing an even higher heat flux in the evaporating thin film region than the case with a smaller superheat. A comparison of the current theoretical results with the previous results [15] on the flat surface shows that the effects of the curvature of particle surface on the thin film profile and heat flux distribution should be considered.

As shown in Fig. 3-16, the experimental results show that the LHP can transport a heat flux up to 75 W/cm^2. Figure 3-16 also illustrates a comparison between the experimental data and theoretical prediction of temperature response in the evaporator and condenser. As shown in Fig. 3-16(a) and (b), the theoretical prediction agrees well with the experimental data both in the condenser and evaporator. When the heat flux is higher than 54 W/cm^2, however, the model cannot predict the temperature response of the evaporator. The main reason is that the model does not consider the secondary flow occurring in the thin film region. When the heat flux is higher, the dynamic contact angle increases and the surface tension near the contact line decreases, which will develop the secondary flow in the thin

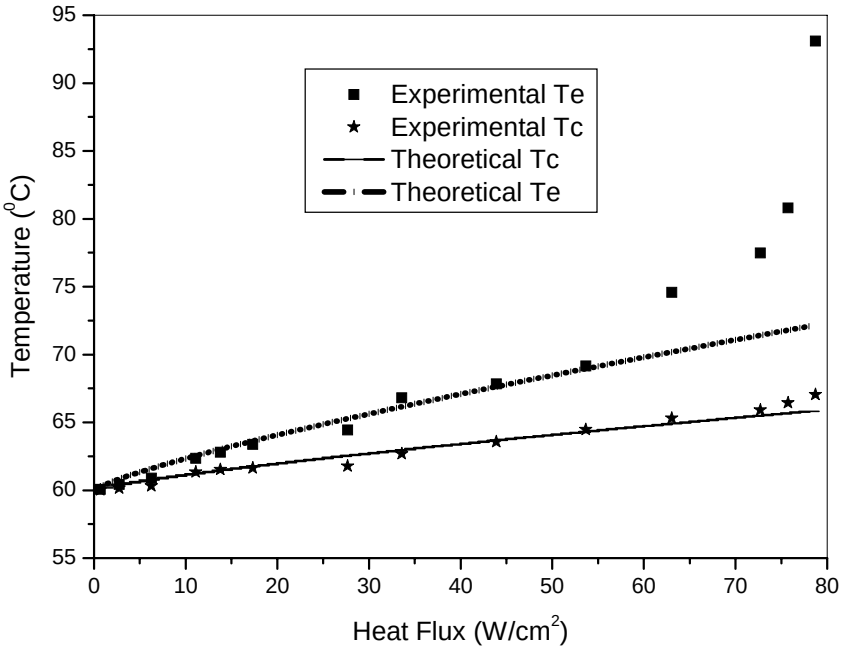

(a)

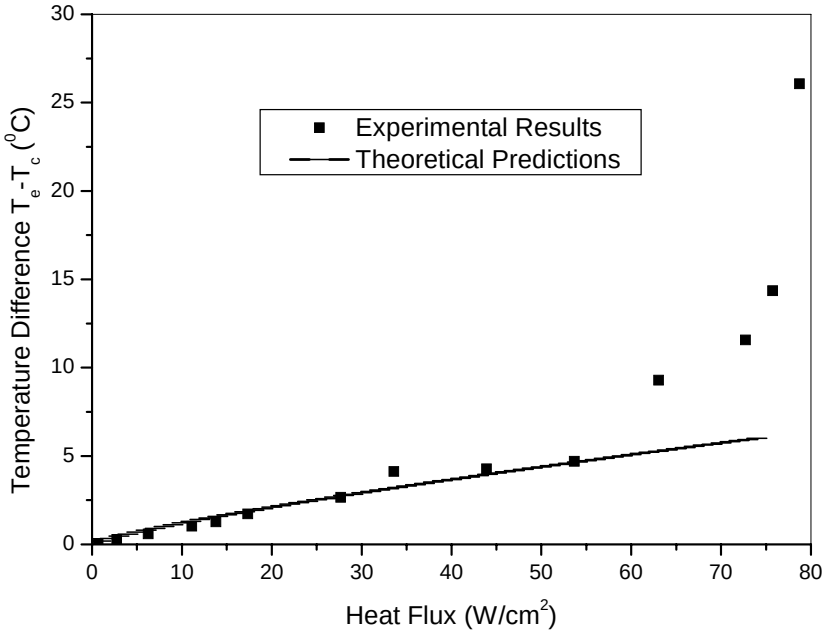

(b)

Fig.3-16 Comparisons the theoretical prediction results with experimental data at different heat flux. (a) temperature response in evaporator and condenser (b) temperature difference between the condenser and evaporator

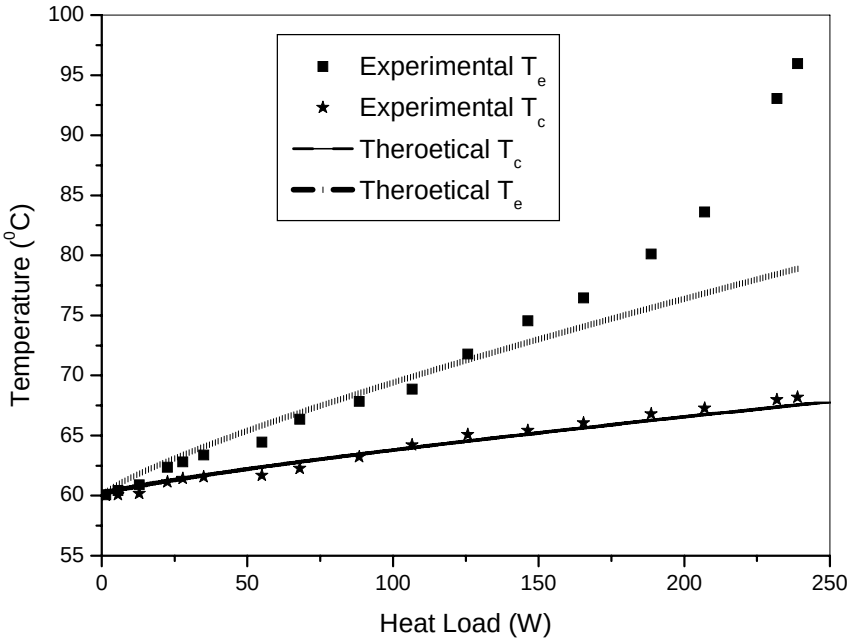

(a)

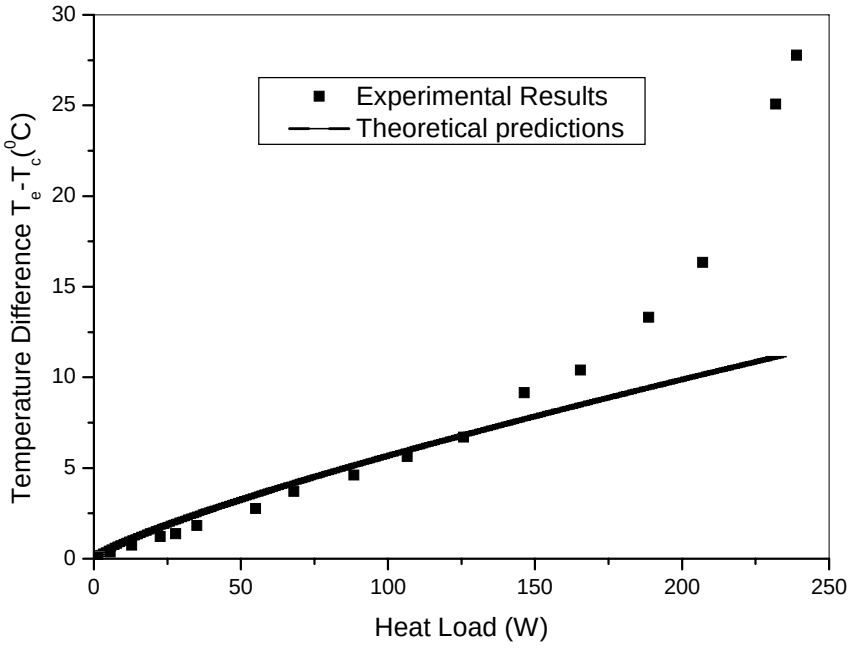

(b)

Fig.3-17 Comparisons the theoretical prediction results with experimental data at different heat load. (a) temperature response in evaporator and condenser (b) temperature difference between the condenser and evaporator

film region and directly reduce the length of thin film region. As a result, the evaporating heat transfer significantly decreases.

Figure 3-17 shows the heat load effect on the temperature responses of evaporator and condenser including a comparison with the theoretical prediction. As shown, the LHP can transport a heat load up to 230 W without dry-out. Similarly, while the theoretical prediction agrees well with the experimental data when the heat load is less than 150W, the model cannot predict the heat transfer performance if the heat load is higher than 150W. Clearly, a new model including the secondary flow induced by the surface tension gradient and larger contact angel should be developed.

3.5 Summarize

A detailed mathematical model for the thin film evaporating heat transfer on curved surface was developed. The effects of gravitational force and contact angle on the thin film profiles and heat flux distribution on the curved surface are investigated. The theoretical results show that the gravity effect on thin film distributions and heat flux profiles on curved surfaces cannot be neglected. The results also indicate that while the thin-film-evaporation region on the curved surface is smaller than that on a flat surface, the sintered particles effectively increase the thin film region per unit of area projected on a horizontal plane and enhance the total heat transfer capability. Based on the capillary limit and thermal resistance, the maximum heat transport capacity of the heat pipes is predicted.

In order to confirm the theoretical investigation, prototypes of miniature FHP with wire core groove and LHP with flat sintered evaporator have been manufactured and experimentally investigated. For miniature FHP, when the heat pipes were operated at the

Case II, heat load reached its maximum transport capacity since the further increase of heat load would result in the sharp increase of the temperature drop due to the heat transfer degradation in thin film evaporation although the heat pipe has not reached the capillary limit. The comparison with the experimental data shows that the theoretical model can be used to precisely predict the temperature response of the evaporator and condenser in the Cases I and II. For miniature LHP, the experimental results show that the LHP investigated herein can remove a heat load 230 W with a heat flux up to 75 W/cm^2. While the theoretical prediction of the temperature responses of evaporator and condenser agrees well with the experimental results, the model cannot be used to predict the temperature response of evaporator if the heat flux is higher than 54 W/cm^2 or the heat load is over 150W. The current investigation will assist in the optimum design of curved-surface wick to enlarge the thin film evaporation region and enhance the evaporation heat transfer of the heat pipe, and a better understanding of the heat transfer mechanisms in miniature heat pipes.

CHAPTER 4 MODELING HEAT TRANSFER OF CELL FREEZING PROCESS AND EXPERIMENTAL INVESTIGATION OF CRYOGENIC OSCILLATING HEAT PIPE

4.1 Introduction

Cells are damaged during equilibrium cooling by one or both of two mechanisms: the injury induced by intracellular ice formation (IIF) and by slow-cooling or solution effects [40]. The latter is often caused by the exposure cells to high intracellular and extracellular solute concentrations during a relatively long cooling time. Many previous reports have focused on the intracellular ice formation mechanisms because it is typically fatal to the cell. Mazur [41, 42], Toscano et al [43], and other investigators [44, 45] try to setup model to predict IIF. However, the prediction of the probability of IIF for a given freezing protocol has met with very limited success [46] because its complexity mechanisms are not known clearly. Recently, Wolfe and Bryant [47] simply suggested that the damage caused with the IIF is due to the poor solvent in terms of molecules solution, thermodynamic and mechanical properties.

When an aqueous solution freezes, water precipitates as ice and the remaining unfrozen solution has a progressively high solute concentration [47]. These high solute concentrations eventually become damaging to cells and tissues [40, 48]. In addition, ice and water interact differently with the hydrophilic surface, and the surface tension of water may play a role in maintaining the native state of enzymes [47]. The ice crystallization may result

in the mechanical damage to the cellular ultra-structure either by the direct action and/or by the volumetric expansion that accompanies. Therefore, avoiding IIF during the cooling process is the key in cryopreservation.

4.1.2 Vitrification and Open Pulled Straw (OPS) Method

Vitrification as an alternative method could completely avoid cell damage by preventing IIF and abstaining ice crystal formation (intra or extracellular). One way to vitrify cells is to use a higher concentration of vitrification solution, in which the cooling rate can be very low and the available cooling technologies can achieve the required cooling rate. The high concentration of vitrification solution, however, often has undesired toxic and osmotic effects on the cell survival. Another way to achieve vitrification is to use an extra-fast cooling rate, which can significantly decrease the concentration of cryoprotective agent mixture, and directly reduce osmotic and toxic effects. In addition, the extra-fast cooling rate can make the cooling process to rapidly pass through the "dangerous" temperature zone, which would lessen severe chilling-injury. Many investigators [55, 56] have directly plunged the cell-containing medium into liquid nitrogen or employed the microdroplet method to increase the temperature difference and increase the cooling rate. Recently, the open pulled straw (OPS) method [54-57] has been widely used in cryopreservation, which could reach a relatively high cooling rate of about 20,000 K/min. The foundational methodology for the OPS method is to use a decreased diameter of straw to increase the ratio of surface area to volume, resulting in a practically achievable higher cooling rate. However, the cooling rate provided by either the OPS or microdroplet methods is much lower than the critical cooling rate

theoretically predicted [49]. Examining all available cooling approaches, it is clear that methods such as the OPS and microdroplet methods are primarily based on the temperature difference between the cooling medium, such as liquid nitrogen, and the sample to increase the cooling rate. Due to the liquid nitrogen saturation temperature limit, it is not possible to further increase the temperature difference for a higher cooling rate. Increasing the heat transfer coefficient might be a new way to further increase the cooling rate.

4.1.3 Dangerous Temperature Range (DTR)

In the previous investigations, Ren and his colleagues [50] who based on Bouttron's [49, 51] semi-empirical crystallization theory developed an exact analytical expression for the quantity variation of ice crystallization by the integral method without considering the finite expansion. Theoretical results [50, 51] show that the crystallization peak zone exists, and this temperature range takes place often between 240 K and 200 K. Boutron and his colleagues [53, 54] further found when ice crystallizes from a wholly amorphous solution, it is first cubic, then ordinary hexagonal ice and normally consider that the damage always occurs following the transition from cubic into hexagonal ice, namely, the subsequent recrystallization of hexagonal ice is the primary reason for the injury but the intracellular cubic ice would be innocuous. In here, the transition temperature region or the temperature region of the crystallization peak zone has been considered as Dangerous Temperature Region (DTR) in the cell freezing. The crystallization peak upon cooling and devitrification peak upon thawing can be predicted by [50, 51, 53],

$$\frac{dC}{dt} = 79.78 \frac{q_0}{100} \frac{dx}{dt} \tag{4-1}$$

where dC/dt (cal/min/g), which can be measured experimentally, is the heat received by the sample, and q_0 is the maximum heat released during crystal process. As shown in Fig. 4-1, the ice formation mainly occurs at the beginning of cooling process, i.e., the temperature zone from 200K-240K. This temperature zone can be called as the dangerous temperature region (DTR) because most of IIF and cell damage mainly create in this temperature region. Quickly passing through this temperature region will play a key role in increasing the cell survival rate.

In addition, investigations [50-53] on the time temperature transformation (TTT) and its derivative continuous-cooling (CT) diagram in assessing the critical cooling rates required for the glass formation have resulted a correlation between the freezing time and the extent of

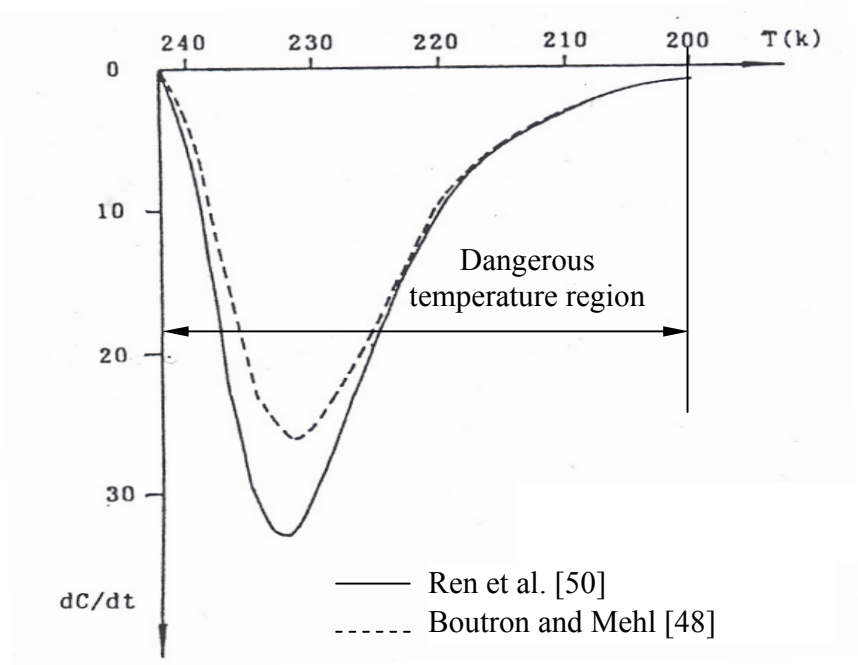

Fig. 4-1 Theoretical prediction of crystallization peaks at a cooling rate of 40 K/min (the solution is 35% 1,2-propanediol, *dC/dt* is in cal/min/g)

given volume fraction of solid phase. These theoretical results show that the required cooling rate is extremely high, up to 10^7 K/min for pure water with volume fractions of crystals, i.e., $x \le 10^{-6}$. Routinely achieving these is practically impossible using current technologies. Clearly, producing an ultra-high cooling rate would be a significant advancement in the area of practically employing vitrification as a cryopreservation methodology. Fortunately, previous investigations [58] show that oscillating motions result in thermal diffusivity up to 17,900 times higher than those without oscillations in the capillary tubes and the ultra-high heat flux could be obtained by thin film evaporation [9, 25]. With those advances in the cooling technology and combining a nanofluid as the working fluid, the cooling rate could be significantly increased [70].

4.2 Transient Heat Transfer Model in Cell Freezing Process

In the model developed here, we define the vessel containing the biological units (here cells or tissues) as a long thin straw filled with solutions and cells (similar to the OPS approach). As shown in Fig. 4-2, the oscillating motion of vapor bubbles and liquid plugs, plus the phase-change heat transfer in the coolant passages will significantly increase the heat transfer coefficient. In order to simplify the problem, it is assumed that the thermal conductivity of cells is the same that for the extracellular solution. The energy equation governing the temperature distribution for the physical model shown in Fig.4-2 can be expressed as:

$$\frac{1}{r}\frac{\partial}{\partial r}\left(kr\frac{\partial T}{\partial r}\right)+\frac{\partial}{\partial z}\left(k\frac{\partial T}{\partial z}\right)+\dot{q}=\rho c_p\frac{\partial T}{\partial t} \qquad (4\text{-}2)$$

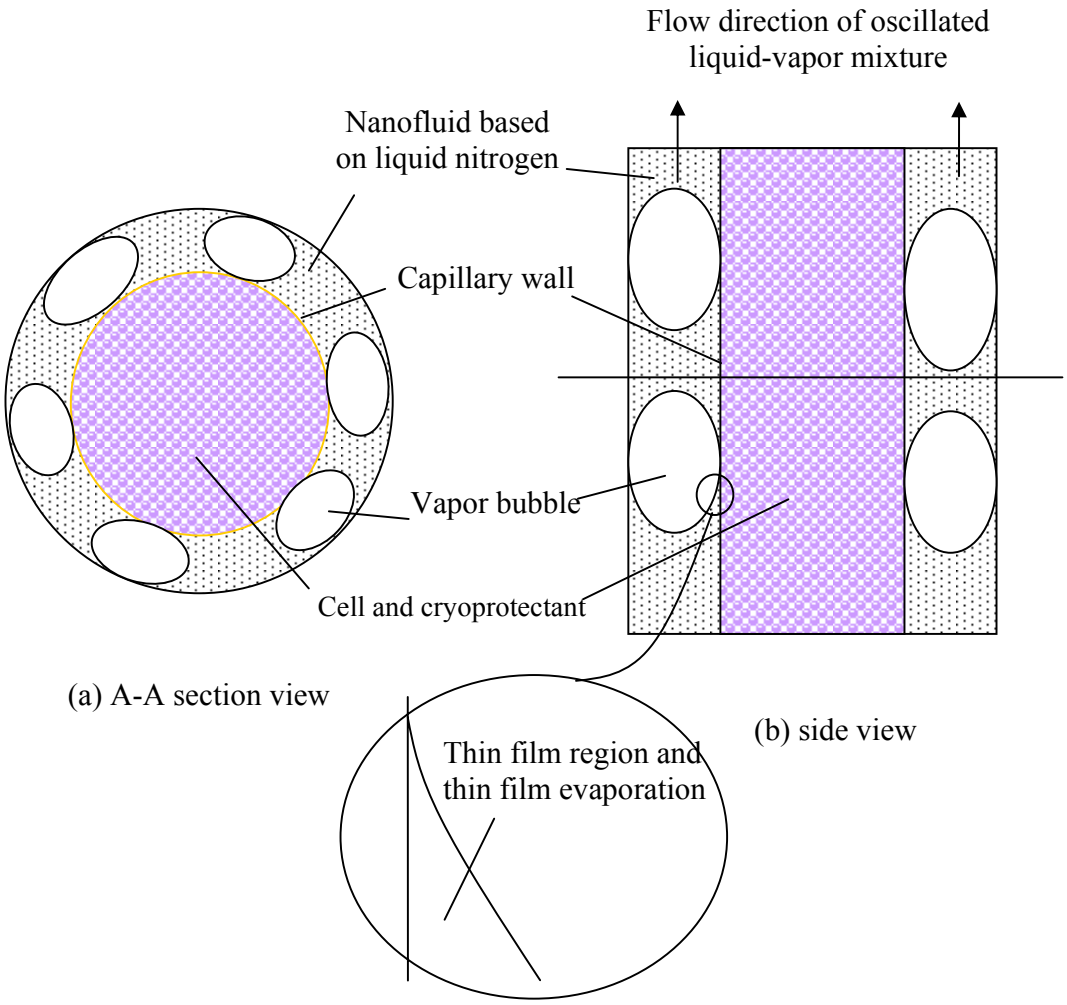

Fig.4-2 Schematic diagram of the theoretical analysis model of cell freezing

Because the straw diameter ($d_0 = 100\mu m$ was selected in the theoretical analysis) is much smaller than the straw length, it is reasonable to assume the cell container as an "infinite cylinder." No heat is generated in the cell, namely, $\dot{q} = 0$. Equation (4-2) can be simply rewritten as

$$\frac{1}{r}\frac{\partial}{\partial r}\left(r\frac{\partial T}{\partial r}\right) = \frac{1}{\alpha}\frac{\partial T}{\partial \tau} \tag{4-3}$$

With the initial temperature, T_0, and the boundary condition, T_∞, the transient temperature distribution can be written as:

$$\theta^* = \sum_{n=1}^{\infty} C_n \exp\left(-\zeta_n^2 Fo\right) J_0\left(\zeta_n \frac{r}{r_0}\right) \tag{4-4}$$

where

$$\begin{aligned} \theta^* &= \frac{T - T_\infty}{T_0 - T_\infty}, \quad Fo = \frac{\alpha t}{r_o^2} \\ Bi &= \zeta_n \frac{J_1(\zeta_n)}{J_0(\zeta_n)}, \quad C_n = \frac{2}{\zeta_n} \frac{J_1(\zeta_n)}{J_0^2(\zeta_n) + J_1^2(\zeta_n)} \end{aligned} \tag{4-5}$$

4.3 Ice Crystallization Model in Cell Freezing

With the predicted temperature variation, the ice quantity formed in the solution can be determined. A number of previous reports [49-53] have described both experimental investigations and theoretical analysis on the ice formation process. One typical equation used for the speed (V) of a crystal edge is expressed as

$$V = \frac{L(T_m - T)}{3\pi\lambda^2 v T_m} \exp\left(-Q/RT\right) \tag{4-6}$$

where T_m is the temperature at the end of melting or freezing process, Q is the activation energy, and R the gas constant, L the heat of fusion, λ the thickness of the transition layer between liquid and crystal, and v the viscosity. The maximum crystalline ice was observed at a very low cooling rate in a process can be considered as reversible process. Let x be the ratio of the quantity of ice at time t to the maximum crystallizable ice, $0 \le x \le 1$. As previously described [53], the derivative dx/dt can be found as:

$$\frac{dx}{a_1(x)} = k(T_m - T)\exp\left(-Q/RT\right)dt \tag{4-7}$$

where

$$k = \frac{L}{\pi\lambda^2 \nu T_m r_f} \tag{4-8}$$

$$a_1(x) = x^{2/3}(1-x) \tag{4-9}$$

The term $a_1(x)$ shown in Eq. (4-9) is called the "spherical crystals with a $1-x$ term" model, which has been widely used [49-51, 53]. With an assumption of $T = T_0 \pm \beta t$ for thawing or freezing process [48, 52], Eq. (4-7) can be expressed as:

$$\frac{dx}{a_1(x)} = k\left[T_m - (T_0 \pm \beta t)\right]\exp\left[\frac{-Q}{R(T_0 \pm \beta t)}\right]dt \tag{4-10}$$

Normally, the crystallization process can be considered as the vitrification process when the volume fraction of crystals is less than the degree detectable by DSC (Differential Scanning Calorimeter)(typically, $x = 10^{-6}$) [49, 51, 53]. If the volume fraction, x, is given, the theoretical critical cooling rate V_{cc} or warming rate V_{cw} can be calculated. For example, based on $a_1(x) = x^{2/3}(1-x)$, Ren et al. [48, 49] calculated the critical cooling rates of several aqueous solutions with the volume fraction of $x = 10^{-6}$ and $x = 5\times10^{-3}$, respectively. Those results show that when the cryopreservation solution concentration is very high, the order magnitude of critical cooling rates (K/min) for aqueous solutions is about 10^4.

As shown in Eq. (4-4), the temperature in cells depends on the location, r/r_0, and freezing time, t, therefore, the assumptions with a constant cooling rate and a linear

temperature variation with the freezing time are unreasonable in the whole freezing process. Integrating the right side of Eq. (4-7) with the assumption of $a_1(x) = x^{2/3}(1-x)$ and the temperature distribution predicted by the transient heat transfer model shown in Eq. (4-4), the ice crystallization rate x can be rewritten as:

$$A(x) = k\int_0^t [T_m - T]\exp\left[-Q/RT\right]dt \tag{4-11}$$

where,

$$\begin{aligned} A(x) &= \int_0^x \frac{dx}{x^{2/3}(1-x)} \\ &= -\ln(1-x^{1/3}) + \frac{1}{2}\ln\left(1+x^{1/3}+x^{2/3}\right) + \sqrt{3}\arctan\left[\sqrt{3}x^{1/3}\Big/\left(2+x^{1/3}\right)\right] \\ T &= T_\infty + \theta^*(T_0 - T_\infty) \end{aligned} \tag{4-12}$$

For a given r/r_0 and a heat transfer coefficient, θ^* (Eq. (4-12)) only depends on the freezing time and can be determined by Eq (4-4), i.e.,

$$\frac{dT}{dt} = -\frac{\alpha(T - T_\infty)\sum\zeta_n^2}{r_0^2} \tag{4-13}$$

Then, Eq. (4-11) can be found as:

$$A(x) = -\frac{k\,r_0^2}{\alpha\sum\zeta_n^2}\left[(T_m - T_\infty)\int_{T_0}^{T}\frac{1}{T-T_\infty}\exp\left(-Q/RT\right)dT - \int_{T_0}^{T}\exp\left(-Q/RT\right)dT\right] \tag{4-14}$$

Considering $\exp\left(-\frac{Q}{RT}\right) = \sum_{n=0}^{\infty}\frac{\left(-Q/RT\right)^n}{n!}$, Eq. (4-14) can be expressed as follows:

$$A(x) = -k r_0^2 \frac{(T_m - T_\infty)\int_{T_0}^{T} \frac{1}{T - T_\infty} \sum_{n=0}^{\infty} \frac{\left(-Q/RT\right)^n}{n!} dT - \int_{T_0}^{T} \sum_{n=0}^{\infty} \frac{\left(-Q/RT\right)^n}{n!} dT}{\alpha \sum \zeta_n^2} \quad (4\text{-}15)$$

Solving Eqs. (4-10), (4-13) and (4-4), the rate x versus the freezing temperature T or time t can be computed and predicted.

4.4 Theoretical Results and Discussion for Cell Freezing

The analysis presented by Ren et al. [50, 51], Boutron and Mehl [49] and Boutron [53] focus on the prediction of the critical cooling or warming rate. However, those results were based on the assumptions of the temperature uniform distribution in the freezing sample with a constant cooling rate in the whole freezing process. These investigations have resulted in a better understanding of mechanisms of heat transport in the cell freezing process. However, when the cooling rate increases, the temperature distribution in the cell is not uniform which directly affects the ice formation rate in the cell. In the current investigation, the effect of cooling rate on the temperature distribution in the sample can be predicted with the solutions shown in Eq. (4-4). Figure 4-3(a) illustrates the effect of the heat transfer coefficient on the temperature distributions along the cell radius direction at $t = 0.005\,s$. As shown in Fig. 4-3(a), the temperature distribution can be considered as uniform in the whole cell if the heat transfer coefficient, *h,* is under 500 W/m^{2}K, which is consistent with the results predicted by the lumped method ($Bi < 0.1$ at $h = 500$ W/m^{2}K). When the heat transfer coefficient increases, the temperature distribution is sharply non-uniform. For example, as h=1000 W/m^{2}K, the temperature distribution is almost uniform for r/r_0<0.82, but its distribution becomes non-

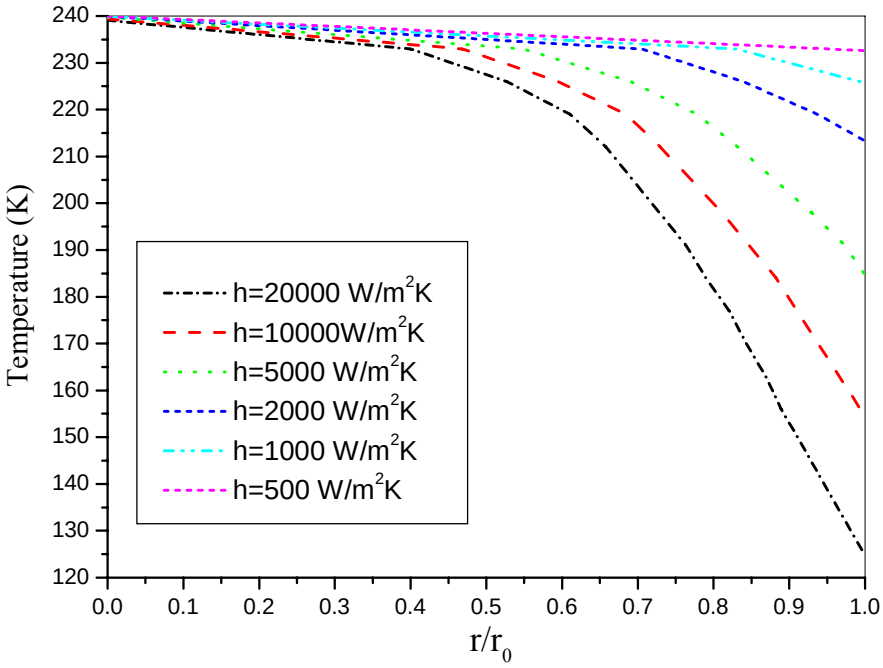

(a)

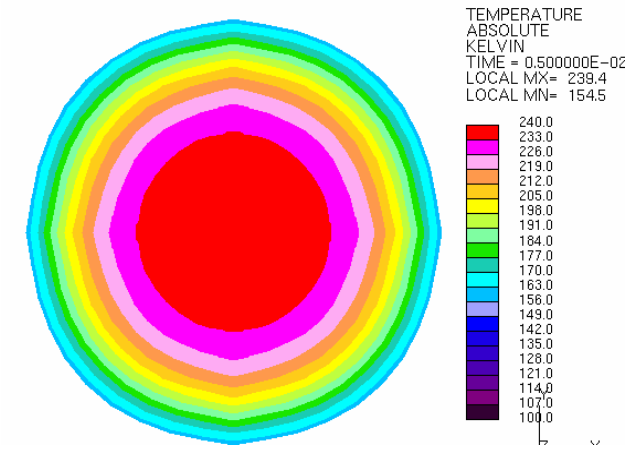

(b)

Fig. 4-3 Temperature distribution along r/r_0 at $\tau = 0.005s$ (a) calculated by equation (4-4) at different heat transfer coefficients. (b) calculated by FULENT at h=10000W/m^{2}K

uniform for $r/r_0>0.82$. When the heat transfer coefficient, *h,* increases to 20,000 W/m^{2}K, the temperature distribution is non-uniform almost for the whole cell. Since the prediction results by FLUENT® software agrees very well with the results from the analytical solution, Eq. (4-4), the FLUENT® software was used to predict the temperature distribution in the cell for a better graphic display. Figure 4-3(b) illustrates the temperature profiles predicted by FLUENT at $t = 0.005\ s$ with h = 10000 W/m^{2}K. It should be noted that the analytical results were based on the 5-term solution of Eq. (4-4). In fact, if $F_o>0.2$, one term solution of Eq. (4-4) is often used to replace its theoretical solution.

Figures 4-4(a) and 4-4(b) illustrate the effect of heat transfer coefficient on the transient temperature and cooling rate at r/r_0=0.5 based on 5-term solution of Eq. (4-4), respectively. As shown in Fig. 4-4(a), the heat transfer coefficient would directly affect the cooling rate and time to pass through the dangerous damage temperature range, *i.e.*, the temperature zone from 200 K to 240 K as shown in Fig. 4-1. When the heat transfer coefficient, *h,* decreases from 20,000 W/m^{2}K, to 1000W/m^{2}K, as shown in Fig. 4-4(a), the time to pass through it would significantly increase from 0.0073 s to 0.051 s. And the cooling rate shown in Fig. 4-4(b) can reach about 335,000 K/min for *h*=20000 W/m^{2}K, but as the heat transfer coefficient is reduced to *h* = 1000 W/m^{2}K, the cooling rate is only about 51,500 K/min. When the heat transfer coefficient, *h,* is less than 500 W/m^{2}K, the cooling rate in the whole freezing process is nearly constant. Comparing with the OPS, the cooling rate is about 20000K/min[20] and this cooling rate can be obtained at the heat transfer coefficient, *h*, is equal to 500 W/m^{2}K. On the other hand, previous investigators [68] proved that oscillating motions result in thermal diffusivity up to 17,900 times higher than those without oscillations

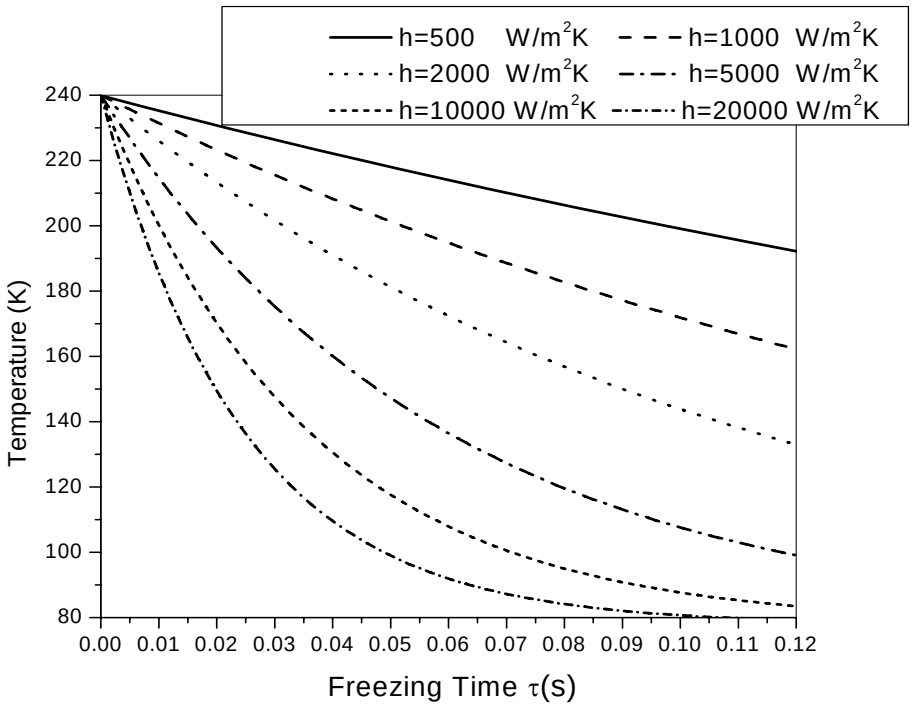

(a)

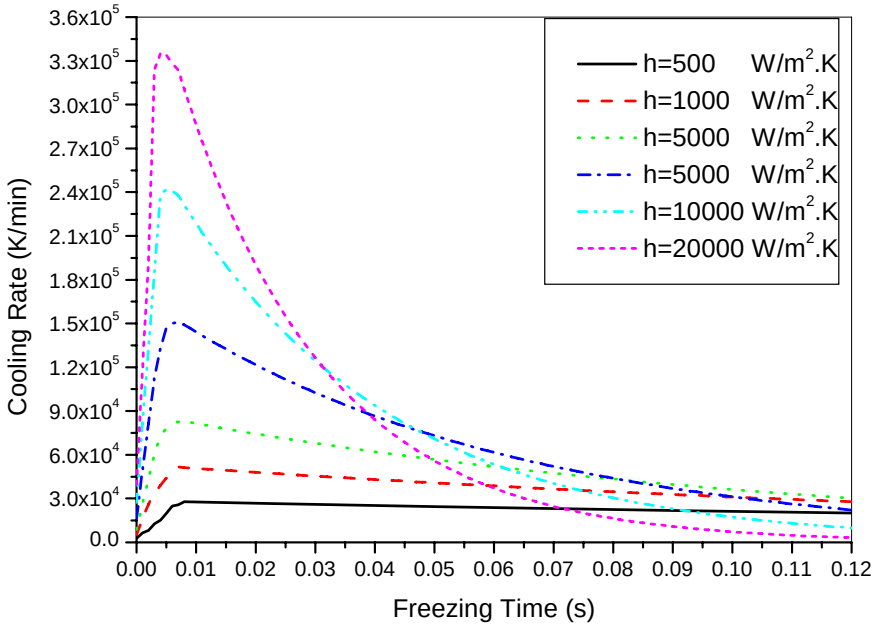

(b)

Fig.4-4 Heat transfer coefficient effect on the cooling characteristics at r/r_0=0.5: (a) temperature distribution; (b) cooling rate

in the capillary tubes. Combined the thin film, microchannel and others novel heat transfer enhancement, the ultra cooling rate (above 200000 K/min) should be available.

Figures 4-5(a) and 4-5(b) illustrate the transient temperature and cooling rate versus the freezing time at the cell center. The transient temperature profile and cooling rate versus the freezing time shown in Fig. 4-5 are similar to those for the case at $r/r_0 = 0.5$. However, the time passing through the DTR is much more, and the highest cooling rate is lower than that at $r/r_0=0.5$ under the same heat transfer coefficient. When the heat transfer coefficient decreases from 20000 W/m^{2}K to 500 W/m^{2}K, the highest obtainable cooling rate changes significantly from 266,000 K/min to 28,200 K/min.

The ultra-fast cooling rate region, as shown in Figs. 4-4 and 4-5, can occur in the DTR if the heat transfer coefficient, h, is higher than 5000 W/m^{2}K. A higher cooling rate can make the cell pass through the DTR in a shorter time, and it will directly improve the cell survival rate. For example, with h = 10,000 W/m^{2}K, the average cooling rate can achieve up to 240,000 K/min at r/r_0 =0.5 and 175,000K/min at the cell center. Combining the previous models [10-12], the critical cooling rate for complete vitrification for most concentrations (45%, 50 glycerol, 30%, 35% L-2,3-butanediol, and 35%-40% 1,2-propanediol) of cryoptectant agents (CPAs) can be readily obtained if the heat transfer coefficient, h, is higher than 5000 W/m^{2}K. Unfortunately, those theoretical analyses depend on relative high concentration CPA which is disadvantage for cell survival rate.

The volume fraction of crystallization, x, has been considered as the most important parameter in the freezing protocol design. Based on the thermophysical properties of 30% L-

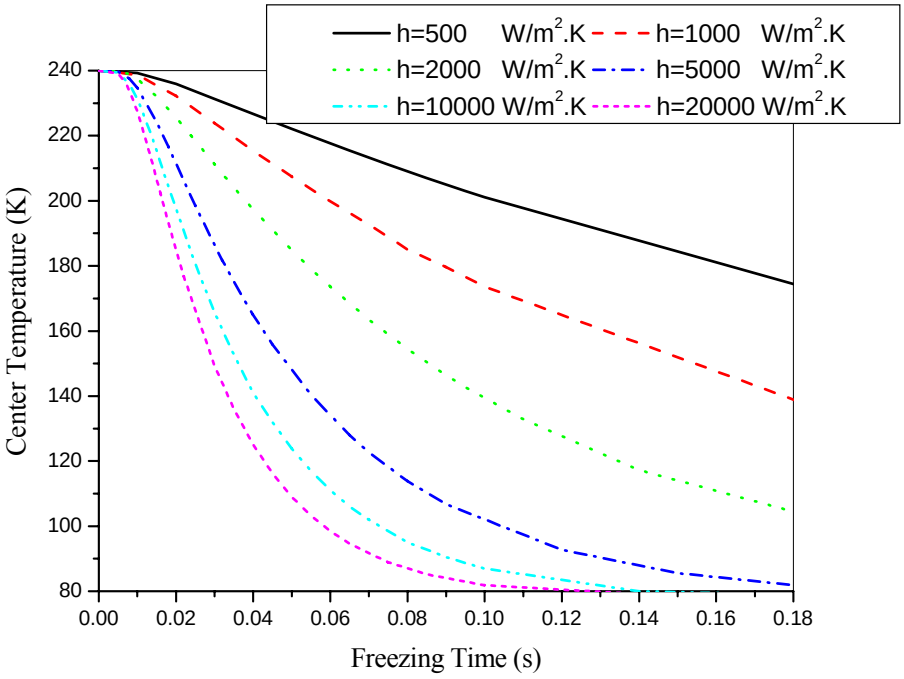

(a)

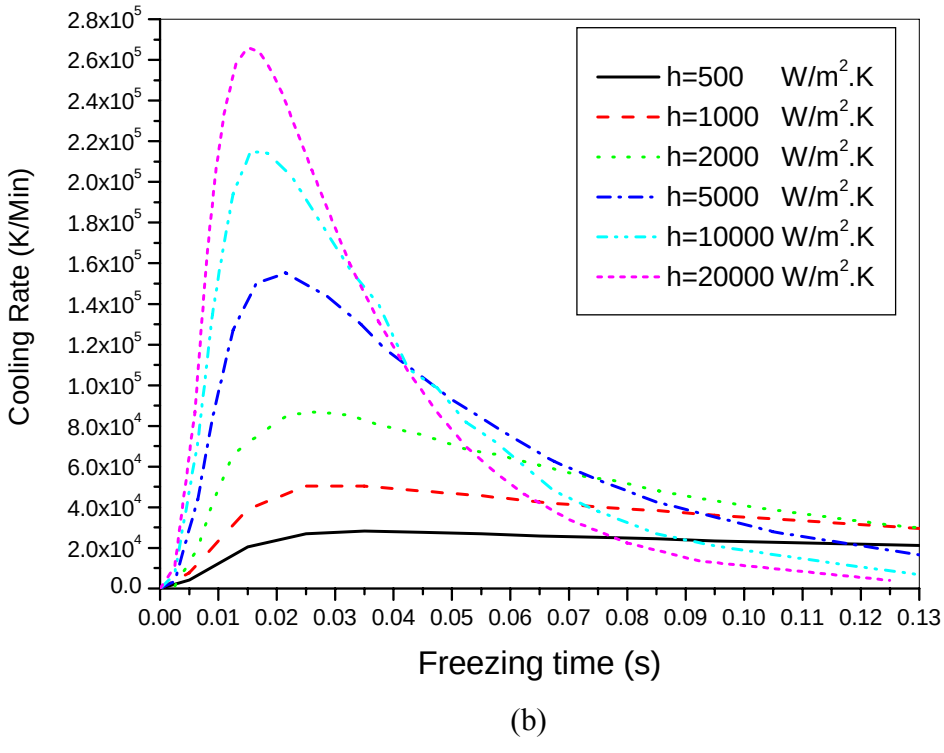

(b)

Fig.4-5 Heat transfer coefficient effect on the cooling characteristics at r/r_0=0.0, (a) temperature distribution; (b) cooling rate

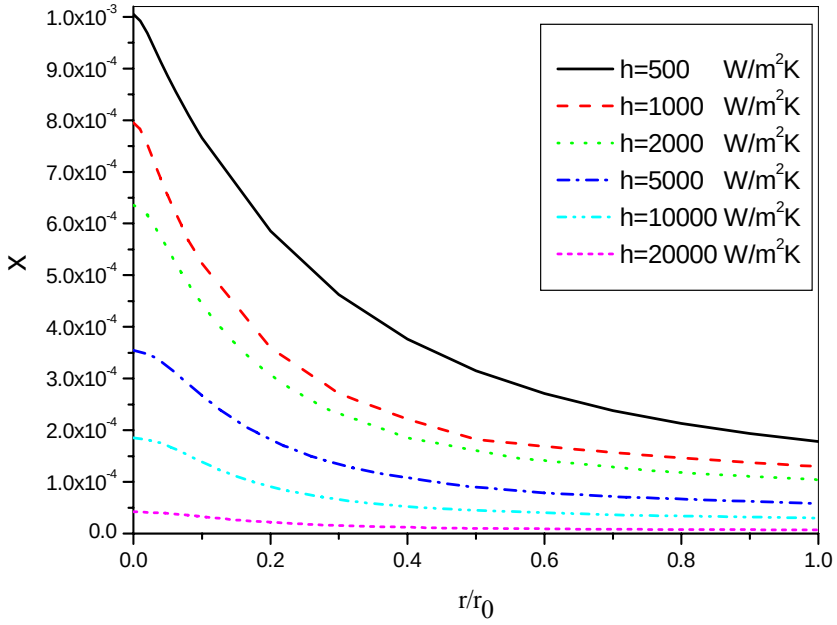

(a)

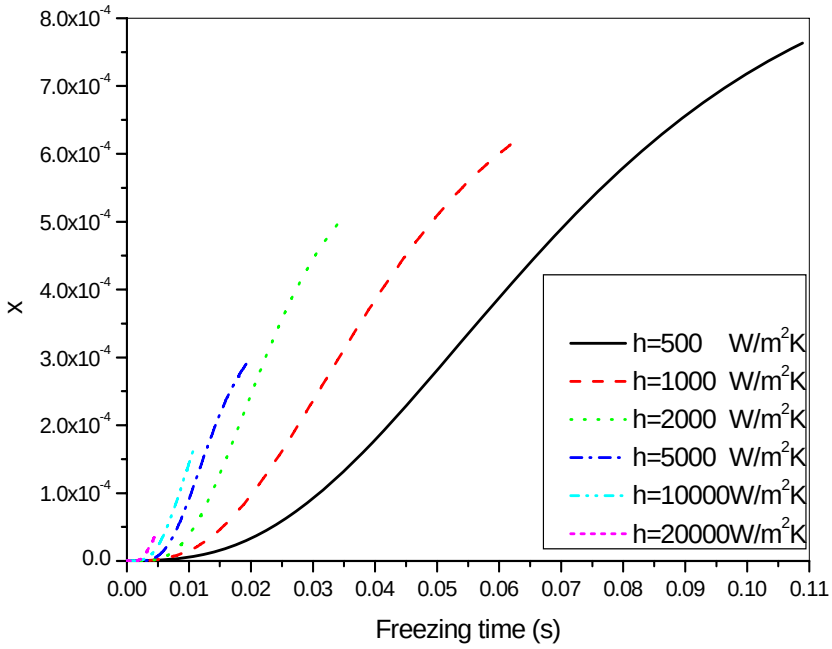

(b)

Fig. 4-6 Effects of different heat transfer coefficients on the volume fraction crystallization *x*. (a) *x* change along *r* direction as the temperature vary from 240K to 200k, (b) *x* value in cell center as the center temperature varies from 200 K to 240 K

2,3-Butanediol cryoprotective solution [48-51, 53](such as Q=20.3Kcal/mol), and the transient temperature profiles predicted by 5-term solution of Eq. (3), the effect of the heat transfer coefficient on the volume fraction of crystallization, *x*, is studied, as shown in Fig. 4-6 (a) and (b). With the different heat transfer coefficient, the volume fraction of crystallization, *x,* along r direction have been conducted as the temperature vary from 240K to 200k. As shown in the Fig.4-6(a), with the heat transfer coefficient increasing, the *x* decrease. The *x* can be predicted at any given location, the Fig. 4-6(b) depicts the results which the $r/r_0 = 0$, namely, cell center. Obviously, the volume fraction of crystallization, x, and the freezing time decrease sharply as the heat transfer coefficient increase keeping the temperature vary from 240K to 200K. The maximum volume fraction of crystallization, x, is 0.000997 and 0.0000439 when the heat transfer coefficient, h, is 500 W/m^{2}K and 20,000 W/m^{2}K, respectively. Therefore, a high heat transfer coefficient can effectively prevent the ice information and take less time to pass through the DTR to abstain the toxic damage to the cells, and as a result, it should directly increase the cell survival rate.

4.5 Experimental Investigation of Cryogenics Oscillating Heat Pipes

As theoretically analyzed in the sections 4.1-4.4, the vitrification with ultra-high cooling rate is the best way to avoid the cell damage by IIF and solution toxic. The numerical analysis results also showed that how to obtain ultra-high cooling rate and uniform cooling temperature field is the key to control the rates *x* of the ice quantity to the maximum crystallizable ice and improve the cell survived ratio. Therefore, how to effectively dissipate

the latent heat reserved in the cryopreservation solutions through a long distance at low temperature surrounding and prevent the nitrogen gas layer formed around the cryopreservation solutions due to big superheat between the solutions and liquid nitrogen is the key in the cell freezing process with ultra-high cooling rate. In fact, in many cryogenic surrounding, effective thermal management between the components to be cooled and cryogenic source always is one of the most serious challenges, too. For example, the most common methods of heat transport in superconducting magnets are the heat conduction by copper. However, with the development of cryocooler-cooled superconducting magnets and large magnets application, where the heat transport distance would be large, the heat conduction by copper will be constrained by its cross section transport capacity [59]. Several types of heat pipe, such as loop heat pipe and oscillation heat pipe, have the abilities to dissipate large heat load with a long distance at low temperature drop, especially, those heat pipes can supply uniform temperature field. However, the cryogenic loop and oscillating heat pipes have not been widely conducted both in theoretical analysis and experimental investigation. Cryogenic heat pipes reported in the literatures can be categorized into four types: thermosyphons [60], wick-based heat pipes [61-63], cryogenic capillary-pumped loops [64] and cryogenic loop heat pipes [59, 65-67]. The results [65-67] showed that the heat transport capacity of the loop heat pipe with liquid nitrogen as working fluid was very low which was only 26W at horizontal direction, especially, its lowest thermal resistance also reached 1.3K/W.

Akachi [68] pioneered a new device called the oscillating heat pipe (OHP), which utilizes the pressure change in volume expansion and contraction during phase change to

excite the oscillation motion of liquid plugs and vapor bubbles between the evaporator and the condenser. Comparing OHP with other conventional heat pipes, the unique feature of OHPs is that there is no wick structure to return the condensate to the evaporator, and therefore there is no countercurrent flow between the liquid and the vapor flow because both of them keep in the same direction. Other features of OHPs including: (1) the driven force mainly depends on the rate of change in pressure with respect with temperature of working fluid $\left(\frac{dp}{dT}\right)_{sat}$ and the temperature difference between the condenser and evaporator. (2) The oscillating motion in the capillary tube significantly enhances forced convection in addition to the phase-change heat transfer, the vapor bubbles and liquid slug formed in capillary tube will effectively produce many thin film surfaces to enhance the phase change heat transfer-both the evaporating and the condensing heat transfer. Because of these unique features, the OHPs have been extensively theoretically analyzed and experimental investigated in the past several years [69].

Recently, the cooling device that combines both the strong oscillating motion in the OHP and the high effective thermal conductivity of nanofluid, which is called the nanofluid oscillating heat pipe, has been developed and experimentally conducted [70]. The nanofluid was consisted of high performance liquid chromatography (HPLC)-grade water and diamond nanoparticles (15nm □ 50nm), which the volume ratio of nanoparticles charged to the heat pipe was 1.0% of the base fluid. Experimental results showed that the nanofluid can significantly enhance the heat transport capability in the OHP [70]. Most of previous investigations of oscillating heat pipe mainly focused on the operation at ambient

temperature and normally the water, acetone was used as its working fluid. In order to better understanding the heat transfer mechanisms and heat transport capacity of cryogenic OHP, one novel oscillating heat pipe with liquid nitrogen as working flow has been developed and experimentally conducted in current investigation.

Figure 4-7 illustrates the test section, including the schematic of OHP and a photograph of 8-turns closed-loop OHP prototype, which has developed and manufactured since the closed-loop OHP has better heat transfer performance [71, 72] than that of open loop. For closed-loop OHP, there exists two moving modes for working flow: (a) oscillating flow only create between the evaporator and the condenser; (b) flow along single-direction moving as shown in Fig. 4-7 (b). The OHP was fabricated from alloy 122 copper tubing with an inner diameter of 1.65 mm and an outer diameter of 3.18 mm, which can work very well at $213\,atm$ pressure with $T = 37.8^0 C$ and satisfy with the pressure change of cryogenic working fluid at different temperature condition. In the design of OHP, the inner diameter must be small enough so that the surface tension forces dominate gravitational forces and distinct vapor bubbles and liquid slug can form. The theoretical maximum interior diameter for a capillary tube occurs when the square of the Bond number is less than 4, which can be expressed that the maximum diameter is $D_{crit} \le 2\sqrt{\dfrac{\sigma}{g(\rho_l - \rho_v)}}$, where σ is the surface tension, ρ_l is the liquid density, ρ_v is the vapor density, and g is the gravitational acceleration. Based on this equation, the copper tubing inner diameter for the current study is well within this constraint. For the working fluid of OHP selection at saturated conditions, a

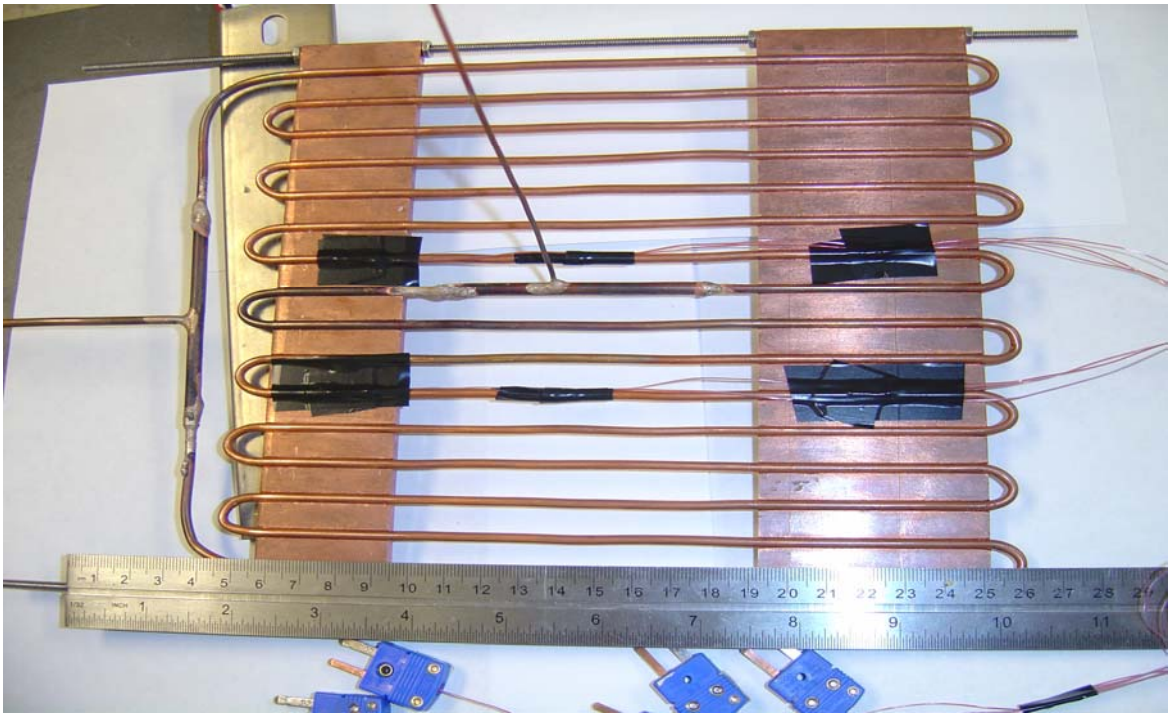

(a) OHP photograph and thermocouples location

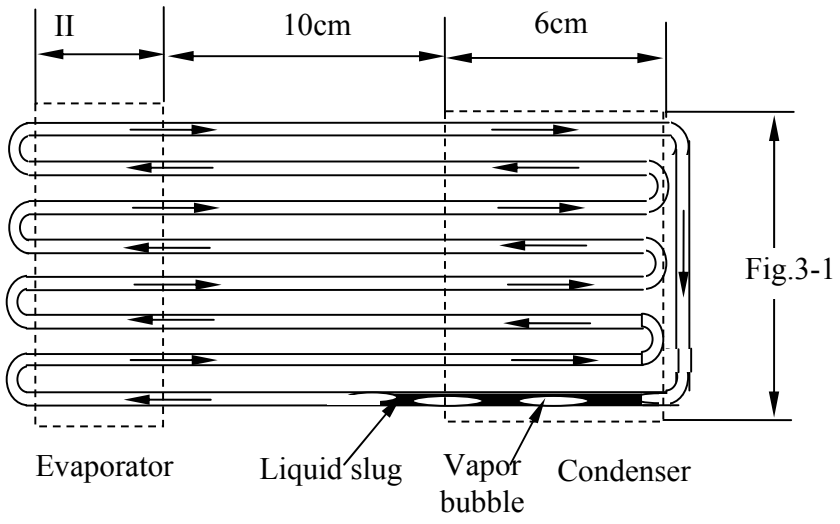

(b) Schematic of OHP operation and dimensions

Figure 4-7 Test section (OHP)

high value of surface tension σ and $\left(\frac{dp}{dT}\right)_{sat}$ to create high enough driven force at given temperature difference between evaporator and condenser will be desirable; on the other hand, a low dynamic viscosity to reduce the shear stress along the wall resulting in a low pressure drop in the channel is also desirable. The working fluid of cryogenic OHP in the current investigation was the liquid nitrogen. The photograph of test section (cryogenic OHP) was displayed in Fig. 4-7(a). The dimensions of the evaporator, where a uniform heat flux was added, were 40×185 mm^2. In order to improve the heat transfer from the heater to the evaporating section, a 40×185×5-mm^3 copper plate was used. The semicircular grooves machined on the plate created a good fit with the tubing for better heat transfer. The dimensions of the condenser were also 60×185 mm^2 and it was fashioned in the same manner as evaporator. The distance between the evaporator and the condenser is 100 mm.

Figure 4-8 (a) displays the schematic experimental system, which consists of test section (OHP), data acquisition system, heat input and measurement system, liquid nitrogen pool, and liquid nitrogen tank. The cryogenic OHP (test section) except the bottom surface of condenser was completely covered by a thick foamed layer, as shown in Fig.4-8 (a), the bottom surface of condenser copper block was directly exposed in the liquid nitrogen pool. Data acquisition system included Type-*T* thermocouples, an IOtech DAQ/56 USB data acquisition system and personal computer to record the temperature response. The heat input and measurement system composed of a heater, its power supplied by a Staco 3PN501B voltage regulator, and the voltage was measured by a Fluke 45 dual display multimeter (DMM). The electronic resistance (R) of heater was measured by multimeter at liquid

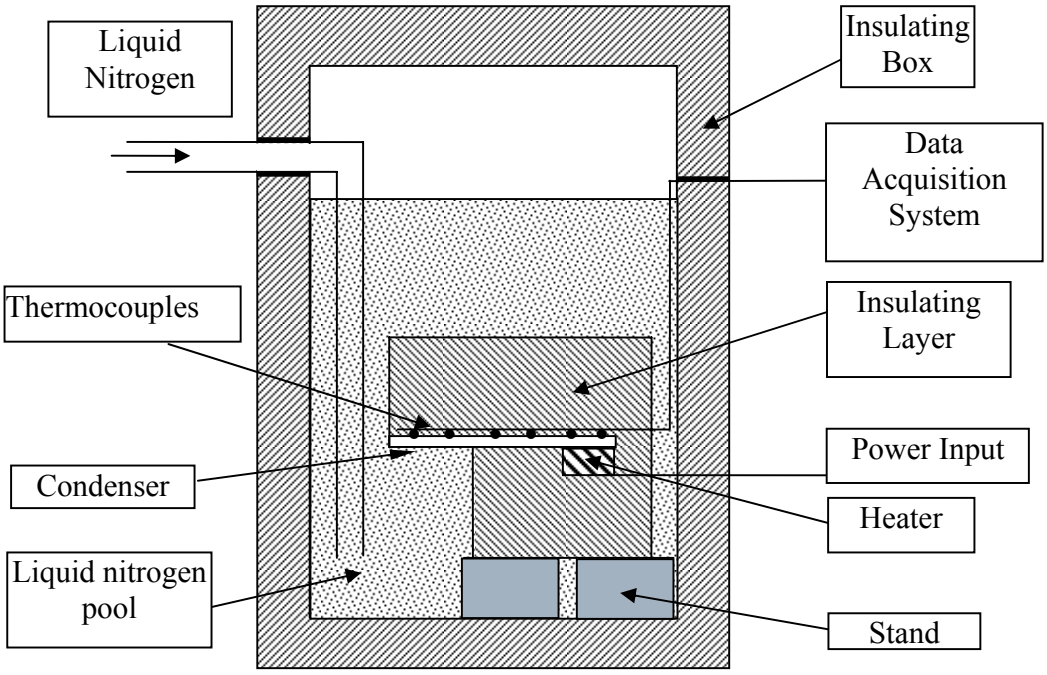

(a)

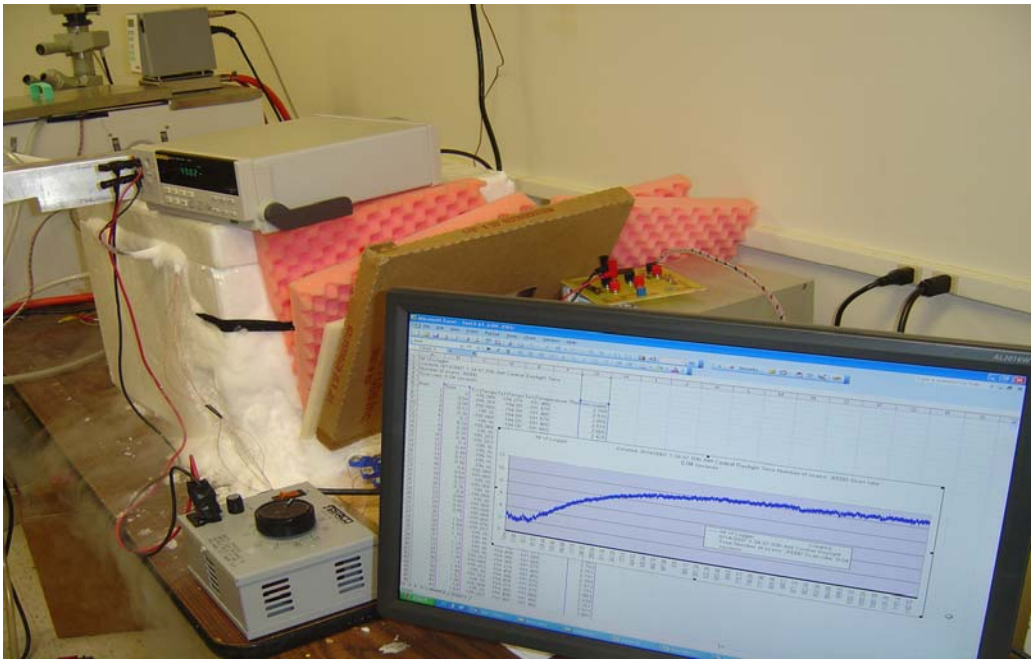

(b)

Figure 4-8 Experimental system (a)schematic (b) photo of the system operating

nitrogen temperature since the resistance of the heater depends on the temperature [39]. The heat load was calculated by: $P = \frac{U^2}{R}$, where, U was measured by multimeter (output value of voltage regulator) and R was the electronic resistance of heater. In the current investigation, the liquid nitrogen pool was an insulating box, which connected with a liquid nitrogen Dewar (its pressure is around 1.5 bar) by a soft hose. Figure 4-8 (b) displays the experimental system was running and the data acquisition system was recording the experimental data simultaneously.

Before the start of experiment, the experimental system should be pre-cooled till the test section reached the liquid saturated temperature since there is no any heat load input. As displayed in Fig.4-7 (a), there are two tubes in the OHP, one of them is the charge tube which will directly immerges into the liquid nitrogen pool and another one is the connection tube which will connect with vacuum pump. In the pre-cool process, the insulated test section was immerged into liquid nitrogen while the vacuum pump turned on simultaneously, therefore, the liquid nitrogen can be charged into the heat pipe. The charge tube and the connection tube will be hammered after the heat pipe was charged enough. The charge ratio is calculated by the weight difference after the experiments. After pre-cool, charge process was done till steady-state condition was reached; the heat load was added to the evaporator by heater. When the desired steady state reached at a given heat load, the power was incremented and the operation of OHP was allowed to reach the next equilibrium condition. During the tests, the thermal power input and the temperature data were simultaneously recorded using the IOtech DAQ/56 data acquisition system controlled by a personal computer.

The performance of cryogenic OHP with liquid nitrogen as working fluid and charge ratio was 0.48 has been illustrated in Fig. 4-9. Figure 4-9(a) recorded the temperature response of the evaporator and the condenser when the heat load added to the evaporator changed from 20.5W to 380.1W. The data acquisition frequency was 1Hz, for any given heat load, the OHP operation was recorded at least 21.7 minutes. As shown in Fig.4-9 (a), the temperature in evaporator changed from the liquid nitrogen saturation temperature (-195.8^{0}C) to -136.8^{0}C while the condenser temperature changed from liquid nitrogen saturation temperature to -185.6^{0}C when the heat load input changed from 20.5W to 380.1W. In order to show clearly the temperature response when the heat load increment added to evaporator, Figure 4-9 (b) illustrated the evaporator temperature response when heat load changed from 68.8W to 86.7W, then 125.7W. Obviously, an increment heat load was added, the OPH operation changed from steady state to unsteady state till a new steady state, as shown in Fig. 4-9 (b), the process can be divided into three regions: (I) unsteady state (around 12 minutes), where the evaporator temperature is increasing, (II) transient state (about 4 minutes) ,where the temperature of the evaporator and the condenser is unsteady and keep the same isochronous pace, and (III) steady state, where the temperature of the evaporator and condenser keep constant. In order to further confirm the temperature response of the evaporator and the condenser keep the same pace when the heat pipe work at the region II, the temperature response in the evaporator and the condenser has been illustrated in Figure 4-10 when the time changed from 6000s to 6400s. As shown in Fig. 4-10, the temperature responses in the evaporator and the condenser keep the same frequency, however, the

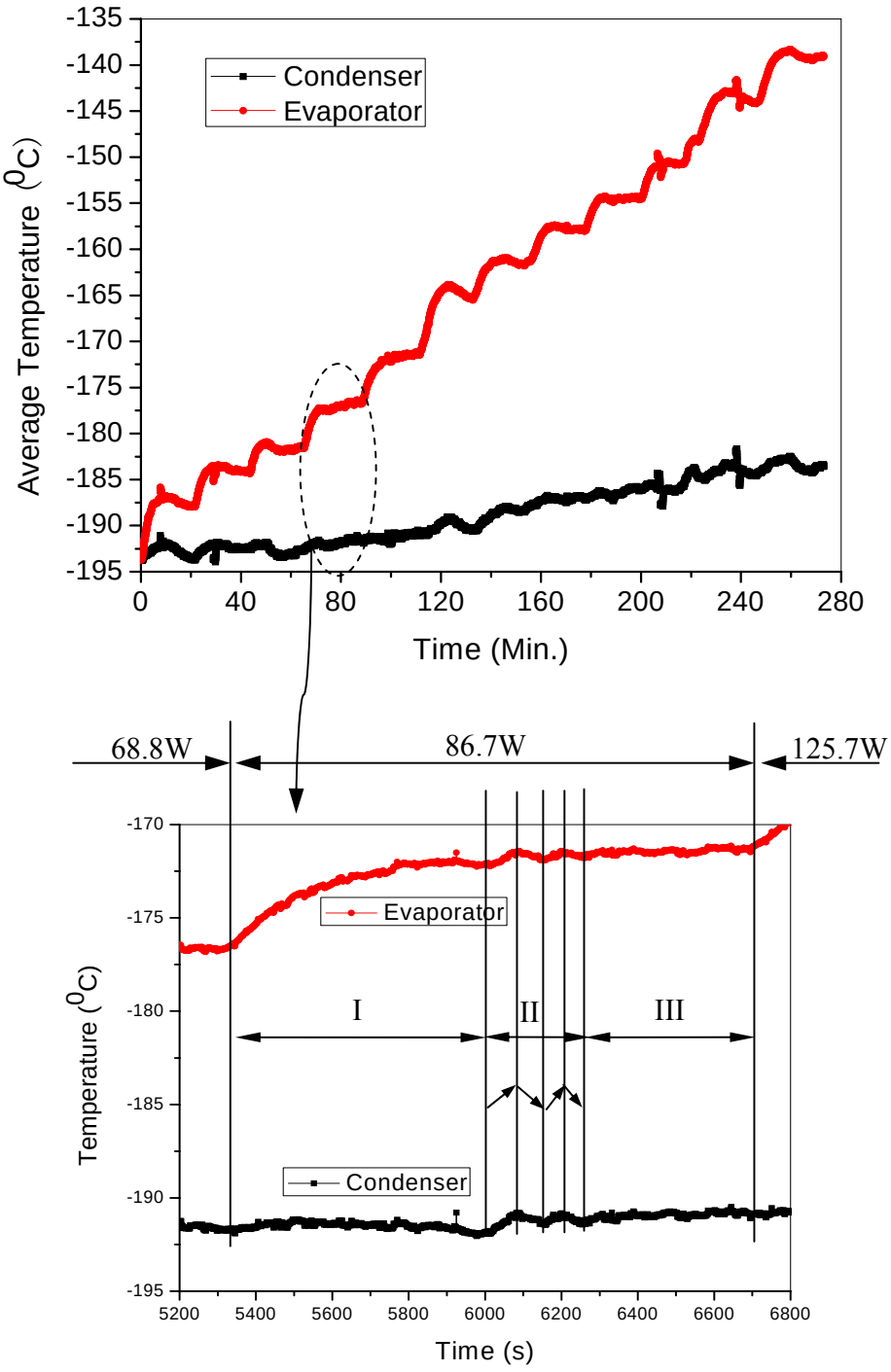

(b) Heat load 86.7W (I) unsteady state (II) transient state (III) new steady state

Figure 4-9 Temperature responses in the evaporator and the condenser versus heat load

amplitudes of the temperature in evaporator is smaller than that of condenser.

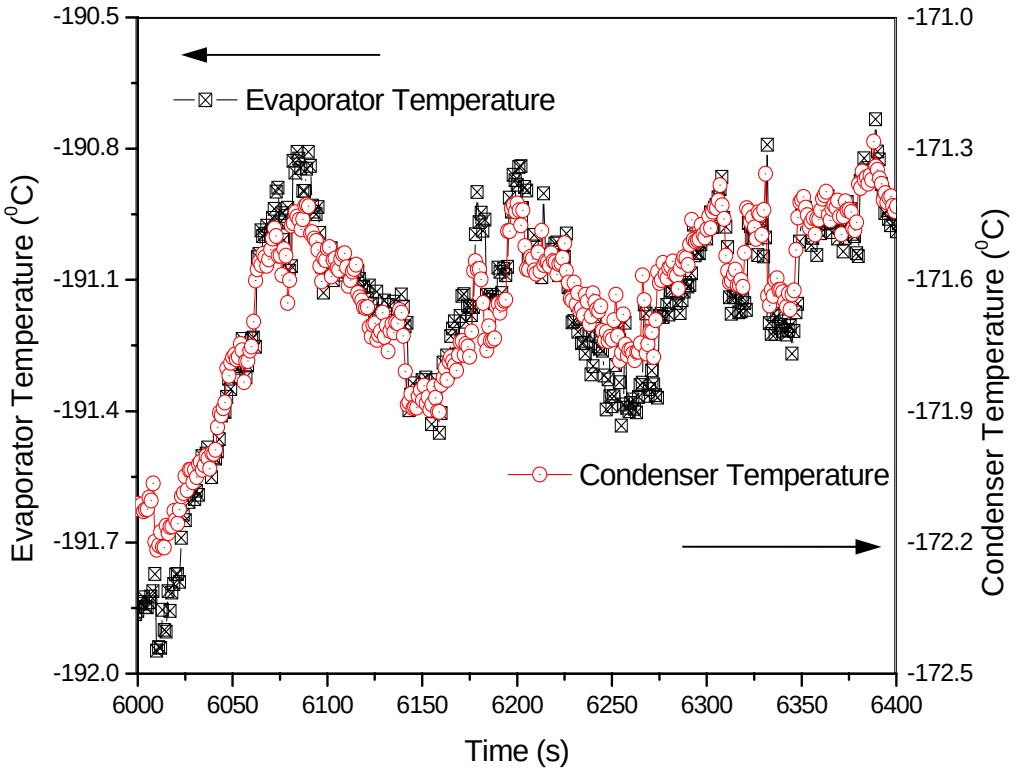

Figure 4-10 Temperature response in the evaporator and condenser reach steady state at $Q = 86.7\text{W}$

The temperature differences between the evaporator and the condenser as well as the average temperature differences at steady state have been displayed in the Fig. 4-11. When the heat load increment was added, the temperature difference changed from unsteady state to steady state and reached new equilibrium state within 12 minutes for any heat load. As shown in Figure 4-11(a), there is several temperature differences change sharply in the transient state (region II) and maybe the working flow move along the single-direction created in those regions. The average temperature difference between the evaporator and the

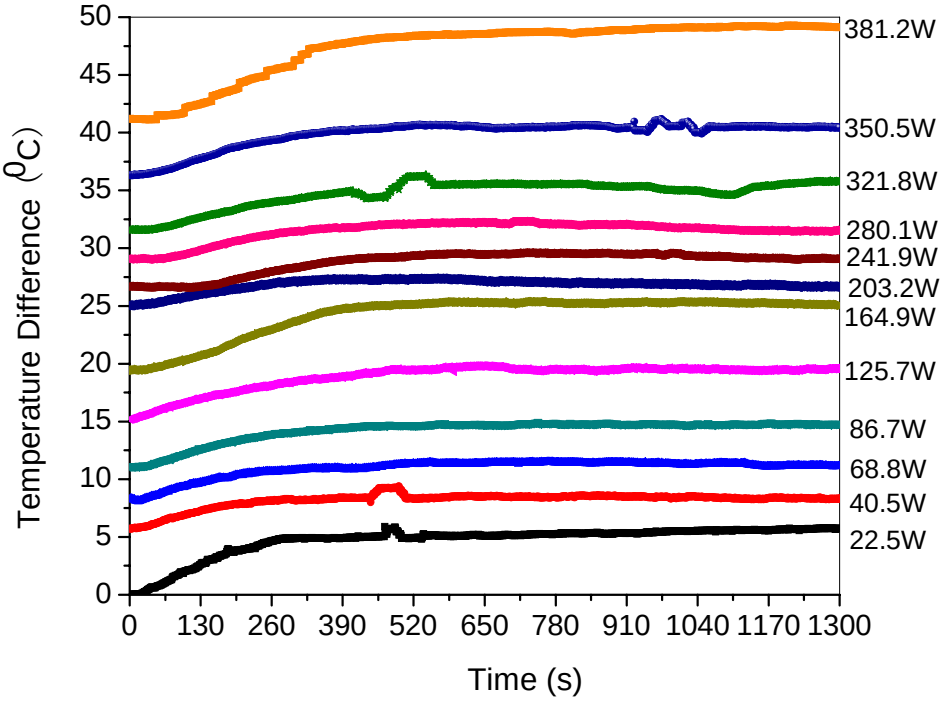

(a) Temperature difference versus heat load input

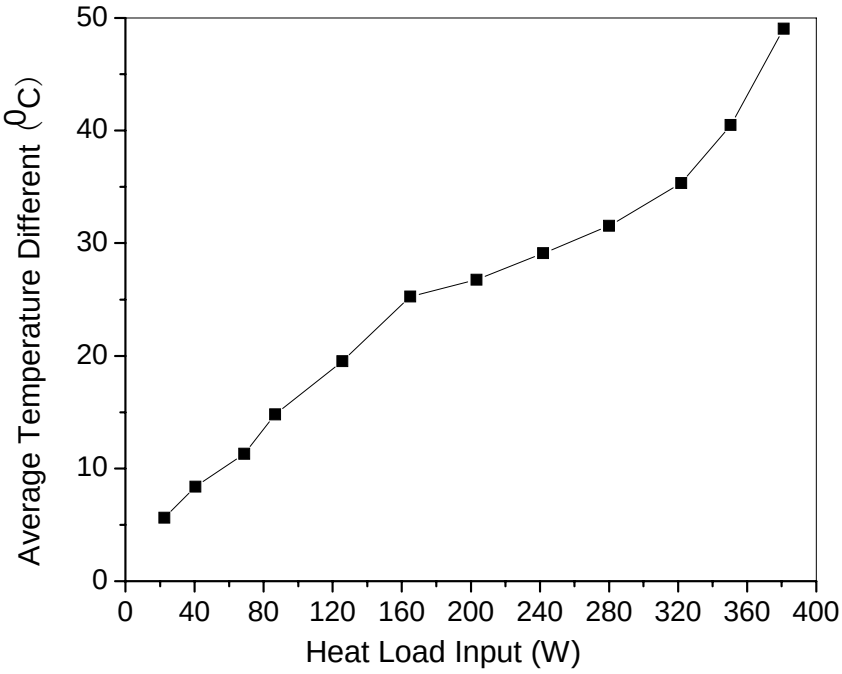

(b) Average temperature difference versus heat load input at steady state

Figure 4-11 performance of cryogenic OHP with liquid nitrogen as working fluid

condenser when the OHP operated at steady state (after 12 minutes) has been calculated and shown in Fig. 4-11(b). The average temperature difference varied linearly to the heat load input when the heat load was less than 160W, and the average temperature difference was higher than 25^0C when the heat load reached 160W. When the heat load continued increasing, the average temperature difference increased very low, for example, the heat load changed from 164.9W to 280.1W (the heat load increment was 115.2W) while the average temperature difference only increased 6.25^0C. Similarly, the average temperature difference increased 17.5^0C when the heat load changed from 280.1W to 381.2W (the heat load increment was 101.1W). Therefore, the OHP work at low heat load, the performance is

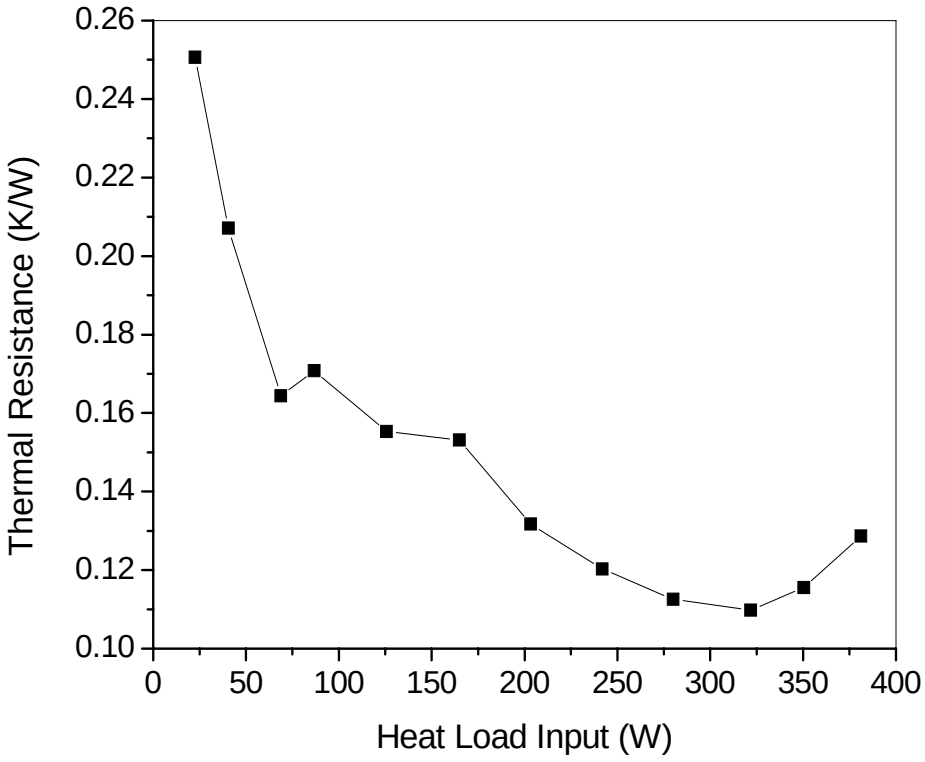

Figure 4-12 average thermal resistance versus heat load input at steady state

poorer than that work at high heat load. The effective thermal resistance was defined as $R = \frac{\Delta T_{ave}}{Q}$ herein and illustrated in the Figure 4-12. As shown in Fig. 4-12, the effective thermal resistance decreases with the heat load input when the heat load was less than 325W, however, the effective resistance will increase with the heat load continue increasing. For example, the effective thermal resistances are 0.25K/W and 0.11K/W for $Q = 22.5\text{W}, 321.8\text{W}$, respectively.

The heat load effect on the amplitude of temperature difference has been displayed in Figure 4-13 (a), (b), and (c). As shown in Fig.4-13, the amplitude of the temperature difference decreases with the heat load increasing. The sample standard derivation (*S*) is the unique parameter to evaluate the spread of the temperature difference [73, 74], namely, the value of *S* can be used to stand for the amplitudes temperature difference. The *S* can be expressed as: $S = \sqrt{\frac{1}{N-1}\sum_{i=1}^{N}\left(T_i - \overline{T}\right)^2}$, and the values, *S*, of Figure 4-13(a), (b) and (c), are 0.387, 0.313, and 0.025 while the heat load was equal to 40.5W, 203W, and 350.5W, respectively. When the higher heat load is added to the evaporator, the higher temperature difference will occur between the evaporator and condenser resulting in big drive force to create higher frequency oscillating flow in the OHP. Higher frequency oscillating flow is equivalent to the higher flow velocity, which result in the high convection heat transfer coefficient while it takes a shorter time to pass through the evaporator and condenser section. Thus, the amplitude of the temperature difference goes down with the heat load increase.

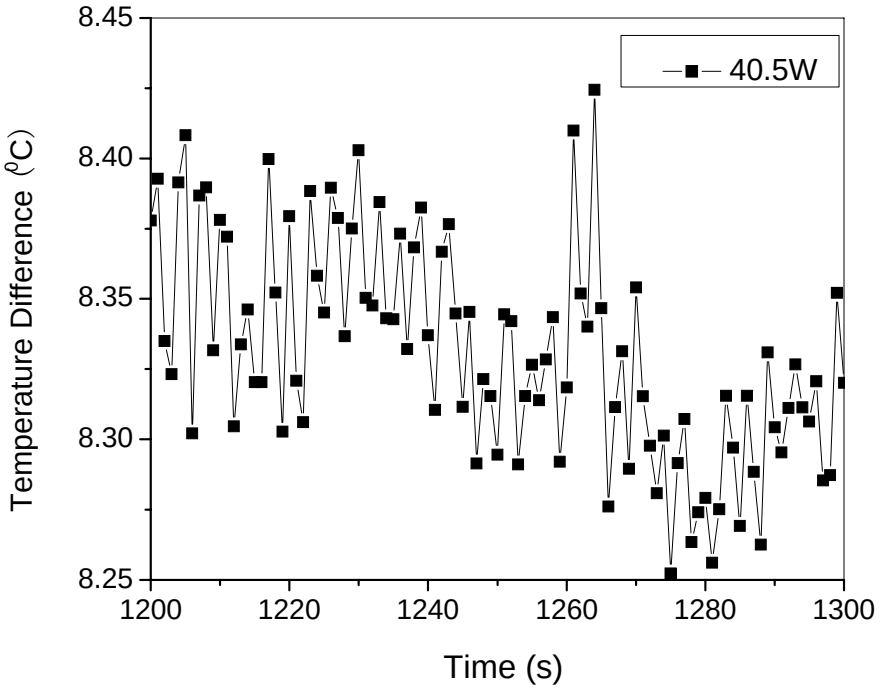
8.45
8.40
8.35
8.30
8.25
Temperature Difference (°C)
40.5W
1200
1220
1240
1260
1280
1300
Time (s)

(a)

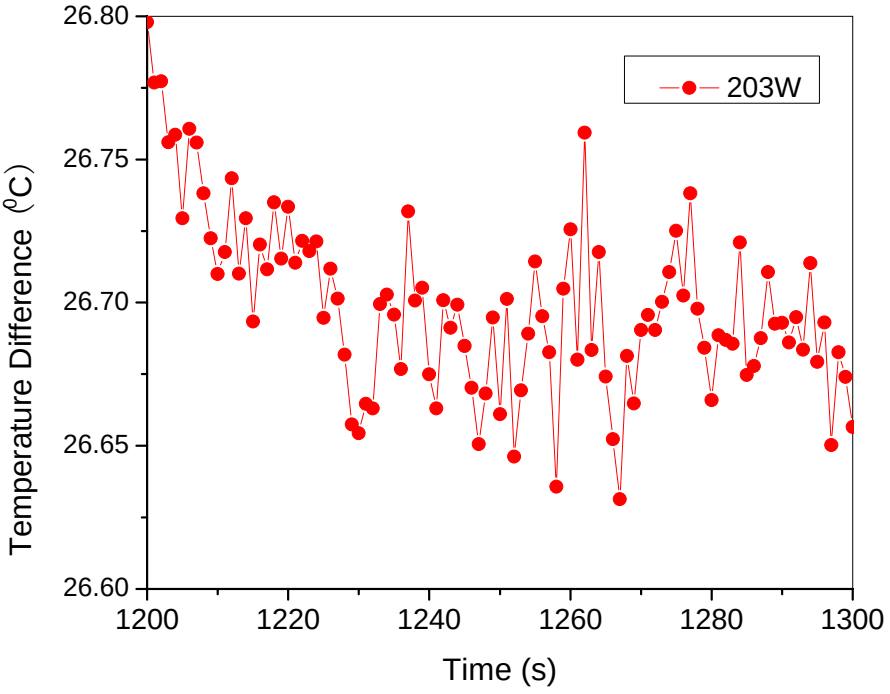
26.80
26.75
26.70
26.65
26.60
Temperature Difference (°C)
203W
1200
1220
1240
1260
1280
1300
Time (s)

(b)

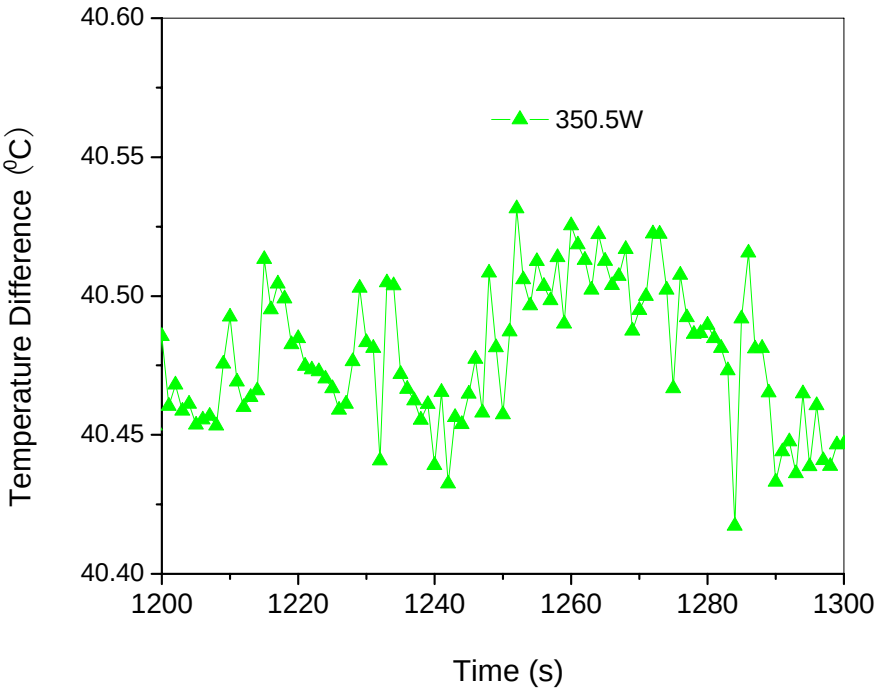

(c)

Figure 4-13 Heat load effect on the amplitude of temperature difference at steady state

4.6 Chapter Summary

A transient heat transfer model predicting the transient temperature distribution with thin film evaporation heat transfer in a cell during the cyropreservation process is developed. The model considers the effects of the heat transfer coefficient on the temperature distribution and cooling rate during the freezing process since the heat transfer coefficient depend on the location of thin film region. The prediction demonstrates that the ultra-high cooling rate can occur in the DTR if the heat transfer coefficient is higher than 5000 W/m^2K for the current investigation. The analytical results show that the heat transfer coefficient significantly affects the volume fraction of crystallization, x, and as the heat transfer coefficient, h,

increases, the volume fraction of crystallization and the freezing time decrease sharply. The current investigation will result in a better understanding of the transient heat transfer characteristics and intracellular ice formation under different heat transfer coefficient in cells during the cryopreservation process.

The numerical analysis results showed that how to obtain ultra-high cooling rate and uniform cooling temperature field is the key to control the rates x of the ice quantity to the maximum crystallizable ice and improve the cell survived ratio. Therefore, how to effectively dissipate the latent heat reserved in the cryopreservation solutions through a long distance at low temperature surrounding and prevent the formation of the nitrogen gas layer around the cryopreservation solutions to create ultra-high cooling rate play a very important role in the cell freezing process with ultra-high cooling rate. In order to obtain an ultra-high cooling rate with uniform temperature distribution, one novel device called cryogenic liquid nitrogen oscillating heat pipe has been developed and experimentally conducted. At horizontal direction, experimental results show that the maximum heat transport capability of the OHP reached 380W with average temperature difference only 49K between the evaporator and the condenser when the cryogenic OHP was charged with liquid nitrogen at 48 percent. The thermal resistance decrease from 0.256 to 0.112 while the heat load increase from 22.5W to 321.8W. When an increment heat load was added to it, the OHP operation changed from steady state to unsteady state till a new steady state reached, the process can be divided into three regions: (I) unsteady state (II) transient state, and (III) new steady state. The temperature response keeps the same frequency both in the evaporator and the condenser when the OHP operated at steady state, but the amplitude of temperature change in the

evaporator is smaller than that of the condenser. The experimental results also show that the amplitude of temperature difference between the evaporator and the condenser decrease when the heat load increase due to the flow velocity rise up.

.

CHAPTER 5 CONCLUSIONS

With the technology development of VLSI circuits, high performance and compact design of microelectronic elements accompany high power consumption and high heat fluxes generation. Effective thermal management in those systems has been, and will continue to be one of the most critical issues to be resolved in order to maintain and keep their peak performance. However, conventional cooling methods such as the conventional heat sinks are of impractical function at such high heat fluxes due to the constraints in the low thermal conductivity, volume. The heat pipe, as the most efficient system known today among the many different types of heat transport systems, makes it become into the peerless choice in the electronics cooling field. In order to better understanding the heat transfer mechanisms of the heat pipe, the heat transfer model including the thin film evaporating heat transfer, different surfaces effect on the thin film profiles, contact angle effect on the maximum heat transport capacity, disjoining pressure, have been developed. The prototypes of groove heat pipe with micro trapezoid wicks, miniature loop heat pipe, flat heat pipe, have been manufactured and experimental investigated. For the groove heat pipe: the experimental data has been compared with the theoretical predictions and they are in good agreement each other. The results also show that the temperature drop in the evaporator is much larger than that in the condenser at any given load. Obviously, it is more important to further decrease the temperature drop in the evaporator in order to enhance the heat transport capability in a grooved heat pipe. With the heat load increase, the new thin film evaporating region formed in CASE II and the thermal resistance reach its minimum. The results also show that the contact angle play important rule in the thin film evaporating heat transfer region.

For miniature FHP and LHP, one theoretical model for the thin film evaporating heat transfer on curved surface was developed. The effects of gravitational force and contact angle on the thin film profiles and heat flux distribution on the curved surface are investigated. The theoretical results show that the gravity effect on thin film distributions and heat flux profiles on curved surfaces cannot be neglected. The results also indicate that while the thin-film-evaporation region on the curved surface is smaller than that on a flat surface. Based on the capillary limit and thermal resistance, the maximum heat transport capacity of the heat pipes is predicted. In order to confirm the theoretical predictions, prototypes of miniature FHP with wire core groove and LHP with flat sintered copper particles evaporator have been manufactured and experimentally investigated. For miniature FHP, when the heat pipes were operated at the Case II where a new thin film region form on flat surface, the heat load reached its maximum transport capacity. The further increase of heat load would result in the sharp increase of the temperature drop due to the heat transfer degradation in thin film evaporation although the heat pipe has not reached the capillary limit. For miniature LHP, the experimental results show that the LHP investigated herein can remove a heat load 230 W with a heat flux up to 75 W/cm^2. The theoretical prediction of the temperature responses of evaporator and condenser agrees well with the experimental results, however, the model cannot be used to predict the temperature response of evaporator at high heat flux.

A transient heat transfer model predicting the transient temperature distribution with thin film evaporation heat transfer in a cell during the cyropreservation process is developed. The prediction demonstrates that the ultra-high cooling rate can occur in the DTR if the heat transfer coefficient is higher than 5000 W/m^2K for the current investigation. The analytical

results show that the heat transfer coefficient significantly affects the volume fraction of crystallization, x, and as the heat transfer coefficient, h, increases, the volume fraction of crystallization and the freezing time decrease sharply. In order to obtain ultra-high cooling rate and uniform cooling temperature field and control the rates x of the ice quantity to the maximum crystallizable ice and improve the cell survived ratio, one novel device called cryogenic liquid nitrogen oscillating heat pipe has been developed and experimentally conducted. Experimental results show that when the cryogenic OHP is charged with liquid nitrogen at 48 percent, heat transport capability reached 380W with average temperature difference 49^0C between the evaporator and condenser. At steady state, the amplitude of temperature response in evaporator is smaller than that of condenser while the temperature response keeps the same frequency both in evaporator and condenser. The experimental results also show that the amplitude of temperature difference between evaporator and condenser decrease while the heat load increase.

REFERENCES

[1] Wang E.N., Zhang L., Jiang L.N., Koo J.M., Maveety J.G., et al., 2004, "Micromachined Jets for Liquid Impingement Cooling of VLSI Chips," Journal of Microelectromechanical System, Vol. 13, pp. 833-842.

[2] Peterson G.P., Ma H.B., 1996, "Theoretical analysis of the maximum heat transport in triangular grooves: a study of idealized micro heat pipes," Journal of heat transfer Vol. 118, pp. 731-739.

[3] Ma H.B., Peterson G.P., 1996, "Experimental investigation of the maximum heat transport in triangular grooves," Journal of Heat Transfer, Vol. 118, pp.740-745.

[4] Ma, H.B., Peterson, G.P., 1997, "Temperature Variation and Heat Transfer in Triangular Grooves with an Evaporating Film," AIAA Journal of Thermophysics and Heat Transfer, Vol. 11, pp. 90-97.

[5] Jiao A. J., Ma H. B., and Critser J. K., 2007, "Investigation of the Evaporation Heat Transfer in Miniature Flat Heat Pipe with Wire Core Groove," Journal of Heat Transfer, (will be published in May, 2008).

[6] Jiao, A.J., Ma, H.B., and Critser J. K., 2007, "Evaporation Heat Transfer Characteristics of tube Heat Pipes with Micro Trapezoidal Structure Liquid Wicks" International Journal of Heat and Mass Transfer, Vol.50(15-16), pp. 2905-2911.

[7] D.B Tuckerman, R.FW Pease, 1981, "High-performance heat sinking for VLSI," IEEE Electron Device Letter, Vol.EDL-2, pp.126-129.

[8] Babin B.R., Peterson G.P., and Wu D., 1990, "Steady state modeling and testing of a micro heat pipe," ASME Journal of Heat Transfer, 112, pp.595-601.

[9] Peterson G.P., Ma H.B., 1999, "Temperature response of heat transport in micro heat pipe," Journal of Heat Transfer, Vol.121, pp.438-445.

[10] Ha J.M., Peterson G.P., 1994, "Analytical prediction of the axial dryout point for evaporating liquids in triangular microgrooves." Journal of Heat Transfer. Vol.116, pp. 498-503.

[11] Khrustalev D., Faghri A., 1994, "Thermal Analysis of a Micro Heat pipe," Journal of Heat Transfer. Vol. 116, pp.189-198.

[12] Faghri A., 1995, Heat Pipe Science and Technology, Taylor & Francis, Washington.

[13] Peterson GP., 1994, An Introduction to Heat Pipes-Modeling, Testing, and Applications, John Wiley & Sons, New York.

[14] Hanlon M.A., Ma H.B., 2003, "Evaporation heat transfer in sintered porous media", Journal of Heat Transfer, Vol.125, pp. 644-652.

[15] Jiao A.J., Riegler R., Ma, H.B., Peterson G.P., 2005, "Thin Film Evaporation Effect on Heat Transport Capability in a Groove Heat pipe," Microfluidics and Nanofluidics, Vol. 1, pp. 227-233.

[16] Cotter T.P., 1984, "Principle and prospects of micro heat pipes," Proc. 5th International Heat pipe Conference, Tsukuba, Japan, pp.328-335.

[17] Demsky S.M., Ma, H.B., 2004, "Thin Film Evaporation on a Curved Surface" Microscale Thermophysical Engineering, Vol. 8, No. 3, pp. 285-299.

[18] Holm F.W., and Goplen S.P., "Heat transfer in the meniscus thin film transition region," ASME Journal of Heat Transfer, 101 (1979) 543-547.

[19] GS Hwang, M. Kaviany, WG Anderson, J Zuo, 2007, "Modulated wick heat pipe,"

International Journal of Heat and Mass Transfer, Vol.50, pp.1420-1434.

[20] PD Dunn, DA Reay, 1978, Heat pipes 2nd edition, Pergamon, Elmsford, New York.

[21] Y., Kamotani, "Evaporator film coefficients of grooved heat pipe," in: Proceeding of the 3rd International heat Pipe Conference, Stanford Press, Palo Alto, CA, 1978, pp. 128-130.

[22] P.C. Wayner, 1994, "Thermal and mechanical effects in the spreading of a liquid film due to a change in the apparent finite contact angle," ASME Journal of Heat Transfer, Vol.117, pp.938-945.

[23] Y. Cao, A. Faghri, 1994, "Analytical solutions of flow and heat transfer in a porous structure with partial heating and evaporation on the upper surface," International Journal of Heat and Mass transfer Vol.37, pp.1525-1533.

[24] X.Xu, Y.P. Carey, 1990, "Film evaporation from a micro-grooved surface-an approximate heat transfer model and its comparison with experimental data," Journal of Thermophysics and Heat Transfer, Vol.4, pp. 512-520.

[25] Wayner PC, Kao YK, LaCroix LV, 1976, "the Interline Heat Transfer Coefficient of An Evaporating Wetting Film," International Journal of Heat and Mass Transfer, Vol. 19, No. 3, pp. 487-492.

[26] Kim S.J., Seo, J.K., Do, K.H., 2003, "Analytical and experimental investigation on the operational characteristics and the thermal optimization of a miniature heat pipe with a grooved wick structure," International Journal of Heat and Mass Transfer, Vol. 46, pp. 2051-2063.

[27] Hopkins R, Faghri A, Khrustalev D, 1999, "Flat Miniature Heat Pipes with Micro

Capillary Grooves," ASME Journal of Heat Transfer, Vol. 121, pp.102-109.

[28] Stephan, P.C., Busse, C.A., 1993, "Analysis of the Heat Transfer Coefficient of Grooved Heat Pipe Evaporator Walls," International Journal of Heat and Mass Transfer, Vol.35, No.2, pp.383-391.

[29] Chato, J.C., 1962, "Laminar Condensation Inside Horizontal and Inclined Tubes," J. ASHRAE, Vol. 4, pp 52.

[30] B Horacek, KT Kiger, JH Kim, 2005, "Single nozzle spary cooling heqat transfer mechanisms," International Journal of Heat and Mass Transfer, Vol. 48, pp.1425-1438.

[31] Kopchikov I.A., Veronim G.I., Kolach T,A., Labuntsov D.A., and Lebedev P.D., 1969, "Liquid boiling in a thin film," International Journal of Heat and Mass Transfer, Vol.12, pp.791-896.

[32] Maydanik Y. F., 2005, "Review of Loop Heat Pipes," Applied Thermal Engineering, 25, pp 635-657.

[33] Maydanik Y. F., Vershinin S. V., and Fershtater Y. G., 1997, "Heat Transfer Enhancement in a Loop Heat Pipe Evaporator," Proc. of 10th Int. Heat Pipe Conference, Stuttgart, Germany, paper Al-3.

[34] Chernyshova M. A., Maydanik Y .F., Vershinin S. V., 1999, "Heat Exchanger in the Evaporator of a Loop Pipe with a Biporous Capillary Structure," Proc. of 11th Int. Heat Pipe Conference, Tokyo, Japan, pp 348-354.

[35] Riehl R. R., Dutra T., 2004, "Development of an Experimental Loop Heat Pipe for Application in Future Space Missions," Applied Thermal Engineering, 25, pp 101-112.

[36] Muraoka I., Ramos F. M., Vlassov V. V., 2001, "Analysis of the Operational

Characteristics and Limits of a Loop Heat Pipes with Porous Element in the Condenser," International Journal of Heat and Mass Transfer, 44, pp. 2287-2297.

[37] Pastukhov V. G., Maidanik Y. F., Vershinin C. V., and Korukov M. A., 2003, "Miniature Loop Heat Pipes for Electronics Cooling," Applied Thermal Engineering, 23, pp 1125-1135.

[38] Cheng P. and Ma H.B., A mathematical model predicting the minimum meniscus radius in mixed particles, Journal of Heat Transfer, 129, 391-394 (2007).

[39] Anjun Jiao, Sangkwon Jeong, and Hongbin Ma, 2004, "Heat Transfer Characteristics of Cryogenic Helium Gas through a Miniature Tube with a Large Temperature Difference," Cryogenics, Vol. 44, pp. 859-866.

[40] Mazur, P., Leibo, S.P., and Chu, E.H.Y.,1972, "A two factor hypothesis of freezing injury: Evidence from Chinese hamster tissue-culture cells," Exp. Cell Res. Vol.71, pp.345-355.

[41] Mazur, P., 1965, "The role of the cell membrane in the freezing of yeast and other single cells," Ann. N.Y. Acad. Sci. Vol. 125, pp.658-676.

[42] Mazur, P. 1977, "The role of intracellular freezing in the death of cells cooled at supraoptimal rates," Cryobiology Vol. 14, pp.251-272.

[43] Toscano, W.M., Cravalho, E.G., Silvares, O.M., and Huggins,C.E, 1975, "The thermodynamics of intracellular nucleation in the freezing of erythrocytes," Trans. Amer. Soc. Mech. Eng. Vol. 97, pp.326-332.

[44] Steponkus, P.L. 1984, "the role of the plasma membrane in freezing injury and cold acclimation," Annu. Rev. Plant physiol. Vol. 35, pp.543-584.

[45] Dowgert, M.F., and Steponkus, P.L. “Effect of cold acclimation on intracellular ice formation in isolated protoplasts,” Plant physiol. Vol.72, pp.978-988.

[46] Toner, M., Cravalho, E.G., Karel, M. and Armant, D.R., 1991, “Cryomicroscopic analysis of intracellular ice formation during freezing of mouse oocytes without cryoadditives,” Cryobiology, Vol.28, pp.55-71.

[47] Wolfe, J., and Bryant, G., 2001, “Cellular cryobiology: thermodynamic and mechanical effects,” International Journal of Refrigeration, Vol.24, pp.438-450.

[48] Fahy, G.M., MacFarlane, D.R., Angell, C.A. and Meryman, T.T., 1984, “Vitrification as an approach to cryopreservation,” Cryobiology, Vol.21, pp.407-426.

[49] Boutron, P., Mehl, P., 1990. “Theoretical prediction of devitrification tendency: determination of critical warming rates without using finite expansions,” Cryobiology, Vol.27, pp.359-377.

[50] Ren, H.S., Wei, Y., Hua, T.C., and Zhang, J., 1994, “Theoretical prediction of vitrification and devitrification tendencies for cryoprotective solutions,” Cryobiology, Vol.31, pp.47-56.

[51] Ren, H.S., Hua, T.C. and Yu, G.X., and Chen, X.H., 1990, “The crystallization kinetics and the critical cooling rate for vitrification of cryoprotective solutions,” Cryogenics, Vol.30, pp.536-540.

[52] Uhlmann, D.R., 1972, “A kinetic treatment of glass formation,” J. Non-crystalline solids, Vol.7, pp. 337-348.

[53] Boutron, P., 1986, “Comparison with the theory of the kinetics and extent of ice crystallization and of the glass-forming tendency in aqueous cryoprotective solutions,”

Cryobiology, Vol.23, pp.88-102.

[54] Riha, J., Landa, V., Kneissl, J., Matus, J., Jindra J., Kloucek, A., 1991, "Vitrification of cattle embryos by direct dropping into liquid nitrogen and embryo survival after nonsurgical transfer," Zivoc. Vir. , Vol.36, pp.112-120.

[55] Misumi, K., Suzuki, M., Sato, S., and Saito, N., 2003, "Successful production of piglets derived from vitrified morulae and early blastocysts using a microdroplet method," Theriogenology, Vol.60, pp.253-260.

[56] Vajta G., Holm P., Kuwayama M., Booth P.J., Jacobsen H., Greve T., and Callesen H., 1998, "Open pulled straw (OPS) vitrification: a new way to reduce cryoinjuries of bovine ova and embryos," Molecular reproduction and development, Vol.51, pp.53-58.

[57] Oberstein, N., O'Donovan, M.K., Bruemmer, J.E., Seidel, G.E., Carnevale, Jr. E.M., and Squires, E.L., 2001, "Cryopreservation of equine embryos by open pulled straw, cryoloop, or conventional slow cooling methods," Theriogenology, Vol.55, pp.607-613.

[58] Jiao A.J., Han X., Critser J.K., and Ma H.B., 2006, "Numerical investigations of transient heat transfer characteristics and vitrification tendencies in ultra-fast cell freezing processes," *Cryobiology,* Vol. 52(3), 386-392.

[59] Chandratilleke R., Hatakeyama H., and Nakagome H., 1998, "Development of cryogenic loop heat pipes," Cryogenics, 38, 263.

[60] Nakagome H., the helium magnetic refrigerator I: development and experimental results, Adv. Cryogenic Engineering, 29, 581 (1984).

[61] Rosenfeld J.H., Wolf D.A., and Buchko M.T., Emerging technologies for cryocooler interfaces, Proc. of the 8th Cryocoolers Conference, Plenum Press, New York, 743, (1995).

[62] Eggers P.E., and Serkiz A.W., Development of cryogenic heat pipes, Trans. ASME J. Eng. Power, ASME Publication paper no. 70-WA/Ener-1, 1-8, (1971).

[63] Prenger F.C., Stewart W.F., and Ruyan J.E., Development of a cryogenic heat pipe, Adv. Cryogenic Engineering, 39, 1707, (1994).

[64] Cullimore B., Krolicaek E., and Ku J., Cryogenic capillary pumped loops: anovel cryocooler integration technology, Proc. of 8th cryocoolers conference, Plenum Press, New York, 719, (1995).

[65] Mo Q. and Liang J.T., 2006, "A novel design and experimental study of a cryogenic loop heat pipe with high heat transfer capability" International Journal of Heat and Mass Transfer ,49, 770–776.

[66] Mo Q. and Liang J.T., 2006, "Operational performance of a cryogenic loop heat pipe," International Journal of Refrigeration, 29, 519–527.

[67] Mo Q., Liang J.T., Cai J.H., 2007, "Investigation of the effects of three key parameters on the heat transfer capability of a CLHP with insufficient working fluid inventory," Cryogenics, 47, 262–266.

[68] Akachi H., U.S. Patent No. 4,921,041 (1 May 1990).

[69] Zhang Y.W., and Faghri A., Advances and Unsolved issues in pulsating heat pipes, Journal of Heat Transfer Engineering, will be published.

[70] Ma H.B., Wilson C., Borgmeyer B., Park K., Yu Q., Choi S.U.S, Tirumala M., Effect of nanofluid on the heat transport capability in an oscillating heat pipe, Applied Physics Letters, 143116 (2006).

[71] Gi K., Sato F., and Maezawa S., Proc. of the 11th International Heat pipe Conference, Tokyo, Japan, 149, (1999).

[72] Zhang X.M., Xu J.L., and Zhou Z.Q., Experimental study of a pulsating heat pipe using FC-72, ethanol, and water as working fluids, Experimental Heat Transfer, 17, 47, (2004).

[73] Jiao A.J., Zhang R., Jeong S.A., 2003, "Experimental investigation of header configuration on flow maldistribution in plate-fin heat exchanger," Applied Thermal Engineering, 23, 1235-1246.

[74] Jiao A.J, Baek S., 2005, "Effects of distributor configuration on flow maldistribution in plate-fin heat exchangers, " Heat Transfer Engineering, 26 (4), 19-25.

VITA

Anjun Jiao is a PhD student in School of Mechanical Engineering, University of Missouri-Columbia, Columbia, Missouri, USA. He was born in Rizhao, Shandong Province, China. In 1984, Anjun left his hometown for the first time for his senior high school. In 1987, being attracted by the ancient culture in mid-west of China, he attended Xi'an Jiaotong University (XJTU) in Xi'an, Shaanxi Province. After receiving his Bachelor degree in 1991, he stayed at XJTU for his master's degree with specialty in Fluid and Fluid Mechanical Engineering, under the supervision of Prof. Changqing Chen. He once serviced for Chinese government after he got his master degree in 1994. In 1999, he returned XJTU and joined Prof. Chunzheng Chen's lab for Cryogenic Heat Transfer System Development. In 2002, he gained his first Ph.D. degree in Thermophysical Engineering. He joined Dr. Hongbin Ma's lab in November, 2003 and mainly focused on the heat pipes and novel evaporator development. He started to pursue his second Ph.D. degree from 8/2005. His research interests cover the Cryogenic Heat Transfer, Micro Heat Pipes, Electronic Cooling, Cell Freezing, and Numerical Simulation in Thermal-fluid. From 12/2007, he has been worked for the Nuclear Engineering Department as a senior Safety Analysis Engineer, Wolf Creek Nuclear Operating Corporation.